CONTROL OF SPRING-MASS RUNNING THROUGH VIRTUAL TUNING OF LEG DAMPING

A THESIS SUBMITTED TO
THE GRADUATE SCHOOL OF NATURAL AND APPLIED SCIENCES
OF
MIDDLE EAST TECHNICAL UNIVERSITY

BY

GÖRKEM SEÇER

IN PARTIAL FULFILLMENT OF THE REQUIREMENTS
FOR
THE DEGREE OF DOCTOR OF PHILOSOPHY
IN
COMPUTER ENGINEERING

JANUARY 2020

Approval of the thesis:

CONTROL OF SPRING-MASS RUNNING THROUGH VIRTUAL TUNING OF LEG DAMPING

submitted by **GÖRKEM SEÇER** in partial fulfillment of the requirements for the degree of **Doctor of Philosophy in Computer Engineering Department, Middle East Technical University** by,

Prof. Dr. Halil Kalıpçılar
Dean, Graduate School of **Natural and Applied Sciences** ________________

Prof. Dr. Halit Oğuztüzün
Head of Department, **Computer Engineering** ________________

Prof. Dr. Uluç Saranlı
Supervisor, **Computer Engineering, METU** ________________

Examining Committee Members:

Assoc. Prof. Dr. Erol Şahin
Computer Engineering, METU ________________

Prof. Dr. Uluç Saranlı
Computer Engineering, METU ________________

Prof. Dr. Ömer Morgül
Electrical and Electronics Engineering, Bilkent University ________________

Assist. Prof. Dr. Ali Emre Turgut
Mechanical Engineering, METU ________________

Assist. Prof. Dr. Onur Özcan
Mechanical Engineering, Bilkent University ________________

Date:

I hereby declare that all information in this document has been obtained and presented in accordance with academic rules and ethical conduct. I also declare that, as required by these rules and conduct, I have fully cited and referenced all material and results that are not original to this work.

Name, Surname: Görkem Seçer

Signature :

ABSTRACT

CONTROL OF SPRING-MASS RUNNING THROUGH VIRTUAL TUNING OF LEG DAMPING

Seçer, Görkem
Ph.D., Department of Computer Engineering
Supervisor: Prof. Dr. Uluç Saranlı

January 2020, 135 pages

Spring-mass models have been very successful in both describing and generating running behaviors. In this regard, the Spring-Loaded Inverted Pendulum (SLIP) is a useful model to represent hybrid dynamics of both natural and robotic runners. Existing research on dynamically capable legged robots, particularly those based on this model, generally considers improving in isolation the stability and control accuracy on the rough terrain or the energetic efficiency in steady state. On the other hand, the pure SLIP model is energetically conservative, hence being unable to define a way for modulation of running energy in legged robots. In this thesis, we propose a new method based on incorporating a virtually tunable leg damping onto the SLIP template model in order to control running energy while addressing both accuracy and efficiency.

In the first part of this thesis, we present our theoretical approach. Proposing to extend the basic SLIP model with a once per step tunable leg damping, we show that energy can be effectively controlled for a vertical hopping task. After showing invertibility of step-to-step Poincare map, we formulate a deadbeat controller with single step convergence. Then, we generalize this controller to planar running, which requires decomposition of the control problem into two coupled subproblems: the regulation of system energy, and the distribution of this energy among different degrees of freedom in the system. The rest of this part focuses on how to efficiently solve this problem, minimizing the energetic expenditure as well as the required computational power. To this end, we preserve the validity of the existing analytic approximations to the underlying SLIP model, propose improvements to increase the predictive accuracy, and construct accurate, model-based controllers that use the tunable damping coefficient of the template model. This part concludes with results of extensive comparative simulations to establish the energy and power efficiency advantages of our approach, together with the accuracy of model-based gait control methods.

In the second part of this thesis, we experimentally verify our theoretical claims. To this end, we, first, build a vertical hopping robot with series elastic actuation. After formulating a set of feasibility constraints towards implementation on such robotic platforms, we optimize our approach with a new gait controller allowing to use the entire stance phase for injection/removal of energy, decreasing the maximum necessary actuator power for series-elastically actuated robotic platforms while eliminating wasteful sources of the negative work altogether. Enabling the most efficient use of actuator power in this manner while preserving analytic tractability, we then show through high fidelity simulations of the robotic platform that the proposed strategy establish substantial performance gains with respect to all available alternatives. Furthermore, experimental evaluation of this approach shows that numerical results translate to the hardware, hence verifying our theoretical claims. Finally, we present our efforts towards implementation of the proposed gait controller on ATRIAS biped, which is a compliant humanoid robot with point feet. Preliminary experimental investigation on this platform reveals that our approach can provide accurate control of running on a complex bipedal robot.

Keywords: control of robotic running, spring-loaded inverted pendulum, energetic efficiency, tunable virtual damping

ÖZ

YAY KÜTLELİ KOŞUNUN SANAL BACAK SÖNÜMLENME KATSAYISI ARACILIĞI İLE KONTROLÜ

Seçer, Görkem
Doktora, Bilgisayar Mühendisliği Bölümü
Tez Yöneticisi: Prof. Dr. Uluç Saranlı

Ocak 2020 , 135 sayfa

Yay ve kütle tabanlı modeller koşu davranışlarını tanımlamakta oldukça başarılıdırlar. Bu bağlamda, Yaylı Ters Sarkaç (YTS) modeli doğal ve robotik koşuların hibrit dinamiklerini muhteva eden hassas bir modeldir. Bacaklı robotlar üzerine YTS çerçevesinde yapılmış araştırmalar genellikle ya sadece bozuk zeminde kararlılık ve gürbüzlük ya da sadece düz zeminde kararlı halde koşu sırasındaki enerji verimliliğine odaklanırlar. Bir diğer yandan, YTS modeli enerjisini koruduğu için, bacaklı robotların koşu enerjisinin nasıl değiştirileceğini tanımlayamaz. Bu tezde, koşu enerjisinin kontrolü için, kontrol hassasiyeti ve verimliliği göz önüne alarak, YTS modeline değiştirilebilir sanal bir sönümlenme katsayısı eklenmesini yeni bir kontrol yöntemi olarak öneriyoruz.

Tezin ilk bölümünde, teorik yaklaşımımız ve katkılarımız sunulmaktadır. Basit YTS modelini her adımda değiştirilebilir sanal bir sönümlenme katsayısı ile genişleterek, dikey zıplama hareketi için enerjinin etkin bir şekilde kontrol edilebildiği gösterilmektedir. Bu yaklaşım ait olan olan ölü vuruşlu kontrol probleminin iç bükey olduğu gösterildikten sonra, bu kontrolcü iki boyutlu koşu hareketine genellenir. Bu genelleş-

tirme kontrol probleminin birbiriyle bağlantılı iki alt probleme ayrılmasını gerektirir : toplam enerjinin kontrolü ve enerjinin farklı serbestlik derecelerine dağıtımı. Bu bölümün geri kalan kısmında bu problemin verimli bir şekilde nasıl çözülebileceği ele alınmıştır. Bu amaçla, literatürde YTS için önerilmiş olan mevcut analitik yaklaşık çözümlerin geçerliliği korunarak, temel olarak sönümlenme katsayısının her adımda değiştirilmesine dayalı bir takım kontrolcü iyileştirmeleri yapılmıştır. Bu bölümde, son olarak, önerdiğimiz yaklaşımın enerji/güç verimliliği ve kontrol doğruluğu açısından avantajlarını ortaya koyan kapsamlı simulasyon sonuçları sunulmuştur.

Tezin ikinci kısmında, teorik iddialarımız deneysel olarak doğrulanmaktadır. Bu amaçla, öncelikle, seri elastik eyleyicili dikey zıplayan bir robot tasarlanıp, üretilmiştir. Deneysel gerçeklenmeye yönelik olarak koşu kontrolcülerinin sağlamasının performansı artıracağı bazı kısıtlar önerildikten sonra, ilk bölümde tanıtılan kontrolcü seri elastik eyleyicili platformlarda yapılan negatif işin ortadan kaldırılması yönünde optimize edilmiştir. Bu anlamda, analitik yaklaşık çözümlerin uygulanabilirliği korunurken en verimli kontrolcü elde edilerek, üretilen platforma ait yüksek doğruluklu simülasyonda bu kontrolcünün literatürdeki mevcut tüm alternatiflerden daha iyi performans sağladığı gösterilmiştir. Daha sonra bu kontrolcü deneysel olarak gerçeklenmiş ve elde edilen deney sonuçları ile teorik bulguların uyumlu olduğu görülmüştür. Bu bölümde, son olarak, önerdiğimiz kontrolcünün kompleks bir insansı robot olan ATRIAS üzerinde gerçeklenmesine yönelik eforlarımız ve elde ettiğimiz öncül deneysel sonuçlar sunulmuştur.

Anahtar Kelimeler: robotik koşu kontrolü, yayli ters sarkaç modeli, enerji verimliliği, değiştirilebilir sanal sönümlenme katsayısı

To my dearest and lovely wife Çağlar.

ACKNOWLEDGMENTS

In the last seven years of my life, I dedicated myself to my PhD research and worked hard as there is no easy recipe for success. Perhaps, the most rewarding aspect of this long journey was my intellectual transformation from being just a student interested in robotics to a person who has gotten deeper knowledge in robotics while still being a student in almost every other field. Throughout this transformation, I have deeply understood the current status and future outlook of robotics research and developed a wide range of interests (from math to neuroscience) on which I want to improve the breadth of my knowledge and experience. At some point in the future, I am hoping to become a person who can connect these seemingly distant dots to maximize my contribution to the scientific community.

Many people helped me throughout these seven years. Among them, I owe my deepest gratitude to my supervisor Uluç Saranlı. He was an incredible advisor who helped me discover and grow creativity, enthusiasm, and diligence. He taught me not only countless things in robotics but also how to become a good scholar.

I want to thank committee members of my thesis jury Ömer Morgül, Erol Şahin, Ali Emre Turgut, and Onur Özcan for their feedbacks and approving my work.

I also want to thank Hartmut Geyer for the inspiring discussions and allowing me to conduct experiments on the ATRIAS biped. Those discussions were transformative for me and helped me understand the difference between engineering and basic science.

Aside from long hours of experiments in the lab, the most joyful moments of my Ph.D. life were the times I was with my friends who are my fellow scientists. I am very thankful to Berk Gönenç, Hasan Hamzaçebi, Ali Nail İnal, Emrullah Korkmaz, İsmail Uyanık, and Mehmet Mutlu for our wonderful times at METU, Bilkent, CMU, and Baltimore. I also want to thank Sinan Şahin Candan, Salih Can Çamdere, Ali Levent Çınar, Deniz Kerimoğlu, Gökhan Gültekin, Bahadır Çatalbaş, Osman Kaan

Karagöz, Başer Kandehir, Sitar Kortik, Timothy Kyung, William Martin, Çağlar Seylan, and Nitish Thatte for their help in work-related or non-work-related part of my life.

In all those years, I also worked full time in the industry. There were many people who made my times at ROKETSAN more enjoyable. I want to thank Sinan Arda, Metin Arslan, Kadir Baş, Semih Çakıroğlu, Alper Kahvecioğlu, Batuhan Kaygusuz, Zafer İbrahim Esen, Zafer Külünk, Murat Şahin, and Çağatay Tanıl for being good friends and great coworkers who tolerated my stressful times and supported my Ph.D. studies.

I am also appreciative of the financial support from the Scientific and Technological Research Council of Turkey (TUBITAK) during my Ph.D. study. TUBITAK supported the work presented in this thesis through the 2211 scholarship program and project 114E277. I also appreciate The Fulbright Program and The Turkish Fulbright Commission, providing me the financial support for my one year at Robotics Institute, Carnegie Mellon University, through Visiting Student Researcher Fellowship.

Finally, I want to express my thanks to my lovely wife Çağlar Coşarderelioğlu Seçer from the bottom of my heart, for being always there to listen and supporting me through this long and rocky road with her undying love. Her love is a gift that I am thankful for every day. This thesis would not have been possible without her. I also would like to give my warmest thanks to my parents Kadriye Benan Seçer, Osman Seçer and my grandparent Müzeyyen Tayyibe Yalçıner for raising me to be a healthy, motivated, and hardworking person.

TABLE OF CONTENTS

LIST OF TABLES

TABLES

LIST OF FIGURES

FIGURES

LIST OF ABBREVIATIONS

ABBREVIATIONS	
2D	2 Dimensional
3D	3 Dimensional
COM	Center of Mass
DOF	Degrees of Freedom
FSLIP	Forced Spring-Loaded Inverted Pendulum
FL	Feedback-Linearization
PE	Percentage Error
RMS	Root Mean Square
SEA	Series Elastic Actuator
SLIP	Spring-Loaded Inverted Pendulum
VPPC	Virtual Pivot Point Pendulum-Based Control

CHAPTER 1

INTRODUCTION

1.1 Motivation and Problem Definition

Legged animals demonstrate a vast range of dynamic locomotion behaviors on a variety of terrains. These animals have highly skilled locomotor systems capable of producing robust, flexible, and maneuverable gaits. Although most motorized robotic platforms that have been built are wheeled, legs have several advantages over wheels : 1) Legs can go over all terrains as opposed to wheels that are effective across flat surfaces. For this reason, wheeled vehicles have difficulty in climbing stairs or rocks, limiting their area of use to specially designed outdoor environments. 2) Legged platforms promise more mobility and agility as opposed to wheeled vehicles whose minimum turning radius is limited by the structure of the vehicle. In this regard, the last decade has witnessed dramatic progress in the development of legged robotic platforms towards the ultimate goal of commercializing assistive robots in our daily lives [46, 106, 32, 82]. However, there are several challenges building these machines : 1) Legged robots have complex mechanics, requiring lightweight structural design with sufficient strength against high contact forces and impacts. 2) They are difficult to control as they are nonlinear and hybrid dynamical systems with high dimensional state spaces (e.g., ATLAS humanoid robot has 28 degrees-of-freedom (DOF) [63]). 3) Energetic efficiency is still an unresolved issue, infeasibly restricting the operational duration of legged robots on a single battery charge.

This thesis concerns the energetic efficiency problem of legged locomotion. In particular, adopting a model-based approach, the primary objective is to develop a simplified model of running that can be efficiently and accurately realized by robotic platforms with series elastic actuation. To this end, we extend the Spring-Loaded Inverted Pendulum (SLIP) model, which is a commonly employed model of running. This thesis presents our efforts on the construction of the extended model from scratch and the formulation of energetically efficient controllers for this model. After theoretical developments in this direction, we report experimental results of proposed algorithms on physical robotic platforms.

1.2 Organization and Contributions

1.2.1 Control Through Virtual Tuning of Leg Damping in Hopping

A commonly used model representing dynamics of running is Spring-Loaded Inverted Pendulum (SLIP) [12]. As it can accurately explain the center of mass (COM) trajectories of natural runners [30], it serves as a reference model to generate running motion for robots [8, 116, 22, 41, 45], theoretically promising the stability and robustness of their natural counterparts [118]. However, trajectories defined by the SLIP model as the desired task for robots are energetically conservative, thus restricting the robot to run at a constant energy level. Motivated by this limitation of the SLIP model, we propose a new model allowing efficient modulation of the locomotion energy in Chapter 2. Our particular contributions in this chapter are as follows:

- An extended SLIP model is introduced by incorporating a virtually tunable damper into the SLIP model for the control of height in vertical hopping as a representative component of energetics in the running.
- We show that the step-to-step change in mechanical energy is an invertible function of damping.
- We show that a simple proportional feedback control law tuning the damping value once per step results in a global asymptotically stable policy to reach a desired hopping height.
- Following from the invertibility, we formulate a novel height controller with a single step convergence guarantee is formulated to reach the desired hopping height by once per step tuning of leg damping.

- Numerical results show that virtual tuning of leg damping is indeed an effective way of controlling energy.

1.2.2 Generalization of Damping-Based Control to Planar Running

Originally proposed as a model of COM dynamics for one dimensional (1D) hopping in place and 2D running in the sagittal plane [12], many extensions, including ours, have been proposed in the literature to generalize SLIP model to higher dimensional tasks such as locomotion in 3D space [98], running with an upright trunk posture [70], and energetically non-conservative gaits. While compromising simplicity, these extensions serve two purposes : i) The model becomes more realistic with the addition of new details, thus allowing to conduct more meaningful analysis about natural runners. ii) The model can be transferred more accurately to a physical platform by addressing practical issues in a real-world robot, such as compensation of lost energy within the mechanical structure and trunk stabilization. With the latter objective, in Chapter 3, we propose for energetically efficient control of planar running. In this context, our contributions are as follows:

- The model in Chapter 2 is extended and adapted to the sagittal plane. The new model is called FSLIP.
- Considering series elastically actuated robotic platforms, a novel control policy called shifted variable damping (SVD) is proposed to regulate 2D running.
- In order to reduce the computational cost of SVD policy, an approximate analytical solution to hybrid nonlinear dynamics of FSLIP is proposed by substantially improving on [88].
- We introduce a hierarchical modeling and control framework allowing to accurately and systematically transfer behavior of a simple model like FSLIP.
- We conduct extensive simulations and present numerical results showing that SVD is superior compared to a traditional approach in terms of accuracy and energetic efficiency.

1.2.3 Experimental Evaluation on a Vertically Constrained Hopping Robot

Even though the spring-mass model theoretically offers self-stability [99, 31] and robustness [25, 118] under highly accurate deadbeat control policies [118, 116], its transfer to physical robotic platforms is often challenging, resulting in inaccurate target behavior deviating from the theory due to discrepancies in the hardware [68, 45]. Among many discrepancies, [117] highlights the limited bandwidth of series elastic actuators as the central reason for poor experimental performance. In this regard, considering a real-world physical hopping robot having a series elastic actuator, Chapter 4 reports experimental and simulation results of many controllers available in the literature compared to a new controller introduced in this chapter. While doing so, our particular contributions are as follows :

- We propose a set of conditions for a gait control policy to be accurately implementable for series-elastically actuated robotic platforms.
- We introduce a new policy called CVD+ satisfying proposed conditions in the scope of FSLIP model introduced in Chapter 3
- We show through numerical simulations of a series-elastically actuated robotic platform that efficiency and accuracy of CVD+ are far better than many alternative policies available in the literature, including SVD from Chapter 3.
- We built a vertical hopping robotic platform with a series elastic actuation and implement a set of controllers within the hierarchical control framework introduced in Chapter 3.
- We conduct extensive simulations and present numerical results showing that SVD is superior compared to a traditional approach in terms of accuracy and energetic efficiency.

1.2.4 Transferring Algorithms to Real World Bipedal Robot Hardware

The final objective of this thesis is to transfer the FSLIP model controlled with CVD+ policy onto a physical bipedal robot. In this regard, we use Carnegie Mellon University's ATRIAS bipedal robot [68] built by the Dynamic Robotics Laboratory at

Oregon State University [46] as a target hardware platform. In order to embed the behavior defined by the FSLIP model, we follow a mixture of the hierarchical control approach, along with practical considerations specific to the ATRIAS hardware platform. Finally, we conduct experiments based on this approach and report our preliminary results in Chapter 5. These results suggest that the CVD+ policy and FSLIP can be effectively translated to real-world humanoid platforms for the control of running.

CHAPTER 2

CONTROL OF VERTICAL SPRING-MASS HOPPING THROUGH ACTIVE VIRTUAL TUNING OF LEG DAMPING

In Chapter 1, we justified our reasoning for pursuing energetically efficient gait control strategies in legged locomotion. In this chapter, we present the main idea of this thesis, which is to use a virtual viscous damping in the context of model-based legged running towards this ultimate goal of obtaining an energetically efficient gait control strategy. In this presentation, we consider the hopping behavior as a preliminary and representative task for regulation of energy in more complex robotic platforms with series elastic actuation. The work in this chapter has also been reported and appeared in [94].

2.1 Introduction

Design, analysis and accurate control of legged robot behaviors have been among difficult challenges faced by robotics researchers. This line of inquiry brought together researchers from different areas, including biomechanics [13], dynamical systems [44], control theory [19], mechanical engineering [17] and materials science [111], towards the goal of building high performance autonomous legged machines. Surprisingly, simple hybrid spring-mass models have been able to capture the essence of basic running behaviors, embodied by the now widely accepted Spring-Loaded Inverted Pendulum (SLIP) model [92]. Since its early discovery [12], to its first instantiation on physical robot platforms [83], with more recent detailed analysis [58, 93, 88, 120], as well as extensions and adoption by morphologically different platform designs [121, 33, 104, 36, 83], this model continues to provide a rich context in which running behaviors can be studied and implemented.

One of the challenges in the embodiment of the fully passive SLIP model in physical robots [27, 4] is the manner in which system energy can be managed through active components. In some cases, such as the flight precompression of the leg in the Bow-Leg platform [121], this is accomplished without compromising the passivity of the stance phase. Another approach which remains within the confines of the ideal model has been active modulation of spring stiffness during stance, implemented by some recent platform designs such as the BiMASC [50] and MABEL [48] platforms. Alternatively, for platforms that use a hip actuator as the only energy input, extensions to the model were necessary to support controller design and stability analysis [6].

Among the best combinations of mechanical simplicity and minimal deviations from the ideal spring-mass model are designs that incorporate a linear positional actuator in series with the leg spring. Raibert's hoppers were similar to this design in their use of a pneumatic actuator in series with the spring [84, 83]. The difficulty of accurate position control for these actuators was addressed by the ARL Monopod [33], which uses a DC motor coupled with the spring through a ball screw. More recent instantiations of this idea can be observed in the ATRIAS biped [36] as well as other small experimental platforms [86]. Recent efforts include using principles behind series-elastic actuators, considering the combination of the spring and the actuator as a force transducer [77, 59]. Improvements in rough terrain mobility, as well as new analytically tractable solutions to resulting dynamics have been reported in the literature [47, 87].

In this chapter, we propose a novel control idea that bridges the analytic gap between such serially actuated compliant leg designs and the passive SLIP model. In particular, we consider the lossy SLIP model, a generalization of the ideal, conservative model, as a basis for our locomotion controllers. The previous work on approximate but accurate analytic solutions to the dynamics of this system have been instrumental in the construction of adaptive, model-based controllers and state estimators for running behaviors [88]. The proposed idea is based on active modulation of the leg force through the series elastic leg actuation to obtain a virtual SLIP model whose viscous damping coefficient can be selected as desired by a high level gait controller.

Active control of damping is traditionally considered for vibration control in various application areas [53, 57, 71], wherein dissipative forces are actively introduced into the system to attenuate unwanted vibrations. In contrast, systems with different, possibly negative, damping coefficients at different parts of their state space have been used to induce stable oscillatory behavior that are useful for many application domains [20], including locomotion [2]. The novelty of our approach lies in our goal of embedding a simple, analytically tractable *template* system within a more complex *anchor* structure [27]. As a result, we are able to ensure the applicability of analytic models and gait controllers designed for the lossy SLIP model, providing a useful abstraction for the control of running behaviors. We also show, through systematic simulation studies, that energy efficiency, control accuracy as well as power requirements on the leg actuation resulting from this strategy are better than its most common alternative, variable stiffness [50], for regulating system energy when actuator limitations are considered. For simplicity of the presentation, the scope of this chapter is limited to a simple vertical model that captures relevant yet fundamental issues in controlling the energy for a hopping system, leaving the generalization of the proposed idea for planar running and extensions toward physical implementations to subsequent chapters.

2.2 Control of Hopping Through Active Tuning of Damping

In this section, we present a new gait control idea for running behaviors using active tuning of damping properties within the system dynamics. For clarity and simplicity, we focus our presentation to vertical hopping models, which capture all relevant energetic aspects of planar running, noting that our results can readily be extended to two dimensions as will be shown in Chapter 3. We first present in Section 2.2.1 our "anchor" model, which incorporates a linear actuator in series with the leg spring. Section 2.2.2 then describes our "template", which is a lossy SLIP model with a tunable, possibly negative, damping constant, and presents analytic solutions to its dynamics within a single hop.Section 2.2.3 shows how this template can be embedded within the anchor system, followed by a presentation of the high level gait controller in Section 2.2.4 as well as practical considerations in Section 2.2.6.

2.2.1 The Anchor: Vertical SLIP with Linear Actuation

A simple model for the vertical hopper with series actuation in the leg, which we call VA-SLIP, is illustrated in Figure 2.1.a. It incorporates a linear actuator in series with the leg spring in order to inject or remove energy from the system. This actuator is assumed to be position controlled, with its length δ considered as a control input. Similar to planar SLIP models, this model alternates between stance and flight phases, that can further be decomposed into compression and decompression, and ascent and descent, respectively. Touchdown, liftoff, bottom, and apex events, respectively identified with subscripts td, lo, b, and a, mark transitions among these sub-phases and are defined in the same way as the ideal SLIP model [88]

The VA-SLIP model follows ballistic trajectories during flight, captured by the dynamics

$$\ddot{z} = -g. \tag{2.1}$$

Stance dynamics, however, are those of a second-order spring-mass system with a constant forcing term due to gravity, and the spring length modulated through the actuator input, taking the form

$$\ddot{z} = -g - \frac{k_p}{m}(z - z_0 - \delta) - \frac{d_p}{m}\dot{z}\ . \tag{2.2}$$

Since we focus on a purely vertical system, a Poincaré section at the apex point yields

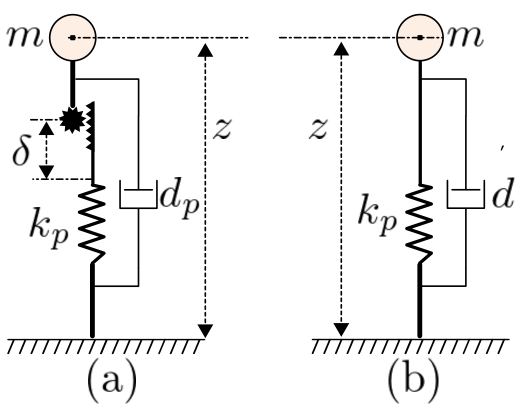

Figure 2.1: (a) VA-SLIP: Vertical SLIP model with linearly actuated compliant leg and physical damping coefficient d_p, (b) VD-SLIP: Vertical SLIP template with a tunable, possibly negative, damping coefficient d.

the one dimensional apex state $h := z_a$. As usual, we define the apex return map as a combination of four components as

$$h_{k+1} = \mathcal{R}(h_k, u) := \, {}^{\mathrm{a}}_{\mathrm{lo}}\mathcal{R} \circ^{\mathrm{lo}}_{\mathrm{b}} \mathcal{R}_\delta \circ^{\mathrm{b}}_{\mathrm{td}} \mathcal{R}_\delta \circ^{\mathrm{td}}_{\mathrm{a}} \mathcal{R}_\delta(h_k), \tag{2.3}$$

where ${}^{\mathrm{td}}_{\mathrm{a}}\mathcal{R}$, ${}^{\mathrm{b}}_{\mathrm{td}}\mathcal{R}_u$, ${}^{\mathrm{lo}}_{\mathrm{b}}\mathcal{R}_u$, and ${}^{\mathrm{a}}_{\mathrm{lo}}\mathcal{R}$ denote descent, compression, decompression, and ascent phases, respectively, and h_k denotes the k^{th} apex state. Maps for compression and decompression are subscripted with δ since they depend on the particular choice of control strategy during stance.

2.2.2 The Template: Vertical SLIP with Tunable Damping

In contrast to the actuated VA-SLIP model, which roughly corresponds to the physical robot implementation, Figure 2.1.b shows the passive SLIP model with a tunable damping coefficient d, which we call VD-SLIP. We will use this model as a dynamical template to interface our high level gait controller for the actuated physical system. Flight dynamics for this model are identical to those of the actuated model, but stance dynamics take the form

$$\ddot{z} = -g - \frac{k_p}{m}(z - z_0) - \frac{d}{m}\dot{z} \ , \tag{2.4}$$

excluding the actuation and incorporating a different damping coefficient, d, considered to be a control input.

For the planar lossy SLIP model, [88] presented an accurate approximation for the return map. Unlike the planar SLIP model, however, vertical hopper dynamics admit an exact solution that we outline in the rest of this section. Energy is conserved during flight, yielding descent and ascent maps as

$$\begin{aligned} [z_{\mathrm{td}}, \dot{z}_{\mathrm{td}}]^T_k &= {}^{\mathrm{td}}_{\mathrm{a}}\mathcal{R}(z_{\mathrm{a,k}}) = [z_0, 2g\sqrt{z_{\mathrm{a,k}} - z_0}]^T && (2.5) \\ z_{\mathrm{a,k+1}} &= {}^{\mathrm{a}}_{\mathrm{lo}}\mathcal{R}([z_{\mathrm{lo}}, \dot{z}_{\mathrm{lo}}]^T_k) = z_{\mathrm{lo},k} - (\dot{z}_{\mathrm{lo},k})^2/(2g) \ . && (2.6) \end{aligned}$$

Here, we assume that the actuator position is reset with $\delta = 0$ prior to touchdown. Return maps for compression and decompression require solving (2.2). Assuming underdamped dynamics with $d^2 - 4k_p m < 0$, which is actually necessary to ensure liftoff and enable locomotion, we have

$$
\begin{aligned}
z(t) &= M\, e^{-\xi\omega_n t}\cos\left(\omega_n\sqrt{1-\xi^2}t+\phi\right)+\frac{F}{\omega_n^2} && (2.7)\\
\dot{z}(t) &= -M\omega_n\, e^{-\xi\omega_n t}\cos\left(\omega_n\sqrt{1-\xi^2}t+\phi+\phi_2\right), && (2.8)
\end{aligned}
$$

with

$$
\begin{aligned}
M &:= (c_1^2+c_2^2)^{1/2}\\
\phi &:= -\arctan(c_2/c_1)\\
\phi_2 &:= -\arctan(1-\xi^2)^{1/2}/\xi\\
\omega_n &:= \sqrt{k/m}\\
\xi &:= d/(2\sqrt{km})\\
F &:= -g+\omega_n^2 z_0\\
c_1 &:= g/\omega_n^2\\
c_2 &:= (\dot{z}_{\mathrm{td}}+c_1\xi\omega_n)/(\omega_n\sqrt{1-\xi^2})
\end{aligned}
.
$$

The bottom transition occurs at the end of compression with

$$
t_b = (\pi/2-\phi-\phi_2)/(\omega_n\sqrt{1-\xi^2})\ . \tag{2.9}
$$

During decompression, liftoff occurs when the ground reaction force or comp crosses zero, which can be marked with

$$
k\,(z-z_0)+d\dot{z}=0\ . \tag{2.10}
$$

Adopting the approximation proposed in [88] for the exponential term in (2.8) to its value at the bottom time t_b as $e^{-\xi\omega_n t}\approx e^{-2\xi\omega_n t_b}$, the liftoff time takes the form

$$
t_{\mathrm{lo}} \approx \frac{2\pi-\arccos(k(z_0-F/\omega_n^2)e^{2\xi\omega_n t_b}/\left(\overline{M}M\right))-\phi-\phi_3}{\omega_n\sqrt{1-\xi^2}} \tag{2.11}
$$

with

$$
\begin{aligned}
\overline{M} &:= \sqrt{k^2-2kd\omega_n\cos\phi_2+d^2\omega_n^2}\\
\phi_3 &:= -\arctan(d\omega_n\sin\phi_2/(k-d\omega_n\cos\phi_2))
\end{aligned}
.
$$

These derivations complete the Poincaré map, allowing us to formulate gait controllers focusing on the virtual damping coefficient d as a control input in Section 2.2.4.

2.2.3 Embedding VD-SLIP into VA-SLIP

As noted in Section 2.2.1, the linear actuator in the VA-SLIP model is assumed to be position controlled, meaning that the control input δ can be chosen as desired. Using this model to realize VD-SLIP dynamics requires that the acceleration felt by the robot body is identical for both, leading to the constraint

$$-g - \frac{k_p}{m}(z - z_0 - \delta) - \frac{d_p}{m}\dot{z} = -g - \frac{k_p}{m}(z - z_0) - \frac{d}{m}\dot{z}\ . \tag{2.12}$$

Solving this equation for the control input δ hence yields the continuous stance controller for the VA-SLIP anchor model to properly realize VD-SLIP dynamics with

$$\delta_e(t) = \frac{d_p - d}{k_p}\dot{z}(t). \tag{2.13}$$

Note that since this embedding exactly realizes VD-SLIP dynamics, the analytic return map derivations of Section 2.2.2 remain valid.

Close inspection of (2.13) shows that energy input from the actuator resulting from this embedding controller will be spread throughout the stance phase in contrast to methods that require abrupt step commands to the actuator such as those used by Raibert's hoppers or the ARL Monopod. Consequently, this method will present substantial benefits in power requirements on the actuator compared to the alternative method of adjusting spring stiffness at bottom that can also preserve the validity of analytic solutions [92, 9]

2.2.4 High-Level Control of Energy

Now that we have active control over the damping coefficient of the VD-SLIP template, we can use it for gait control. For vertical hoppers, this is equivalent to controlling system energy, with positive and negative values of d used for decreasing and increasing the energy level of the system, respectively. We begin by noting that the return map for the VD-SLIP model now accepts d as a control parameter, rewritten as

$$\mathcal{R}(h_k, d) = h_{k+1}\ . \tag{2.14}$$

In the following subsections, after analysing this form of the return map in depth, we present a gait controller that relies on once per step tuning of virtual damping d.

2.2.4.1 Analysis of Return Map's Dependence on Damping

Identifying the mechanical energy with the apex height, the return map relating apex states at k^{th} step to the next can be alternatively written as

$$h_{k+1} = \mathcal{R}(h_k, d) = h_k +_{\mathrm{td}}^{\mathrm{lo}} (\Delta E)/(mg) \tag{2.15}$$

with ${}_{\mathrm{td}}^{\mathrm{lo}}(\Delta E) := \widetilde{E}_{\mathrm{lo}} - \widetilde{E}_{\mathrm{td}}$ denoting the change in mechanical energy of the mass m between touchdown and liftoff whose energies can be respectively defined as

$$\begin{aligned} \widetilde{E}_{\mathrm{td}} &:= \frac{1}{2} m \dot{z}_{\mathrm{td}}^2 + mgz_{\mathrm{td}} \\ \widetilde{E}_{\mathrm{lo}} &:= \frac{1}{2} m \dot{z}_{\mathrm{lo}}^2 + mgz_{\mathrm{lo}} \end{aligned} .$$

In the rest of this section, based on these quantities, we present a rigorous analysis about the dependence of return map on damping. In particular, through this analysis, we show

1. The return map $\mathcal{R}(h_k, d)$ is an invertible function of damping for a given h_k.

2. A simple proportional feedback controller tuning the damping once per step according to $d(h_k) = -\kappa(h^\star - h_k)$ renders the system $h_{k+1} = \mathcal{R}(h_k, d(h_k))$ global asymptotically stable for a desired apex height $h^\star$.

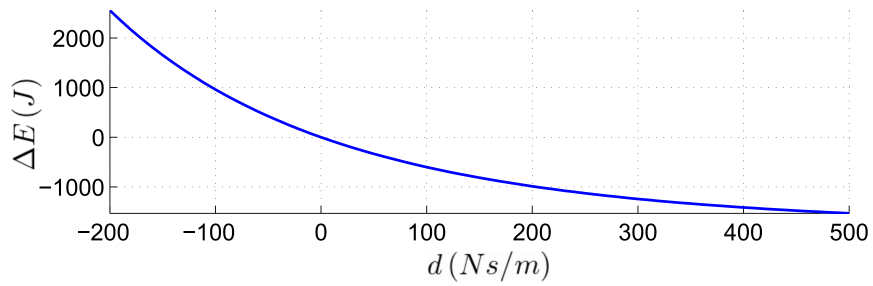

Figure 2.2: Monotonic dependence of the change in VD-SLIP energy, ΔE on the virtual damping coefficient d.

The former result will be useful to show the existence of a controller with a single step convergence, which will be further formulated in Sec. 2.2.4.2 . On the other hand, the latter also provides a strong result as being the second global asmyptotically stable controller in the literature for SLIP-like hopping after Koditschek's seminal work [58], to the best of our knowledge.

Assumption 1. *Feasible range of leg damping is assumed to be* $d \in D := [d_{\min}, d_{\max}]$ *with* $d_{\min} = -\sqrt{km}$ *and* $d_{\max} = \sqrt{km}$ *corresponding to damping ratios*

$$\xi := \frac{d}{2\sqrt{km}} \in [-0.5, 0.5].$$

Lemma 1. *For a given* h_k*, the return map* $R(h_k, d)$ *is a monotonically decreasing function of* d *on the interval* D*. A numerical example to this statement is illustrated in Fig. 2.2.*

Proof. *For monotonic dependence stated by the Lemma, we need to show*

$$\mathcal{R}'(d) = \frac{\mathrm{d}R(h_k, d)}{\mathrm{d}d} < 0 \; \forall d \in D. \tag{2.16}$$

Differentiating (2.15) and using explicit forms of $\widetilde{E}_{\mathrm{td}}$ *and* $\widetilde{E}_{\mathrm{lo}}$*, we obtain*

$$\mathcal{R}'(d) = \frac{1}{mg}\frac{\mathrm{d}\widetilde{E}_{\mathrm{lo}}}{\mathrm{d}d}.$$

Hence, the theorem can be proved by showing

$$\frac{\mathrm{d}\widetilde{E}_{\mathrm{lo}}}{\mathrm{d}d} < 0.$$

To this end, we first express the stance dynamics in a shifted coordinate system $w := z + mg/k - z_0$*, yielding*

$$\ddot{w} = -\frac{k}{m}w - \frac{d}{m}\dot{w}.$$

The solution to trajectories, now, takes the form

$$\begin{aligned} w(t) &= e^{-t\frac{d}{2m}}\Big[w_{\mathrm{td}}\cos\Big(t\tfrac{\sqrt{4km-d^2}}{2m}\Big) + \tfrac{2m\dot{w}_{\mathrm{td}}+dw_{\mathrm{td}}}{\sqrt{4km-d^2}}\sin\Big(t\tfrac{\sqrt{4km-d^2}}{2m}\Big)\Big] \\ \dot{w}(t) &= -\tfrac{d}{2m}w(t) + e^{-t\frac{d}{2m}}\Big[\tfrac{2m\dot{w}_{\mathrm{td}}+dw_{\mathrm{td}}}{2m}\cos\Big(t\tfrac{\sqrt{4km-d^2}}{2m}\Big) - \tfrac{w_{\mathrm{td}}\sqrt{4km-d^2}}{2m}\sin\Big(t\tfrac{\sqrt{4km-d^2}}{2m}\Big)\Big] \end{aligned} . \tag{2.17}$$

Defining the total mechanical energy in unshifted coordinates during stance with

$$E := \frac{1}{2}k\left(z - z_0\right)^2 + \frac{1}{2}m\dot{z}^2 + mgz,$$

the total mechanical energy $W := \frac{1}{2}kw^2 + \frac{1}{2}m\dot{w}^2$ *in shifted coordinates is related to it as*

$$E = W + mg(z_0 - mg/(2k)), \tag{2.18}$$

implying $\frac{\mathrm{d}E}{\mathrm{d}d} = \frac{\mathrm{d}W}{\mathrm{d}d}$*. Taking the square of (2.17), adding the resulting two equations side-by-side, and algebraic manipulation yields*

$$e^{t\frac{d}{m}}(kw^2 + bw\dot{w} + m\dot{w}^2) = kw_{\mathrm{td}} + w_{\mathrm{td}}\dot{w}_{\mathrm{td}} + m\dot{w}_{\mathrm{td}}^2,$$

which we can further arrange to express the energy W *as a function of time with*

$$W = e^{-t\frac{d}{m}}(W_{\mathrm{td}} + \frac{1}{2}dw_{\mathrm{td}}\dot{w}_{\mathrm{td}}) - \frac{1}{2}dw\dot{w}.$$

After expressing liftoff condition (2.10) in shifted coordinates as

$$\dot{w}_{\mathrm{lo}} = -\frac{k}{d}(w_{\mathrm{lo}} - w_{\mathrm{td}}), \tag{2.19}$$

we obtain an alternative form for the liftoff energy with

$$W_{\mathrm{lo}} = e^{-t_{\mathrm{lo}}\frac{d}{m}}(W_{\mathrm{td}} + \frac{1}{2}dw_{\mathrm{td}}\dot{w}_{\mathrm{td}}) + \frac{1}{2}kw_{\mathrm{lo}}(w_{\mathrm{lo}} - w_{\mathrm{td}}).$$

On the other hand, since the stored spring energy is lost with the liftoff, only kinetic and gravitational potential energies contribute to the flight. In this regard, we introduce a new energetic quantity to define the sum of kinetic and gravitational potential energies as

$$\widetilde{W}_{\mathrm{lo}} := W_{\mathrm{lo}} - \frac{1}{2}kw_{\mathrm{lo}}^2 + kw_{\mathrm{td}}w_{\mathrm{lo}} = e^{-t_{\mathrm{lo}}\frac{d}{m}}(W_{\mathrm{td}} + \frac{1}{2}dw_{\mathrm{td}}\dot{w}_{\mathrm{td}}) + \frac{1}{2}kw_{\mathrm{td}}w_{\mathrm{lo}}. \tag{2.20}$$

This quantity is indeed related to $\widetilde{E}_{\mathrm{lo}}$ *up to an additive constant, which is the same way* E *is related to* W *as given in (2.18). Therefore, we have*

$$\frac{\mathrm{d}\widetilde{W}_{\mathrm{lo}}}{\mathrm{d}d} = \frac{\mathrm{d}\widetilde{E}_{\mathrm{lo}}}{\mathrm{d}d},$$

suggesting that it is sufficient to show $\frac{\mathrm{d}\widetilde{W}_{\mathrm{lo}}}{\mathrm{d}d} < 0$ *for the proof. Differentiating (2.20), this inequality can be explicitly expressed as*

$$\frac{\mathrm{d}\widetilde{W}_{\mathrm{lo}}}{\mathrm{d}d} = e^{-t_{\mathrm{lo}}\frac{d}{m}}\left[\frac{1}{2}w_{\mathrm{td}}\dot{w}_{\mathrm{td}} - \frac{t_{\mathrm{lo}} + d(\mathrm{d}t_{\mathrm{lo}}/\mathrm{d}d)}{m}(W_{\mathrm{td}} + \frac{1}{2}dw_{\mathrm{td}}\dot{w}_{\mathrm{td}})\right] + \frac{1}{2}kw_{\mathrm{td}}\frac{\mathrm{d}w_{\mathrm{lo}}}{\mathrm{d}d} < 0. \tag{2.21}$$

As t_{lo} *does not admit an analytical solution (see Section 2.2.2), we follow a different strategy to express the term* $t_{\mathrm{lo}} + d(\mathrm{d}t_{\mathrm{lo}}/\mathrm{d}d)$ *as a function of liftoff position* w_{lo}*. To* *this end, we indirectly define the liftoff time relative to a new event, called extended top corresponding to a fictitious configuration of VD-SLIP that would occur at $\dot{z} = 0$ after liftoff with $z > z_{\mathrm{lo}}$ if the model was pinned to ground, as illustrated in Figure 2.3. In particular, the liftoff time can be computed in this way as $t_{\mathrm{lo}} = t_{\mathrm{td,ext}} - t_{\mathrm{td,ext}}$. with $t_{\mathrm{td,ext}}$ from touchdown to extended top and the duration $t_{\mathrm{lo,ext}}$ from liftoff to extended top, respectively taking the form*

$$
\begin{aligned}
t_{\mathrm{td,ext}} &= \frac{2m}{\sqrt{4km - d^2}} \left[2\pi + \arctan \frac{\dot{w}_{\mathrm{td}} \sqrt{4km - d^2}}{2kw_{\mathrm{td}} + d\dot{w}_{\mathrm{td}}} \right] \\
t_{\mathrm{lo,ext}} &= \frac{2m}{\sqrt{4km - d^2}} \arctan \frac{\dot{w}_{\mathrm{lo}} \sqrt{4km - d^2}}{2kw_{\mathrm{lo}} + d\dot{w}_{\mathrm{lo}}}
\end{aligned}
. \tag{2.22}
$$

Substituting liftoff condition (2.19) into these equations and differentiation with respect to d yields

$$
\begin{aligned}
\frac{\mathrm{d}t_{\mathrm{td,ext}}}{\mathrm{d}d} &= \frac{2dm}{(\sqrt{4km - d^2})^3} \left[2\pi + \arctan \frac{\dot{w}_{\mathrm{td}} \sqrt{4km - d^2}}{2kw_{\mathrm{td}} + d\dot{w}_{\mathrm{td}}} \right] - \frac{m\dot{w}_{\mathrm{td}}(2m\dot{w}_{\mathrm{td}} + dw_{\mathrm{td}})}{(4km - d^2)(2W_{\mathrm{td}} + dw_{\mathrm{td}}\dot{w}_{\mathrm{td}})} \\
\frac{\mathrm{d}t_{\mathrm{lo,ext}}}{\mathrm{d}d} &= \frac{2dm}{(\sqrt{4km - d^2})^3} \arctan \left(\frac{\sqrt{4km - d^2}(w_{\mathrm{lo}} - w_{\mathrm{td}})}{d(w_{\mathrm{lo}} + w_{\mathrm{td}})} \right) \\
&\quad + \frac{2km^2(w_{\mathrm{lo}}^2 - w_{\mathrm{td}}^2) - dm(4km - d^2)w_{\mathrm{td}}(\frac{\mathrm{d}w_{\mathrm{lo}}}{\mathrm{d}d})}{(4km - d^2)(d^2/k)(2W_{\mathrm{lo}} + dw_{\mathrm{lo}}\dot{w}_{\mathrm{lo}})}
\end{aligned}
.
$$

Multiplying these equations by d and adding side-by-sde with (2.22) gives

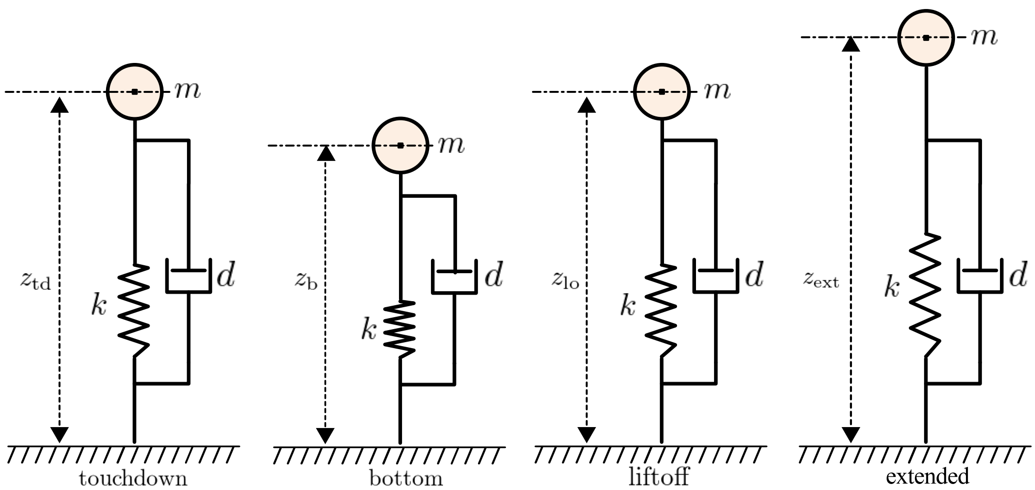

Figure 2.3: Monotonic dependence of the change in VD-SLIP energy, ΔE on the virtual damping coefficient d.

$$
\begin{aligned}
t_{\mathrm{td,ext}} + d\frac{\mathrm{d}t_{\mathrm{td,ext}}}{\mathrm{d}d} &= \frac{8km^2}{(\sqrt{4km-d^2})^3}\left[2\pi + \arctan\frac{\dot{w}_{\mathrm{td}}\sqrt{4km-d^2}}{2kw_{\mathrm{td}}+d\dot{w}_{\mathrm{td}}}\right] - \frac{dm\dot{w}_{\mathrm{td}}(2m\dot{w}_{\mathrm{td}}+dw_{\mathrm{td}})}{(4km-d^2)(2W_{\mathrm{td}}+dw_{\mathrm{td}}\dot{w}_{\mathrm{td}})} \\
t_{\mathrm{lo,ext}} + d\frac{\mathrm{d}t_{\mathrm{lo,ext}}}{\mathrm{d}d} &= \frac{8km^2}{(\sqrt{4km-d^2})^3}\arctan\left(\frac{\sqrt{4km-d^2}(w_{\mathrm{lo}}-w_{\mathrm{td}})}{d(w_{\mathrm{lo}}+w_{\mathrm{td}})}\right) \\
&\quad + \frac{2km^2(w_{\mathrm{lo}}^2-w_{\mathrm{td}}^2) - dm(4km-d^2)w_{\mathrm{td}}(\frac{\mathrm{d}w_{\mathrm{lo}}}{\mathrm{d}d})}{(4km-d^2)(d/k)(2W_{\mathrm{lo}}+dw_{\mathrm{lo}}\dot{w}_{\mathrm{lo}})}
\end{aligned}
.
$$

Subtracting the second equation from the first one, we obtain

$$
t_{\mathrm{lo}} + d\frac{\mathrm{d}t_{\mathrm{lo}}}{\mathrm{d}d} = \mathcal{E}_1 + \mathcal{E}_2 + \frac{kmw_{\mathrm{td}}}{2W_{\mathrm{lo}}+dw_{\mathrm{lo}}\dot{w}_{\mathrm{lo}}}\frac{\mathrm{d}w_{\mathrm{lo}}}{\mathrm{d}d} \tag{2.23}
$$

with

$$
\begin{aligned}
\mathcal{E}_1 &:= \frac{8km^2}{(\sqrt{4km-d^2})^3}\left[2\pi + \arctan\frac{\dot{w}_{\mathrm{td}}\sqrt{4km-d^2}}{2kw_{\mathrm{td}}+d\dot{w}_{\mathrm{td}}} - \arctan\frac{(w_{\mathrm{lo}}-w_{\mathrm{td}})\sqrt{4km-d^2}}{d(w_{\mathrm{lo}}+w_{\mathrm{td}})}\right] \\
\mathcal{E}_2 &:= \frac{2(km)^2(w_{\mathrm{td}}^2-w_{\mathrm{lo}}^2)}{d(4km-d^2)(2W_{\mathrm{lo}}+dw_{\mathrm{lo}}\dot{w}_{\mathrm{lo}})} - \frac{dm\dot{w}_{\mathrm{td}}(2m\dot{w}_{\mathrm{td}}+dw_{\mathrm{td}})}{(4km-d^2)(2W_{\mathrm{td}}+dw_{\mathrm{td}}\dot{w}_{\mathrm{td}})}
\end{aligned}
.
$$

Now that we have obtained an explicit expression for the liftoff time-related terms as a function of liftoff position w_{lo}, (2.21) can be rewritten as

$$
\frac{\mathrm{d}\widetilde{W}_{\mathrm{lo}}}{\mathrm{d}d} = e^{-t_{\mathrm{lo}}\frac{d}{m}}\left[\frac{1}{2}w_{\mathrm{td}}\dot{w}_{\mathrm{td}} - \frac{\mathcal{E}_1+\mathcal{E}_2}{m}(W_{\mathrm{td}} + \frac{1}{2}dw_{\mathrm{td}}\dot{w}_{\mathrm{td}})\right] < 0,
$$

which can be satisfied by ensuring

$$
\frac{\mathcal{E}_1+\mathcal{E}_2}{m}(W_{\mathrm{td}} + \frac{1}{2}dw_{\mathrm{td}}\dot{w}_{\mathrm{td}}) - \frac{1}{2}w_{\mathrm{td}}\dot{w}_{\mathrm{td}} > 0. \tag{2.24}
$$

Observe, first, that feasible damping ratio range $\xi \in [-0.5, +0.5]$ leads to

$$
W + \frac{1}{2}dw\dot{w} = \frac{(w\sqrt{k}+\dot{w}\sqrt{m})^2 + (d-2\sqrt{km})w\dot{w}}{2} > \frac{(w\sqrt{k}+\dot{w}\sqrt{m})^2}{2} > 0,
$$

allowing us to rewrite the inequality (2.24) as

$$
\mathcal{I} := \frac{\mathcal{E}_1+\mathcal{E}_2}{m} - \frac{w_{\mathrm{td}}\dot{w}_{\mathrm{td}}}{2W_{\mathrm{td}}+dw_{\mathrm{td}}\dot{w}_{\mathrm{td}}} > 0. \tag{2.25}
$$

Substituting explicit forms of $\mathcal{E}_1$ and $\mathcal{E}_2$ into this and reusing the liftoff condition (2.19) yields

$$
\begin{aligned}
\mathcal{I} =& \frac{8km}{\sqrt{4km-d^2}}\left[2\pi + \arctan\frac{\dot{w}_{\mathrm{td}}\sqrt{4km-d^2}}{2kw_{\mathrm{td}}+d\dot{w}_{\mathrm{td}}} - \arctan\frac{\dot{w}_{\mathrm{lo}}\sqrt{4km-d^2}}{2kw_{\mathrm{lo}}+d\dot{w}_{\mathrm{lo}}}\right] \\
&+ \left(\frac{2mk^2(w_{\mathrm{td}}^2-w_{\mathrm{lo}}^2)}{d(2W_{\mathrm{lo}}+dw_{\mathrm{lo}}\dot{w}_{\mathrm{lo}})} - \frac{2dm\dot{w}_{\mathrm{td}}^2+4kmw_{\mathrm{td}}\dot{w}_{\mathrm{td}}}{2W_{\mathrm{td}}+dw_{\mathrm{td}}\dot{w}_{\mathrm{td}}}\right)
\end{aligned}
> 0.
$$

The upper and lower bounds for $\arctan$ *terms can be defined as*

$$-\frac{\pi}{2} \leq \arctan \frac{\dot{w}_{\text{td}}\sqrt{4km-d^2}}{2kw_{\text{td}}+d\dot{w}_{\text{td}}} \leq \frac{\pi}{2}$$
$$-\frac{\pi}{2} \leq \arctan \frac{\dot{w}_{\text{lo}}\sqrt{4km-d^2}}{2kw_{\text{lo}}+d\dot{w}_{\text{lo}}} \leq \frac{\pi}{2}$$

which reduces the inequality (2.25) to

$$\mathcal{I} > \frac{8\pi km}{\sqrt{4km-d^2}} + \frac{2mk^2(w_{\text{td}}^2 - w_{\text{lo}}^2)}{d(2W_{\text{lo}} + dw_{\text{lo}}\dot{w}_{\text{lo}})} - \frac{2dm\dot{w}_{\text{td}}^2 + 4kmw_{\text{td}}\dot{w}_{\text{td}}}{2W_{\text{td}} + dw_{\text{td}}\dot{w}_{\text{td}}} > 0. \quad (2.26)$$

An alternative expression for this inequality can be obtained by substituting w_{td} *in the second term with its solution to the liftoff condition (2.19) as*

$$\mathcal{I} > \frac{8\pi km}{\sqrt{4km-d^2}} + \frac{2dm\dot{w}_{\text{lo}}^2 + 4kmw_{\text{lo}}\dot{w}_{\text{lo}}}{2W_{\text{lo}} + dw_{\text{lo}}\dot{w}_{\text{lo}}} - \frac{2dm\dot{w}_{\text{td}}^2 + 4kmw_{\text{td}}\dot{w}_{\text{td}}}{2W_{\text{td}} + dw_{\text{td}}\dot{w}_{\text{td}}} > 0. \quad (2.27)$$

Now, we provide some upper and lower bounds for the terms in this inequality before proceeding to completing the proof of $\mathbb{I}$ *inequality. In this regard, using the feasible values of damping ratios, that can be identified with representative range* $\xi \in [-0.5, 0.5]$, *we, first, show that denominators of second and third terms can be shown to be positive as*

$$\begin{aligned} 2W_{\text{td}} + dw_{\text{td}}\dot{w}_{\text{td}} &> 2W_{\text{td}} + 2(\sqrt{km})w_{\text{td}}\dot{w}_{\text{td}} > (\dot{w}_{\text{td}}\sqrt{m} + w_{\text{td}}\sqrt{k})^2 > 0 \\ 2W_{\text{lo}} + dw_{\text{lo}}\dot{w}_{\text{lo}} &> 2W_{\text{lo}} - 2(\sqrt{km})|w_{\text{lo}}|\dot{w}_{\text{lo}} > (\dot{w}_{\text{lo}}\sqrt{m} - w_{\text{lo}}\sqrt{k})^2 > 0 \end{aligned}.$$

Secondly, we focus on the numerators to show

$$\begin{aligned} -(2dm\dot{w}_{\text{td}}^2 + 4kmw_{\text{td}}\dot{w}_{\text{td}}) = -2m\dot{w}_{\text{td}}(d\dot{w}_{\text{td}} + 2kw_{\text{td}}) > 0 &\implies 2kw_{\text{td}} + d\dot{w}_{\text{td}} > 0 \\ 2dm\dot{w}_{\text{lo}}^2 + 4kmw_{\text{lo}}\dot{w}_{\text{lo}} = 2m\dot{w}_{\text{lo}}(d\dot{w}_{\text{lo}} + 2kw_{\text{lo}}) > 0 &\implies 2kw_{\text{lo}} + d\dot{w}_{\text{lo}} > 0 \end{aligned}.$$

Consider, first, the term $T_{\text{td}} := 2kw_{\text{td}} + d\dot{w}_{\text{td}}$*. As* $\dot{w}_{\text{td}} < 0$ *and* $w_{\text{td}} = mg/k$*, this term has to be positive for* $d \leq 0$*. For the other case,* $d > 0$*, we use the proof by contradiction and assume that* $T_{\text{td}} < 0$*, which is contrary to the statement to be proved. Substituting* $w_{\text{td}} = mg/k$ *into this term requires*

$$\dot{w}_{\text{td}} < -\frac{2mg}{d}.$$

On the other hand, we know that the touchdown acceleration should be negative $\ddot{w}_{\text{td}}$ *to avoid foot rebounding. In this regard, plugging this velocity inequality into the stance dynamics, we obtain a contradiction*

$$\ddot{w}_{\text{td}} = -g - \frac{d}{m}\dot{w}_{\text{td}} > g > 0,$$

which indirectly proves the claim $T_{\mathrm{td}} > 0$*. Consider, now, the remaining term* $T_{\mathrm{lo}} := 2kw_{\mathrm{lo}} + d\dot{w}_{\mathrm{lo}} = (2mk^2/d)(w_{\mathrm{td}}^2 - w_{\mathrm{lo}}^2)$*. Using the liftoff condition (2.19), this term can be expressed in an alternative form as*

$$T_{\mathrm{lo}} = 2kw_{\mathrm{td}} - d\dot{w}_{\mathrm{lo}} = 2mg - d\dot{w}_{\mathrm{lo}} \quad .$$

For $d \leq 0$*, it is obvious that* $T_{\mathrm{lo}} > 0$*. For the remaining case,* $d > 0$*, the liftoff condition translates to* $w_{\mathrm{lo}} = w_{\mathrm{td}} - \frac{d}{k}\dot{w}_{\mathrm{lo}} < w_{\mathrm{td}}$*, which leads to the proof of* $T_{\mathrm{lo}} > 0$ *with*

$$T_{\mathrm{lo}} = (2mk^2/d)(w_{\mathrm{td}}^2 - w_{\mathrm{lo}}^2) > 0.$$

Now that we have shown

$$\begin{aligned} \frac{2dm\dot{w}_{\mathrm{lo}}^2 + 4kmw_{\mathrm{lo}}\dot{w}_{\mathrm{lo}}}{2W_{\mathrm{lo}} + dw_{\mathrm{lo}}\dot{w}_{\mathrm{lo}}} &> 0 \\ -\frac{2dm\dot{w}_{\mathrm{td}}^2 + 4kmw_{\mathrm{td}}\dot{w}_{\mathrm{td}}}{2W_{\mathrm{td}} + dw_{\mathrm{td}}\dot{w}_{\mathrm{td}}} &> 0 \end{aligned},$$

we can rewrite the inequality (2.27) with a tighter bound by neglecting second and third terms as

$$\mathcal{I} > \frac{8\pi km}{\sqrt{4km - d^2}} > 0,$$

which completes the proof. □

Theorem 1. *For a given* h_k*, the return map is invertible, admitting*

$$d = \mathcal{R}^{-1}(h_k, h_{k+1})$$

.

Proof. *Monotonicity of* $\mathcal{R}(h_k, d)$ *for a given* h_k *on the interval* D *implies that image of the return map is a closed interval with*

$$H = [\mathcal{R}(h_k, d_{\min}), \mathcal{R}(h_k, d_{\max})] \, .$$

In this regard, the return map is surjective when restricted to $\mathcal{R}(h_k, \cdot) : D \to H$*. Furthermore,* $\mathcal{R}(h_k, d)$ *is injective because of monotonicity, hence yielding that* $\mathcal{R}(h_k, d)$ *is invertible.* □

Theorem 2. *A proportional control law*

$$d(h_k) = -\kappa(h^\star - h_k) \tag{2.28}$$

renders $h = h^\star$ a global asymptotically stable point of the system $h_{k+1} = \mathcal{R}(h_k, d(h_k))$ for any feedback gain

$$-\frac{2}{\mathcal{R}'_{\min}(d)} > \kappa > 0$$

with

$$\mathcal{R}'_{\min}(d \in D) = \min_d \mathcal{R}'(d).$$

Proof. *We will prove the Theorem by showing the Lyapunov stability of the discrete dynamical system $h_{k+1} = \mathcal{R}(h_k, d)$ under the specified feedback law. To this end, consider a function*

$$V(h) = (h - h^\star)^2 \tag{2.29}$$

with $h \in H$. This function is a suitable Lyapunov function candidate to show stability of $h = h^\star$, as it satisfies $V(h^\star) = 0$ and $V(h) > 0 \; \forall h \neq h^\star$. In this regard, for this function to qualify as a suitable Lyapunov function, hence showing the stability, we need

$$V(\mathcal{R}(h_k, d(h_k))) - V(h_k) = 0 \; \forall \quad h_k \in \{h^\star\}\,. \tag{2.30}$$

$$V(\mathcal{R}(h_k, d(h_k))) - V(h_k) < 0 \; \forall \quad h_k \in H - \{h^\star\}. \tag{2.31}$$

Before proceeding to the proof of this inequalities, observe that

$$h_k = \mathcal{R}(h_k, 0)$$

since $d = 0$ results in an energetically conservative system with $h_{k+1} = h_k$. This observation automatically verifies (2.30). On the other hand, using this observation again, (2.31) can be alternatively written as

$$V(\mathcal{R}(h_k, d(h_k))) - V(h_k) = V(\mathcal{R}(h_k, d(h_k))) - V(\mathcal{R}(h_k, 0)) < 0.$$

Using the explicit form of V given in (2.29), we can express this condition more explicitly as

$$\left(\mathcal{R}(h_k, d(h_k)) - \mathcal{R}(h_k, 0)\right)\left(\mathcal{R}(h_k, d(h_k)) + \mathcal{R}(h_k, 0) - 2h^\star\right) < 0. \tag{2.32}$$

In this regard, we, first, observe

$$\operatorname{sgn}\left(\mathcal{R}(h_k, d(h_k)) - \mathcal{R}(h_k, 0)\right) = \operatorname{sgn}(h^\star - \mathcal{R}(h_k, 0))$$

since $d(h_k) = -\kappa(h^\star - h)$ *and* $d_a \lesseqgtr d_b \iff \mathcal{R}(h_k, d_a) \gtreqless \mathcal{R}(h_k, d_b)$. *This lets us rewrite (2.32) in a more refined form as*

$$\operatorname{sgn}(h^\star - h_k)\,(\mathcal{R}(h_k, d(h_k)) + \mathcal{R}(h_k, 0) - 2h^\star) < 0. \tag{2.33}$$

The proof of this inequality will be presented for two complementary cases of (2.31): $h^\star - h_k > 0$ *and* $h^\star - h_k < 0$.

Consider, first, $h^\star - h_k > 0$*, leading to* $d(h_k) < 0$*. In this case, the stability condition (2.33) translates to*

$$\mathcal{R}(h_k, d(h_k)) + \mathcal{R}(h_k, 0) - 2h^\star < 0. \tag{2.34}$$

By Mean Value Theorem, there exists $d_c \in [d(h_k), 0]$ *satisfying*

$$\frac{\mathcal{R}(h_k, d(h_k)) - \mathcal{R}(h_k, 0)}{d(h_k)} = \mathcal{R}'(d_c).$$

Since $\mathcal{R}'_{\min} \leq \mathcal{R}'(d_c) < 0$ *by Lemma 1, we can find an upper bound for* $\mathcal{R}(h_k, d(h_k))$ *as*

$$\mathcal{R}(h_k, d(h_k)) \leq \mathcal{R}(h_k, 0) + d(h_k)\mathcal{R}'_{\min} = h_k + \kappa(h_k - h^\star)\mathcal{R}'_{\min},$$

which can be substituted into (2.34) to obtain a more strict stability condition as

$$\mathcal{R}(h_k, d(h_k)) + \mathcal{R}(h_k, 0) - 2h^\star < (2 + \kappa\mathcal{R}'_{\min})(h_k - h^\star) < 0.$$

This inequality is automatically satisfied by the condition given in the Theorem for κ*, hence completing* $h^\star - h_k > 0$ *part of the proof.*

Consider, now, the remaining case $h^\star - h_k < 0$*, where we have* $d(h_k) > 0$*, translating the stability condition (2.33) to*

$$\mathcal{R}(h_k, d(h_k)) + \mathcal{R}(h_k, 0) - 2h^\star > 0. \tag{2.35}$$

By Mean Value Theorem, there exists $d_c \in [0, d(h_k)]$ *satisfying*

$$\frac{\mathcal{R}(h_k, d(h_k)) - \mathcal{R}(h_k, 0)}{d(h_k)} = \mathcal{R}'(d_c).$$

Since $\mathcal{R}'_{\min} \leq \mathcal{R}'(d_c) < 0$ *by Lemma 1, we can again find a lower bound for* $\mathcal{R}(h_k, d(h_k))$ *as*

$$\mathcal{R}(h_k, d(h_k)) \geq \mathcal{R}(h_k, 0) + d(h_k)\mathcal{R}'_{\min} = h_k + \kappa(h_k - h^\star)\mathcal{R}'_{\min}.$$

Substituting the lower bound into the stability condition (2.35) yields

$$\mathcal{R}(h_k, d(h_k)) + \mathcal{R}(h_k, 0) - 2h^\star > (2 + \kappa \mathcal{R}'_{\min})(h_k - h^\star) > 0,$$

which is automatically satisfied by the κ stability condition given in the Theorem, hence completing the proof. □

2.2.4.2 Variable Damping Control

We formulate our gait controller in a deadbeat structure, relying on the inverse of the return map to yield

$$d = \mathcal{R}^{-1}(h_k, h^\star) \ , \tag{2.36}$$

where $h^\star$ denotes the desired apex height to be achieved in a single stride. As shown in Section 2.2.4.1, the return map $\mathcal{R}$ is an invertible function of d, thus admitting an efficient numerical solution. This takes the form of a simple root finding problem expressed in liftoff coordinates as $\underset{d}{\text{solve}} \left(mg \ z_{lo,k}(d) + \frac{1}{2} \dot{z}^2_{lo,k}(d) - g \ h^\star = 0 \right)$, where the dependence of liftoff states on the control input d are explicitly shown. Once d is computed, it can be virtually realized by (2.13) Figure 2.4 illustrates an example run with this strategy marked as the solid blue line with $h_k = 1.2m$ and $h^\star = 1.5m$ for a human sized model with $z_0 = 1m$, $m = 70kg$, $k = 10kN/m$, and $d_p = 100Ns/m$.

2.2.5 Variable Stiffness Control

One of the more commonly used alternatives for analytically tractable control of the SLIP model relies on changing the effective spring constant of the leg, either through mechanical linkages [50] or using active force control on a structure such as the VA-SLIP model. In the latter case, the actuator position required to realize a desired stiffness k' takes the form

$$\delta(t) = \frac{k - k'}{k}(z(t) - z_0) \ . \tag{2.37}$$

Usually, analytic tractability is obtained by assuming a step change in stiffness at the bottom instant, enabling the stance map to be studied in two parts. An example run with the VA-SLIP model under this controller is shown in Figure 2.4 as the dot-dashed

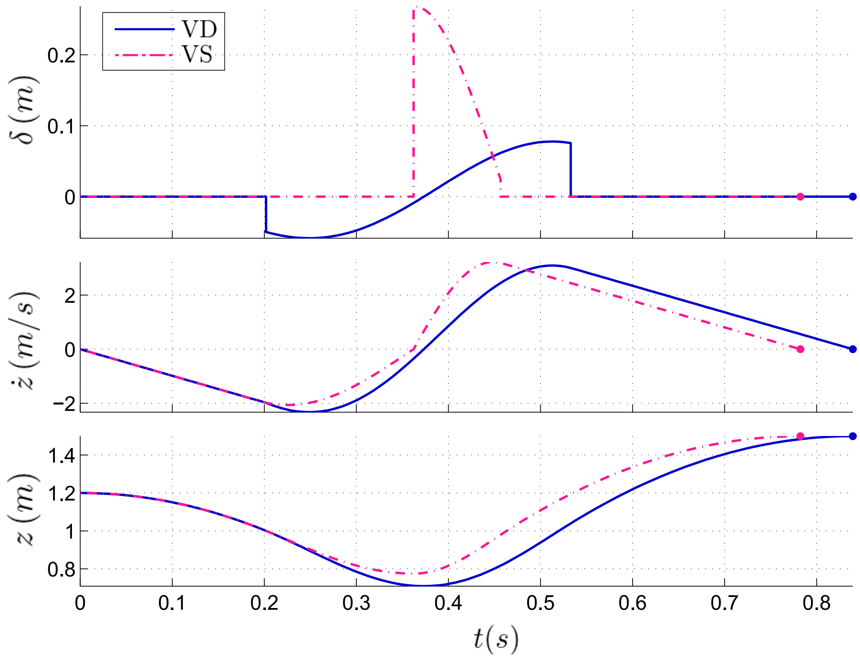

Figure 2.4: Example simulation plots of actuator input (top), vertical velocity (middle) and vertical position (bottom) with constant d throughout stance (solid blue) and step stiffness change at bottom (dot-dashed red). End of the stride in each case is marked with a colored dot.

red plot. In subsequent sections, we will provide a comparative study of this method in relation to our method.

2.2.6 Actuator Limitations and Practical Considerations

As evident from the example run in Figure 2.4 with constant virtual damping d, there are discontinuities in $\delta(t)$ at touchdown and liftoff. Even though the discontinuity at liftoff is not a problem since the actuator can be quickly rewound during flight, the necessity of having $z = z_0$ at touchdown requires $\delta(t_{\mathrm{td}}) = 0$ at touchdown. The stiffness control method of (2.37) exhibits a similar discontinuity in actuator position at the bottom instant.

Such discontinuities clearly cannot be realized by any physical position-controlled actuator. Consequently, we must consider controller performance under actuator limitations in order to ensure their practical applicability. In particular, we will consider a realistic DC motor model [34] wherein the actuator speed is limited by its force according to the torque-speed curve as

$$|\dot{\delta}(t)| < \dot{\delta}_{\max}(1 - |F|/F_{\max}) \ , \tag{2.38}$$

where F denotes the current force exerted on the actuator by the leg spring, and $F_{\max}$ is the maximum actuator force.

2.3 Controller Performance and Efficiency

In this section, we present a comparative study of the energetic performance and controller accuracy for gait control methods we described in Section 2.2. We first evaluate the energetic effectiveness of both methods in Section 2.3.1 based on the maximum amount of energy they can inject into the system within a single stride. We then investigate the accuracy of single-stride deadbeat control in Section 2.3.2. Finally, we compare power requirements of these methods on the actuator, establishing that the tunable damping idea allow platform designs with smaller actuators and better efficiency. All our simulation results in this section consider a human-sized platform with $z_0 = 1m$ and $m = 70kg$.

2.3.1 Effectiveness of Energy Input

One of the physical constraints associated with robot designs using a linear actuator in series with the leg spring is the limited range of displacements for the actuator. In this section, we establish upper bounds on the amount of energy that can be injected into the VA-SLIP system using both control methods described in Section 2.2 by considering only the range constraint $|\delta(t)| < \delta_{\max}$, assuming that the actuator can otherwise supply required forces and velocities. Figure 2.5 shows our results from simulation runs with $\delta_{\max} = 0.2m$, starting from initial conditions in the range $z(0) \in [1.1, 2.5]m$ and different leg stiffnesses in the range $k \in [10, 40]kN/m$. Maximum achievable increase in apex height was computed for each controller enforcing $|\delta(t)| < \delta_{\max}$, and the results were averaged for different physical damping coefficients in the range $d_p \in [100, 500]Ns/m$. As expected, the stiffness controller has the

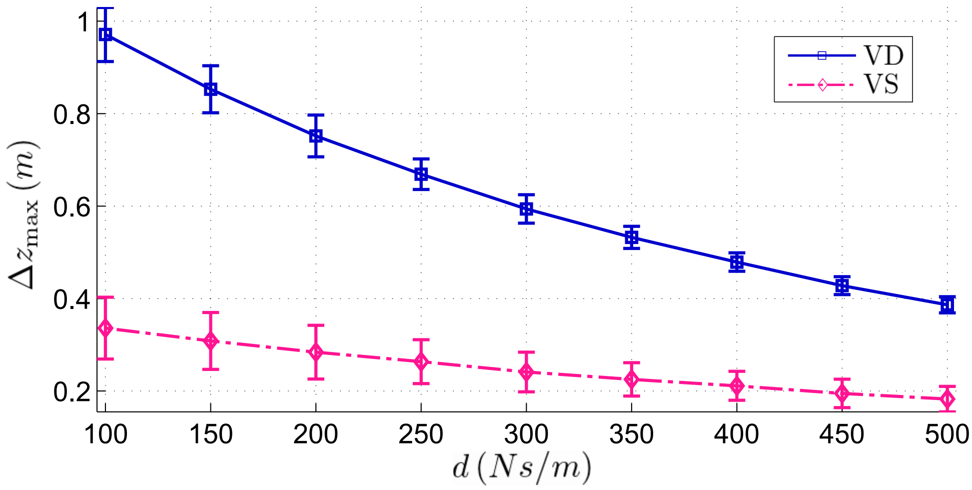

Figure 2.5: Maximum height gain $\Delta y = z^{\star} - z(0)$ that can be achieved using different control strategies as a function of the physical leg damping d_p with $\delta_{\max} = 0.2m$, averaged over $z(0) \in [1.1, 2.5]m$, $k \in [10, 40]kN/m$. Error bars correspond to the standard deviation across different initial conditions and spring stiffness values.

lowest energy injection performance since it is limited to decompression and requires a large initial displacement. For similar reasons, the decompression-only damping controller is limited in its energy injection capability. However, both the ideal damping controller and the ramp-up damping have similar performance, with up to $1m$ height gain in a single stride, showing that they can effectively use the entire stride to inject energy into the system for the best effectiveness.

2.3.2 Accuracy of Deadbeat Control

Having established that the ramp-up damping controller outperforms its alternatives in being able to supply the most energy within a single stride, we now investigate its accuracy when additional actuator limitations described in Section 2.2.6 are introduced. To this end, we use a maximum actuator velocity of $\dot{\delta}_{\max} = 2m/s$ and a maximum force of $F_{\max} = 10kN$, motivated by motor choices in the ATRIAS 2.1 robot scaled to the size and weight of our platform. We run simulations covering initial conditions and spring stiffnesses in the same ranges as Section 2.3.1, while considering height difference commands in the range $\Delta z := z^{\star} - z(0) \in [-0.5, 0.5]m$. We

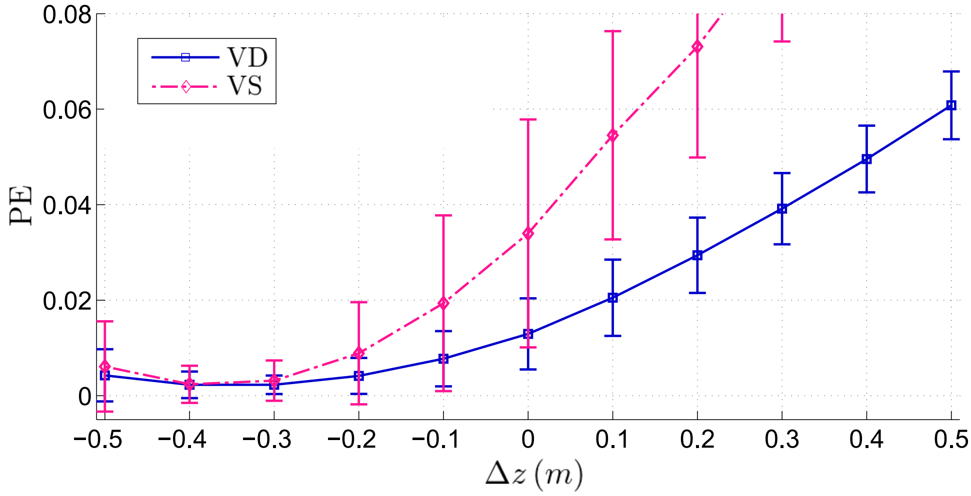

Figure 2.6: Percentage height tracking error using different control strategies with $\delta_{\max} = 0.2m$, $\dot{\delta}_{\max} = 2m/s$ and $F_{\max} = 10kN/m$, averaged across $d_p \in [100, 500]Ns/m$, $z(0) \in [1.1, 2.5]m$, $k \in [10, 40]kN/m$. Error bars correspond to the standard deviation across different initial conditions and parameter values.

evaluate controller performance with a *percentage error*, defined as

$$PE_{z^\star} := \frac{|z^\star - z_1|}{z^\star}\,, \tag{2.39}$$

where z_1 denotes the next apex height reached at the end of the stride. Figure 2.6 shows average percentage error across different simulations with respect to desired height differences.

Our results show that the accuracy of the stiffness controller is the worst since it requires a step change at bottom which is impossible to realize with realistic actuators. The bottom instant is also when the spring force is largest, challenging the actuator's power constraints. Similarly, since the ideal damping controller also assumes a discontinuous actuator position at touchdown, its accuracy worsens as the desired height difference increases. Damping control limited to decompression does well in a certain range, until its demand on the actuator speed exceeds practical limits beyond which its performance degrades substantially. Since the ramp-up damping controller eliminates discontinuities in the desired actuator position and spreads out energy pumping throughout the entire stance, its accuracy remains consistently low for a large range of desired height differences. Finally, it is informative to note that when the desired height difference is close to $-0.35m$, the physical damping in the system does most of the work, eliminating the need for explicit control and increasing the accuracy of all controllers.

2.3.3 Actuator Power Requirements

Finally, this section presents improvements in actuator power requirements under each of the different gait control methods. To this end, we focus on a single choice of leg parameters with $k = 10000N/m$ and $d_p = 100Ns/m$, using an initial robot height of $z(0) = 1.6m$ with different commanded height differences in the range $\Delta y \in [-0.5, 0.5]m$. Actuator limits were chosen to be the same as Section 2.3.2, with maximum and average power requirements through the stride, $P_{\max}$ and P_{avg} respectively, defined as

$$P_{\max} := \max_{t \in [t_t, t_l]} (|\dot{\delta}(t) F_{spring}(t)|) \tag{2.40}$$

$$P_{avg} := \frac{1}{t_f} \int_{t_t}^{t_l} |\dot{\delta}(\tau) F_{spring}(\tau)| d\tau \ , \tag{2.41}$$

where t_t and t_l denote the touchdown and liftoff times, and $F_{spring}(t)$ denotes the spring force at time t. Figure 2.7 shows our simulation results.

Our results show that the stiffness control has the highest power requirements as expected, attempting to inject most of the energy at bottom where the spring force is largest. The damping adjustment limited to decompression performs better but still has substantial power requirements. The ideal damping control and the ramp-up damping perform best, with a dramatic reduction in power requirements for small changes in apex height, until the actuator saturates altogether beyond $\Delta y > 0.5m$. Note, also, that the natural damping in the system around $\Delta y \approx -0.25m$ eliminates the need for any actuation, which is why power requirements on the actuator all vanish at that point.

These comparative results show that the novel gait control method we proposed through active tuning of the system's damping coefficient has the best performance in terms of effective energy injection, controller accuracy and power requirements. As such, it provides a robust, effective and accurate method for controlling running behaviors.

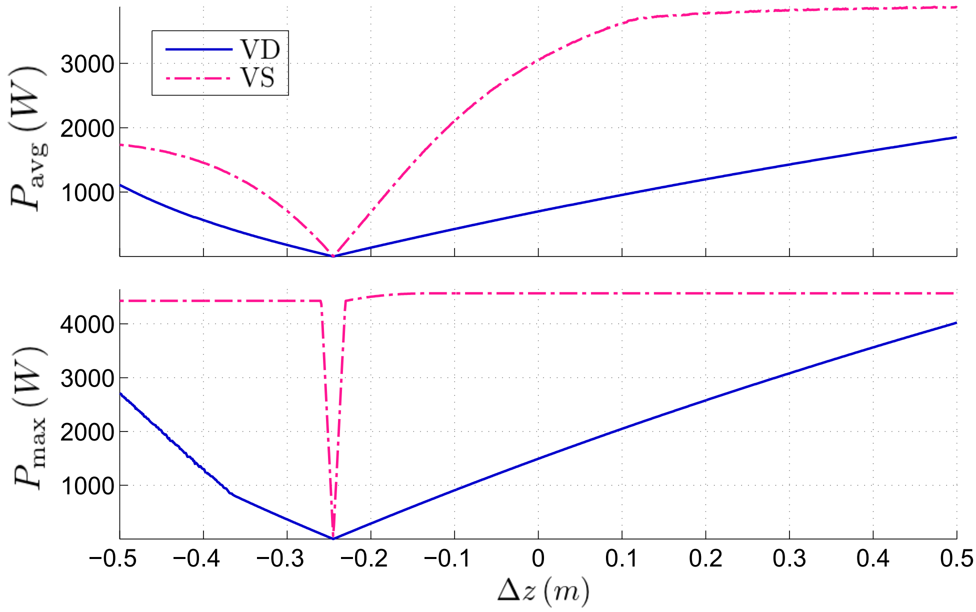

Figure 2.7: Dependence of average (top) and maximum (bottom) actuator power on the commanded height difference for different controllers. Simulations were run for a particular leg with $k = 10000N/m$ and $d_p = 100Ns/m$ and an initial height $z(0) = 1.6m$. Note that power data are saturated for visibility purposes.

2.4 Conclusion

In this chapter, we introduced a new control strategy for running robots that incorporate a linear actuator in series with the leg compliance. Our strategy is based on tuning the damping of a virtual unactuated leg attached to the robot body, preserving the spring-mass-damper structure and solutions of radial SLIP dynamics [88]. We present our derivations and controller design on a simpler, vertical model, noting that they can readily be extended to planar running models. Our simulation studies show that the proposed strategy and its extensions to address physical considerations yield more efficient energy injection within a stride, smaller power requirements on the actuator and better control accuracy under physical actuator limitations in comparison to an alternative control strategy that relies on active regulation of leg stiffness.

CHAPTER 3

CONTROL OF PLANAR SPRING-MASS RUNNING THROUGH VIRTUAL TUNING OF RADIAL LEG DAMPING

In Chapter 2, we proposed to virtually tune leg viscous damping in order control energy in spring-mass hopping. In this chapter, generalizing this idea to planar motion, we present a gait control strategy to realize a desired running gait in two dimensions. While doing so, a novel framework, which will be used throughout this thesis, is introduced for the realization of model-based control towards this goal. The work in this chapter has also been reported and appeared in [95].

3.1 Introduction

Despite numerous advantages in locomotory dexterity, versatility and efficiency that can ultimately be achieved by legged morphologies, there are still substantial challenges in the realization of these features on legged robots. Energetic efficiency, both for steady state and transient steps, is among these challenges, requiring careful tuning of system dynamics and morphology to minimize possible sources of energy loss, channelling as much actuator power to useful, non-negative work as possible while maintaining stability and accuracy. Not suprisingly, this is a difficult problem that requires co-design of the robot morphology together with control algorithms that can make effective and efficient use of the resulting dynamics.

Walking and running behaviors received considerable attention in this context, with research in both biomechanics and robotics focusing on characterizing both energetic properties of these behaviors as well as morphologies on which they are realized.

Interestingly, research in this area revealed that perfect efficiency can be achieved with very simple dynamic models for both walking and running behaviors. In particular, the Compass Gait model for walking behaviors with infinitesimal foot masses can walk indefinitely on almost flat ground with infinitesimal inclination [28]. Similarly, the lossless Spring-Loaded Inverted Pendulum Model can run indefinitely without any energy input on flat ground [92]. The elimination of energetic concerns in this fashion allowed researchers to focus on characterizing and improving stability of steady-state behavior. Subsequently, control authority over the system energy was recovered through carefully selected extensions that preserved the simplicity of underlying models, including instantaneous changes in leg stiffness and leg precompression for running, as well as impulsive ankle or hip actuation for walking. These idealized extensions inherit the efficiency of the basic models, but provide additional control affordance to achieve authority over all fundamental degrees of freedom.

Unfortunately, there still remains a gap between these efficient but idealized models and physical platforms designed to realize the same locomotory behaviors in an efficient manner. Despite biomechanical evidence in support of such ideal "template" models being embedded within more complex, higher degree of freedom "anchor" morphologies [27], it has been challenging to achieve similarly effective control of complex robotic platforms. Walking behaviors have been easier to implement on physical platforms than running for a variety of reasons, including the lower dimensionality of associated models and the accuracy of models for rigid linkages. Running robots, on the other hand, often deviate substantially from idealized models, with additional sources of energy loss as well as complex and nonlinear leg compliance and actuation mechanisms. Even though spring-mass running have been successfully demonstrated in many platforms, it has been more challenging to combine both energetic efficiency and accuracy of control in the same platform for running behaviors, particularly on rough terrain where transient steps dominate and system energy must be regulated effectively.

Raibert's runners [84, 83], being the first robots capable of dynamic running, did not place particular emphasis on energetic efficiency or accuracy of control, but used an intuitive decoupling of locomotory degrees of freedom to achieve stable locomotion. Subsequently, the ARL family of monopods [33, 3] introduced series-elastic actuation in the leg and the hip to achieve substantial improvements in energetic efficiency, but were not yet able to combine these properties with control accuracy since models and solutions for the proposed actuation mechanisms were not yet available. A structurally different but equally efficient actuation mechanism for SLIP running was introduced by the Bow Leg robot [121], which relied on pre-compression the leg spring during flight to store elastic energy which was then released during stance. It was difficult, however, to build accurate models for this morphology due to the nonlinear compliance and damping properties of the leg.

More recent bipeds MABEL [38, 104] and ATRIAS [85, 67, 46] were designed with a stronger emphasis on efficiency and the goal of matching the robot's overall dynamics to those of the SLIP model by using tunable compliance and series elastic actuation, respectively [60]. Nevertheless, significant actuator dynamics and the complex mechanical structure of these platforms still introduce inefficiencies [1], particularly in the presence of controllers that seek to achieve accurate embedding of SLIP dynamics together with stable and robust locomotory behaviors at the expense of energetic and power efficiency [21]. Some platforms go in the opposite direction and eliminate passive compliance altogether, relying on direct drive actuation to obtain accurate realization of SLIP dynamics [55]. Alternative methods based on feedback linearization with series-elastic actuation have also been proposed, but their main focus has been on accuracy at the expense of energetic efficiency [78, 79, 40]. In any case, even though these platforms and control methods have been successful in matching fundamental locomotory models such as the SLIP [68], and achieve impressive energetic efficiency for steady-state locomotion, there is considerable room for improvement for applications involving rough terrain traversal where transient steps dominate and effective footstep planning and control require models that are both accurate and efficient [10].

The work in this chapter is motivated by the ideas presented in the previous chapter and [88], introducing novel extentions and improvements to achieve accurate, power and energy efficient and computationally simple control of non-steady-state saggittal plane running with substantial changes in system energy within each step. In particular, we extend the use of the concept of virtually tunable damping for the vertically constrained VD-SLIP model proposed in Chapter 2 to a much more useful, 2D, saggittal plane model. In addition to this structural generalization and associated improvements to approximate analytic solutions that were introduced in [88], we propose to add a new "constant forcing" component into the template model [27], allowing us to altogether eliminate discontinuities in position and velocity commands for a radial series-elastic actuator on the leg. This allows a much more accurate realization of the virtually tunable damping concept on more realistic platform models with substantial actuator inertia. In order to realize the resulting, seemingly unrealistic SLIP-like template model, we propose a hierarchy of template models towards a realistic, serially actuated leg model, providing controllers to embed the dynamics of each template into its neighboring "anchor" system. This allows a relatively simple translation of a new single-step deadbeat control policy that we formulate for the generalized SLIP model, to an anchor system with complex dynamics that does not admit analytic solutions. Finally, we provide simulations to show that our overall approach yields substantial improvements for energy and power efficiency as well as accuracy of control for transient steps with a wide range of commanded changes in system states.

3.2 A Hierarchical Template/Anchor Framework for Modeling and Control

The realization of locomotory behaviors on legged morphologies entails numerous challenges, particularly when dynamic dexterity is desired to obtain increased performance with less stringent actuator and power requirements. The underlying dynamics are often high degree-of-freedom (DOF), hybrid and nonlinear, requiring complex mechanisms for coordination, stabilization and control. Motivated by both this complexity, as well as the observation of similar principles in the biomechanics of a wide range of legged animals, the decompositional, *templates and anchors* approach was proposed [27], wherein simple, low DOF template models that capture essential aspects of locomotory behaviors are dynamically "embedded" in more complex models that incorporate the remaining complexity. It is of course still questionable whether such a decomposition of control effort is necessary and whether it is explicitly present in biological locomotors. Nevertheless, this approach is certainly beneficial in the synthesis of locomotory controllers since it allows decoupled focus on the stability

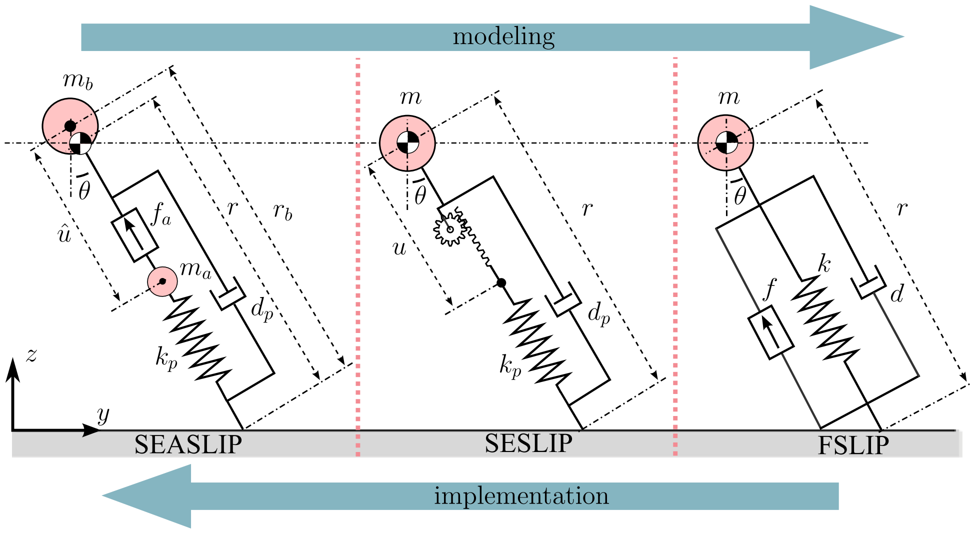

Figure 3.1: A hierarchy of progressively simpler templates for planar running behaviors starting from the anchor model with series elastic actuation on the left (SEASLIP) to the lossy SLIP template with parallel force actuator (FSLIP) on the right.

and control of the basic locomotory behavior of interest. Many recent studies in the literature make use of this approach not only to synthesize effective locomotory controllers, but to also obtain theoretical conclusions about stability and performance [7, 21]. In this chapter, we extend this approach with a hierarchical structure, introducing multiple levels of abstraction between the simple template and the complex anchor models. Our focus on planar running behaviors with support for transient and energetically non-conservative gaits suggests the use of the SLIP model with necessary extensions as a high-level template. From among alternatives studied in the literature, we have chosen to adopt series-elastic radial actuation for regulating system energy due to its practical advantages as evidenced by a successful instantiations in the literature [46, 108, 3, 83]. We have also not considered using hip torque for energy regulation [97, 6], since hip actuation is often better suited stabilizing body attitude rather than accurate control of system energy [83, 46]. Based on these observations, we introduce a new SLIP model, augmented with viscous damping and a constant radial forcing term, FSLIP, as our gait-level template model as shown in the leftmost model in Figure 3.1 and detailed in Section 3.3.3. Starting from the FSLIP model, we consider progressively more complex templates towards a realistic anchor as shown in Figure 3.1. First, we consider a SLIP model with ideal series-elastic actuation with no actuator dynamics (SESLIP model), which allows a relatively simple embedding of the FSLIP dynamics through force control as described in Section 3.4.1. This choice is motivated by the vertical hopping anchor VA-SLIP proposed in Chapter 2, which allows us to formalize whether a particular choice of parameters in FSLIP can be accurately realized on a physical machine through the corresponding, idealized actuator motion. Subsequently, we consider our ultimate anchor, a realistic model with series-elastic actuation (SEASLIP) (see Figure 11 in [49], Figure 1 in [109], and Figure 2.3 in [110] for previous uses of similar models for platforms with series-elastic actuation), which can accurately realize SESLIP through position control of a radial actuator as described in Section 3.4.2. In this framework, adjacent models constitute template/anchor pairs, wherein each model is a simplified representation of the model to its left, and seeks to actively embed the dynamics of the simpler model to its right. Thus, controllers designed for the lower complexity templates will be subsequently embedded into progressively more complex models towards the left, eventually reaching the physical anchor to complete the implementation. Note that the scope of this chapter excludes the embedding of the SEASLIP model into physical platforms, for which existing methods proposed in the literature for specific serially-actuated compliant legged platforms can be used.

Finally, it is important to note that one of our primary goals is to preserve the availability of analytic approximations to system behavior throughout the stride as a basis for gait controller design [112, 68], adaptive control [113] and state estimation [39]. Consequently, we propose the piecewise constant FSLIP template and our hierarchical embedding approach instead of, for example, numerical optimal control methods formulated directly on the complex SEASLIP anchor system. Such an analytical framework also promises to offer substantial reductions in computational requirements [79], allowing real-time implementation of associated control strategies on less demanding hardware that would be easier and more energetically efficient deployment on smaller, lighter and cheaper autonomous mobile robot platforms.

3.3 Dynamics of Template Models

Running behaviors for all three monopedal templates described in Section 3.2 share a common hybrid dynamical structure, going through alternating flight and stance phases, separated by touchdown and liftoff events, triggered respectively by the toe coming in contact with the ground and the vertical ground reaction force during stance becoming zero. In the following sections, we will present the equations of motion for both stance and flight phases for all three models.

3.3.1 SEASLIP: Serially-Actuated Lossy SLIP with Actuator Mass

A common approach among successful physical realizations of the SLIP model is to serially couple an actuator with a spring acting in the radial direction for energy injection and removal either implemented directly [3, 87] or through kinematic linkages [51, 59]. Note, however, that force control bandwidth of the compliant actuator is a fundamental factor in locomotory performance for robots with such morphologies [68]. Therefore, in line with related work [49, 108], we seek to capture relevant locomotory properties of such systems with an extended SLIP model that incorporates a linear force actuator in series to a spring with non-negligible mass and inertia components in between as shown in the SEASLIP model of Figure 3.1. Even though often, there is also an additional rotational degree of freedom in the orientation of the robot body for physical instantiations, its control is generally considered and implemented orthogonally to the SLIP-like center-of-mass (COM) dynamics. Consequently, our focus in this chapter excludes rotational body dynamics (assuming large body inertia to enable leg recirculation during flight through a hip torque input) and focuses on the motion of the COM. We also assume that the electrical dynamics of the actuator are negligible, but that the actuator is subject to practical limits on its force and displacement outputs determined by motor characteristics and mechanical boundaries, respectively. In particular, we enforce a realistic torque speed curve with $f_{min}(\dot{u}) < f_a < f_{max}(\dot{u})$ and limits on the actuator displacement which can be modeled by $|u - u_0| < \Delta u$ where u_0 models the kinematic offset between the physical spring and the actuator.

During stance, we coordinatize the system configuration with the COM position in polar coordinates and the actuator position with $q_{s_1} := [r, \theta, u]^T$. Note that the COM position can be computed with $r = r_b - m_a u/(m_b + m_a)$. Using standard Euler-Lagrange derivations, stance dynamics take the form

$$\boldsymbol{M}_{s_1}\ddot{q}_{s_1} + \boldsymbol{C}_{s_1} + \boldsymbol{G}_{s_1} = \Upsilon_{s_1} \tag{3.1}$$

where the mass matrix $\boldsymbol{M}_{s_1}$, Coriolis and centrifugal force vector $\boldsymbol{C}_{s_1}$, the gravitational force vector $\boldsymbol{G}_{s_1}$ and non-conservative forces Υ_{s_1} are derived as

$$\begin{aligned}
\boldsymbol{M}_{s_1} &:= \begin{bmatrix} m & 0 & 0 \\ 0 & mr^2 + m_b m_a u^2/m & 0 \\ 0 & 0 & J_a + m_b m_a/m \end{bmatrix} \\
\boldsymbol{C}_{s_1} &:= \begin{bmatrix} -mr\dot{\theta}^2 \\ 2mr\dot{r}\dot{\theta} + 2m_b m_a u\dot{u}\dot{\theta}/m \\ -m_b m_a u\dot{\theta}^2/m \end{bmatrix} \\
\boldsymbol{G}_{s_1} &:= \begin{bmatrix} mg\cos\theta + k_p(r - m_b u/m - l_0) \\ -mgr\sin\theta \\ -k_p m_b(r - m_b u/m - l_0)/m \end{bmatrix} \\
\Upsilon_{s_1} &:= [f_d, \tau_h, f_a + m_a f_d/m]^T
\end{aligned}$$

with the total mass defined as $m := m_b + m_a$, the physical damping force as $f_d := -d_p(\dot{r} + m_a\dot{u}/m)$, l_0 denoting the rest length of the spring, and J_a denoting the additional rotational inertia that might be associated with the linear actuator. In contrast, we formulate the flight dynamics for the SEASLIP in cartesian coordinates of the COM defined as $y = y_b + (m_a/m)u\sin\theta$ and $z = z_b - (m_a/m)u\cos\theta$, with the configuration vector $q_{f_1} := [y, z, \theta, u]^T$ that also incorporates the leg angle. Equations of motion take the form

$$\boldsymbol{M}_{f_1}\ddot{q}_{f_1} + \boldsymbol{C}_{f_1} + \boldsymbol{G}_{f_1} = \Upsilon_{f_1}$$

with

$$
\begin{aligned}
\boldsymbol{M}_{f_1} &= \begin{bmatrix} m & 0 & 0 & 0 \\ 0 & m & 0 & 0 \\ 0 & 0 & m_b m_a u^2/m & 0 \\ 0 & 0 & 0 & J_a + m_b m_a/m \end{bmatrix} \\
\boldsymbol{C}_{f_1} &= \begin{bmatrix} 0 \\ 0 \\ 2 m_b m_a u \dot{\theta} \dot{u}/m \\ -m_b m_a u \dot{\theta}^2/m \end{bmatrix} \\
\boldsymbol{G}_{f_1} &= [0, mg, 0, 0]^T \\
\Upsilon_{f_1} &= [0, 0, \tau_h, f_a - d_p \dot{u}]^T
\end{aligned}
$$

As usual, transitions from flight to stance coincide with the toe coming into contact with the ground, corresponding to the touchdown condition

$$z - (l_0 + u m_b/m)\cos\theta = 0.$$

As a result of the non-zero leg inertia within the SEASLIP model arising from the actuator mass, the touchdown collision results in discontinuous changes in system velocities. In particular, the radial component of the body velocity remains the same due to the non-impulsive nature of the spring and damping forces, but the angular body velocity after the collision is found as

$$\dot{\theta}^+ = \frac{(m_a m_b/m) u^2 \dot{\theta}^- - m(l_0 + u m_b/m)(\dot{z}\sin\theta + \dot{y}\cos\theta)}{m_b (l_0 + u)^2 + m_a l_0^2}.$$

by following the approach in [37].

On the other hand, transition from stance to flight can be triggered by either the leg reaching its full extension with

$$r - l_0 - u\, m_b/m = 0$$

or the vertical ground reaction force on the toe becoming negative with

$$k_p(r - u m_b/m - l_0) + d_p(\dot{r} + \dot{u} m_a/m) = 0$$

Unlike touchdown, the liftoff transition preserves both the configuration and the velocities in the system.

3.3.2 SESLIP: Serially-Actuated Lossy SLIP with No Actuator Dynamics

For the SEASLIP model, both the actuator and body masses are assumed to be aligned radially with the toe. This suggests a simpler template model with a single point mass $m = m_b + m_a$ and a position controlled actuator in series with the spring. This model, which we call the SESLIP model, is also illustrated in Figure 3.1. In Section 3.4.2, we show that accurate position control of u within SEASLIP realizes this model.

The stance dynamics of SESLIP are easily formulated in radial coordinates $q_{s_2} := [r, \theta]^T$ with

$$\begin{aligned} m\ddot{r} &= mr\dot{\theta}^2 - mg\cos\theta - k_p(r - u - l_0) - d_p\dot{r} \\ r\ddot{\theta} &= g\sin\theta - 2\dot{r}\dot{\theta} \; . \end{aligned} \tag{3.2}$$

In contrast, the simplest form of the flight dynamics are in cartesian coordinates, yielding $q_{f_2} := [y, z]^T$ with

$$\begin{aligned} \ddot{y} &= 0 \\ \ddot{z} &= -g \; . \end{aligned} \tag{3.3}$$

As usual with models with massless legs, the SESLIP model also assumes that the leg can be arbitrarily positioned during flight in preparation for the upcoming touchdown event. Transitions from flight to stance is defined similar to the SEASLIP model with the condition

$$z - (l_0 + u_{\text{td}})\cos\theta_{\text{td}} = 0 \; .$$

Here, both the leg angle θ_{td} and the actuator position u_{td} at touchdown are considered to be per-step control inputs determined during flight. In contrast, the transition from stance to flight is captured by the pair of conditions

$$\begin{aligned} r - (u + l_0) &= 0 \\ k_p(r - u - l_0) + d_p\dot{r} &= 0 \end{aligned}$$

corresponding respectively to the full leg extension and the negative ground reaction force on the toe. Since this model has a massless leg, system velocities remain continuous. Intuitively, this simpler template model corresponds to a lossy SLIP model with explicit control over the spring rest length.

3.3.3 FSLIP: Lossy SLIP with Constant Forcing

The last template in the hierarchy of Figure 3.1, the FSLIP model, consists of a point mass riding on a compliant leg with stiffness k, viscous damping coefficient d and a force f, all acting radially and assumed to be controlled in a piecewise constant fashion during stance. In subsequent sections, we will show that this model is sufficiently general to represent a number of different gait control strategies, while being simple enough to support previously developed accurate analytic approximations to the stance dynamics [88, 101] and associated one-step deadbeat controllers. As such, it provides a simple yet effective interface to high level controllers for running.

Similar to the SESLIP model, generalized coordinates for stance and flight phases are respectively defined as $q_{s_3} := [r, \theta]^T$ and $q_{f_3} := [z, y]^T$. Flight dynamics are identical to those of the SESLIP in (3.3) On the other hand, stance dynamics are given by

$$\begin{aligned} m\ddot{r} &= mr\dot{\theta}^2 - mg\cos\theta - k(r - r_{\mathrm{td}}) - d\dot{r} + f \\ r\ddot{\theta} &= g\sin\theta - 2\dot{r}\dot{\theta} \ , \end{aligned} \tag{3.4}$$

where k, d, and f, are the piecewise constant stiffness, damping coefficient and constant forcing terms and $r_{\mathrm{td}} := l_0 + u_{\mathrm{td}}$ is an updated spring rest length to capture nonzero actuator position prior to touchdown. The transition from flight to stance for this model is captured by the condition

$$z - r_{\mathrm{td}}\cos\theta_{\mathrm{td}} = 0 \ ,$$

with both r_{td} and θ_{td} considered as once-per-step control inputs. The transition from stance to flight is captured by

$$\begin{aligned} r - r_{\mathrm{td}} &= 0 \\ k(r - r_{\mathrm{td}}) + d\dot{r} - f &= 0 \ . \end{aligned}$$

3.4 Hierarchical Realization of Template Models

As explained in Section 3.2, our overall control strategy relies on hierarchical embedding of each template in Figure 3.1 into its corresponding anchor towards the left.

The following sections describe in detail anchoring controllers that realize required template dynamics as accurately as possible.

3.4.1 Embedding FSLIP into SESLIP

Dynamics of FSLIP can be realized on SESLIP by appropriately choosing the series elastic actuator position u. During flight, the required touchdown length r_{td} for FSLIP can be realized with

$$u(t) = r_{\mathrm{td}} - l_0$$

In contrast, during stance, the actuator position must be chosen to modulate the radial acceleration of (3.2) to exactly match the radial acceleration required by the FSLIP model as given by (3.4) This can be accomplished with

$$u(t) = u_{\mathrm{td}} + \frac{k_p - k}{k_p}(r(t) - r_{\mathrm{td}}) + \frac{d_p - d}{k_p}\dot{r}(t) + \frac{f}{k_p} \; . \tag{3.5}$$

Since both models have massless legs, their angular dynamics are the same. Thus, matching radial accelerations ensures an exact embedding of FSLIP into SESLIP.

3.4.2 Embedding SESLIP into SEASLIP

Unlike the close match between the template and the anchor models in Section 3.4.1, there are structural differences between the SESLIP and SEASLIP models, including an extra degree of freedom to capture the actuator dynamics in the latter. Fortunately, the COM dynamics of both systems during flight are identical since the only external force acting on the system is the gravitational acceleration. No active embedding is hence necessary and the touchdown leg length and angle for the SEASLIP model can be controlled through the inputs f_a and τ_h, respectively, using any suitable control strategy without affecting COM dynamics.

During stance, however, the COM dynamics become coupled to the dynamics of the actuator. In the sequel, we use the concept of zero dynamics to formalize the formulation of our embedding controller [52, 81]. To begin, the system (3.1) can be written in state-space form as

$$\dot{x}_{s1} = \frac{\mathrm{d}}{\mathrm{d}t}\begin{bmatrix} q_{s1} \\ \dot{q}_{s1} \end{bmatrix} = a(x_{s1}) + b_1(x_{s1})f_a + b_2(x_{s1})\tau_h. \tag{3.6}$$

Considering the position error for the series-elatic actuator as the output function $y_1 := u - u_{\text{des}}$, with $u_{\text{des}} := (m/m_b)u$ to bring together COM positions of the SESLIP and SEASLIP models, the second-order input-output dynamics take the form

$$\ddot{y}_1 = \mathcal{L}_{\mathrm{a}}^2 y_1(x_{s1}) + \mathcal{L}_{b_1}\mathcal{L}_a y_1(x_{s1})f_a + \mathcal{L}_{b_2}\mathcal{L}_a y_1(x_{s1})\tau_h$$

where we have

$$\begin{aligned}
\mathcal{L}_a^2 y_1(x_{s1}) &= \frac{k_p m_b(r - \frac{m_b}{m}u - l_0) - d_p m_a(\dot{r} + \frac{m_a}{m}\dot{u}) + m_b m_a u\dot{\theta}^2}{m_a m_b + J_a m} \\
\mathcal{L}_{b_1}\mathcal{L}_a y_1(x_{s1}) &= \frac{m}{m_a m_b + J_a m} \\
\mathcal{L}_{b_2}\mathcal{L}_a y_1(x_{s1}) &= 0\ .
\end{aligned}$$

with $\mathcal{L}_X(Y)$ denoting the Lie Derivative of vector field Y with respect to vector field X [52]. The following feedback law for the radial control action,

$$f_a = \frac{\mu^\star(y_1, \dot{y}_1) - \mathcal{L}_a^2 y_1(x_{s1}) - \mathcal{L}_{b_2}\mathcal{L}_a y_1(x_{s1})\tau_h}{(\mathcal{L}_{b_1}\mathcal{L}_a y_1(x_{s1}))},$$

where $\mu^\star(y_1, \dot{y}_1)$ is a suitable stabilizing controller, renders the set $\mathcal{Z} := \{x_{s1} : y_1(x_{s1}) = 0 \wedge \mathcal{L}_a y_1(x_{s1}) = 0\}$ attractive and invariant. Using the simple, yet effective PID control strategy

$$\mu^\star(y_1, \dot{y}_1) = -K_p y - K_i \int_0^t y(\lambda)\mathrm{d}\lambda - K_d\dot{y},$$

results in the closed-loop transverse dynamics

$$\ddot{y}_1 = -K_p y - K_i \int_0^t y(\lambda)\mathrm{d}\lambda - K_d\dot{y}$$

which can be exponentially stabilized by a proper choice of K_p, K_i, and K_d. Furthermore, if the PID gains are sufficiently high, system trajectories will quickly converge onto the zero dynamics manifold $\mathcal{Z}$ and follow its restricted dynamics. Note, also, that the new gait controllers we propose for FSLIP in Section 3.6.2 ensure smooth trajectories for the desired actuator position $\hat{u}_{\text{des}}(t)$, further improving embedding performance.

The final component in the embedding of SESLIP into SEASLIP is a feedback law for the hip torque control action τ_h that ensures that the restriction dynamics of SEASLIP on $\mathcal{Z}$ is diffeomorphic to SESLIP. Since $\mathcal{L}_{b_1}\mathcal{L}_a y_1(x_{s1}) = 0$, control actions are decoupled in radial and angular directions. This allows separate formulation of control actions for tangential and radial actuator inputs. Defining $y_2 := \theta$, we have

$$\ddot{y}_2 = \mathcal{L}_{\mathrm{a}}^2 y_2(x_{s1}) + \mathcal{L}_{b_1}\mathcal{L}_a y_2(x_{s1}) f_a + \mathcal{L}_{b_2}\mathcal{L}_a y_2(x_{s1})\tau_h$$

where

$$\begin{aligned}
\mathcal{L}_a^2 y_2(x_{s1}) &= \frac{m\left(mgr\sin\theta - 2mr\dot{r}\dot{\theta} - 2m_a(m_b/m)u\dot{u}\dot{\theta}\right)}{m^2r^2 + m_b m_a u^2} \\
\mathcal{L}_{b_1}\mathcal{L}_a y_2(x_{s1}) &= 0 \\
\mathcal{L}_{b_2}\mathcal{L}_a y_2(x_{s1}) &= \frac{m\tau_h}{m^2r^2 + m_b m_a u^2}
\end{aligned}$$

At this point, the angular component of the SESLIP dynamics can be enforced on the system by using the hip torque

$$\tau_h = \frac{m_a m_b u(gu\sin\theta + 2(r\dot{u} - u\dot{r})\dot{\theta})}{mr}. \tag{3.7}$$

Having formulated both control actions, the restriction dynamics are found by substituting $u = u_{\mathrm{des}}$ and (3.7) in (3.6) as

$$\begin{aligned}
\ddot{r} &= r\dot{\theta}^2 - g\cos\theta - \frac{k_p}{m}(r - u_{\mathrm{des}} - l_0) - \frac{d_p}{m}\dot{r} + n(\dot{u}_{\mathrm{des}}) \\
r\ddot{\theta} &= g\sin\theta - 2\dot{r}\dot{\theta}
\end{aligned}$$

with $n(\dot{u}_{\mathrm{des}}) := -d_p m_a \dot{u}_{\mathrm{des}}/(m\ m_b)$. Unfortunately, due to the extra term $n(\dot{u}_{\mathrm{des}})$, embedding of SESLIP into SEASLIP can only be approximate [66]. Nevertheless, as we will observe in our simulation results, the effects of $n(\dot{u}_{\mathrm{des}})$ are expected to remain small since, in general, platform designs seek to minimize frictional losses by reducing d_p in comparison with spring forces, while keeping the actuator linear mass m_a small relative to the body mass m_b. For example, recent leg designs based on parallel mechanisms explicitly minimize m_a/m_b to be close to 0 by relying on rotary actuators located around the center-of-mass [46, 55].

Finally, even though exact embedding of angular dynamics is possible with (3.7), we have chosen to evaluate the performance of our embedding controller with $\tau_h = 0$, including associated deviations from the ideal embedding in our characterization of controller performance. For physical platforms, the hip torque is generally also used for stabilizing body attitude, which will inevitably effect the angular dynamics. Consequently, exact embedding of angular leg dynamics is generally not achievable in practice. Nevertheless, our results with $\tau_h = 0$ in Section 3.7.2 and the illustrative example in Figure 3.5 confirm that inaccuracies in the embedding of SESLIP into SEASLIP remain small when the the gait level controller ensures continuity of $\hat{u}_{\text{des}}(t)$ for SESLIP.

3.5 Analytic Solutions for the FSLIP Template

The cascaded embedding controllers of Section 3.4 allow us to formulate gait controllers purely within the FSLIP model, which is considerably simpler and admits approximate yet accurate analytic solutions to its dynamics, reducing computational complexity with respect to numerical simulations [79]. In this section, we present generalized analytic solutions assuming that the parameters k, d and f are modulated in a piecewise constant fashion, propose a number of improvements on the basic method of [88] to increase accuracy and support deadbeat control strategies for different subsets of available control inputs, which we describe in Section 3.6.

3.5.1 Generalization of Existing Analytic Approximations

In parallel with previous work, we seek to find the apex return map for a single stride of the FSLIP model. Defining apex coordinates as $\mathbf{X} := [y, z, \dot{y}]^T$ at the highest point during flight with $\dot{z} = 0$, the return map from the i^{th} apex to the next takes the form

$$\mathbf{X}[i+1] = \mathcal{R}(\mathbf{X}[i], \theta_{\text{td}}[i], r_{\text{td}}[i], \mathbf{p}[i])$$

where $\theta_{\text{td}}[i]$ and $r_{\text{td}}[i]$ are the leg angle and length at touchdown and $\mathbf{p}[i]$ denotes a discrete parameterization of remaining control inputs $k(t)$, $d(t)$ and $f(t)$ within the i^{th} stride. In particular, our generalized approximate analytic solutions described below support piecewise constant modulation of the FSLIP leg parameters $k(t)$, $d(t)$ and $f(t)$ during stance.

As usual, the apex return map can be computed as the composition of individual maps for flight and stance. The flight maps capture ballistic dynamics and admit exact analytic solutions [88]. Stance dynamics, on the other hand, cannot be solved analytically [43], but fortunately allow sufficiently accurate approximations. In particular, we adopt the structure of the approximation proposed in [88], which proceeds in two stages: i) Generating a preliminary solution assuming small angular displacement and spring deflection to decouple and linearize the dynamics, and ii) Incorporating corrections to the predictions of the first stage by improving on initial assumptions to reach the final solution. In this chapter, we generalize the approximations introduced in [88] to arbitrary initial and final conditions within stance, and introduce several improvements in both stages to substantially improve predictive accuracy.

To formalize, suppose the FSLIP model begins with a particular initial state $[q_{s_3}(0), \dot{q}_{s_3}(0)]$ within stance at $t = 0$. Our generalized approximations seek to compute $[q_{s_3}(t_f), \dot{q}_{s_3}(t_f)]$ for any subsequent point in the stance phase with $0 < t_f \leq t_{\mathrm{lo}}$, where t_{lo} denotes the time of liftoff and the leg parameters k, d and f are assumed to remain constant in interval $[0, t_f]$. To this end, we begin by assuming that the angular momentum stays constant at $\hat{L}$ as in [88], but propose the following three improvements:

1. We linearize radial dynamics around an average length
$$\hat{r} := \frac{1}{t_f}\int_0^{t_f} r(t)\mathrm{d}t \tag{3.8}$$
instead of $r(0)$,

2. We linearize angular dynamics around an average angle
$$\hat{\theta} := \frac{1}{t_f}\int_0^{t_f} \theta(t)\mathrm{d}t \tag{3.9}$$
instead of $\theta = 0$,

3. We use a corrected gravitational acceleration
$$\hat{g} := \frac{1}{t_f}\int_0^{t_f} g\cos\theta(t)\mathrm{d}t. \tag{3.10}$$
in the radial direction to account for non-symmetric strides.

Redefining stiffness and spring rest length parameters with

$$\begin{aligned}
\kappa &:= k + 3\hat{L}^2/(m\hat{r}^4) \\
\gamma &:= r_{\mathrm{td}} - \left(m\hat{g} - f - \hat{L}^2(4\hat{r} - 3r_{\mathrm{td}})/(m\hat{r}^4)\right)/\kappa
\end{aligned}$$

and shifted radial coordinates with $r_s := r - \gamma$, the equations of motion can be approximated as

$$
\begin{aligned}
m\ddot{r}_s &= -\kappa r_s - d\dot{r}_s && (3.11)\\
m\hat{r}^3\dot{\theta} &= \hat{L}(3\hat{r} - 2(r_s + \gamma))\ . && (3.12)
\end{aligned}
$$

following derivations similar to those in [88]. Assuming underdamped dynamics, this set of second order linear ODEs gives approximate trajectories at a given time t_f as

$$
\begin{aligned}
r_s(t_f) &= e^{-\frac{d}{2m}t_f}\left[r_s(0)\cos T_f + \frac{2m\dot{r}_s(0) + dr_s(0)}{\sqrt{4\kappa m - d^2}}\sin T_f\right] && (3.13)\\
\theta(t_f) &= \theta(0) + \frac{\hat{L}}{m\hat{r}^3}\left[t_f(3\hat{r} - 2\gamma) - 2\int_0^{t_f} r_s(t)\mathrm{d}t\right] && (3.14)
\end{aligned}
$$

where we have $T_f := t_f\sqrt{4\kappa m - d^2}/(2m)$ and the integral term in (3.14) is computed by integrating both sides of (3.11) as

$$
\int_0^{t_f} r_s(t)\mathrm{d}t = -\frac{m}{\kappa}\left(\dot{r}_s(t_f) - \dot{r}_s(0)\right) - \frac{d}{\kappa}\left(r_s(t_f) - r_s(0)\right)\ . \qquad (3.15)
$$

As noted above, our approximations to the stance trajectories of the FSLIP model consist of two stages. Since the radial and angular trajectories are initially unknown, the first stage generates initial estimates $r^{(0)}(t)$ and $\theta^{(0)}(t)$ for system trajectories by choosing $\hat{L}^{(0)} = L(0)$, $\hat{g}^{(0)} = g$ and $\hat{r}^{(0)} = r(0)$ within (3.13) and (3.14). Once these estimates are obtained, the second stage uses improved estimates for $\hat{L}$, $\hat{g}$ and $\hat{r}$ to obtain new approximations $r^{(1)}(t)$ and $\theta^{(1)}(t)$.

Regardless of the nature of the corrections in this second step, the radial velocity can be computed through direct differentiation of (3.13) and the angular velocity based on the conservation of angular momentum and a model of damping losses as proposed in [88].

3.5.2 Convention

In the following subsections, we will present detailed derivations of average angular momentum and gravity during stance for the FSLIP model. Before doing so, however, we will find it useful to introduce a number of common definitions and integrals. First, we define a simplified notation for single, double, and triple integrals of any function $g(t)$ as

$$
\begin{aligned}
I_g(t) &:= \int_0^t g(x)\mathrm{d}x \\
D_g(t) &:= \int_0^t \left(\int_0^y g(x)\mathrm{d}x\right)\mathrm{d}y \\
T_g(t) &:= \int_0^t \left(\int_0^z \left(\int_0^y g(x)\mathrm{d}x\right)\mathrm{d}y\right)\mathrm{d}z.
\end{aligned}
$$

Closed form solutions to some common integrals that we will use throughout our derivations are given as

$$
\begin{aligned}
I_r(t) &= \gamma t - \frac{m}{\kappa}\left(\dot{r}(t) - \dot{r}(0)\right) - \frac{d}{\kappa}\left(r(t) - r(0)\right) \qquad (3.16)\\
D_r(t) &= \frac{\gamma}{2}t^2 - \frac{m}{\kappa}\left(r(t) - r(0) - t\dot{r}(0)\right) - \frac{d}{\kappa}I_r(t) \\
T_r(t) &= \frac{\gamma}{6}t^3 - \frac{m}{\kappa}\left(I_r(t) - tr(0) - t^2\frac{\dot{r}(0)}{2}\right) - \frac{d}{\kappa}D_r(t) \\
I_\theta(t) &= t\,\theta(0) + \frac{\hat{L}}{m\hat{r}^3}\left(\frac{3\hat{r}}{2}t^2 - 2D_r(t)\right) \\
I_{tr}(t) &= tI_r(t) - D_r(t) \\
I_{t\int r}(t) &= tD_r(t) - T_r(t) \\
D_{tr}(t) &= I_{t\int r}(t) - T_r(t)
\end{aligned}
$$

and can be derived via straightforward algebraic manipulations and integration by parts using our analytic approximations for $r(t)$ and $\theta(t)$.

3.5.3 Estimation of Average Angular Momentum

In [88], the angular momentum was updated in the second stage with

$$
\hat{L}^{(1)} = \hat{L}^{(0)} + \frac{mgt_f}{4}\left(r(0)\sin\theta(0) + r(t_f)\sin\theta(t_f)\right) .
$$

This correction, however, assumes a linear gravitational torque between the initial and final states during stance and is not accurate since the leg length trajectory also effects angular momentum through

$$
L(t) = L(0) + mg\int_0^t r(\tau)\sin\theta(\tau)\mathrm{d}\tau. \qquad (3.17)
$$

We propose a more accurate second stage for the constant angular momentum based on its average value with

$$\hat{L}^{(1)} = L_{\text{avg}} = \frac{1}{t_f} \int_0^{t_f} L(t)\mathrm{d}t \ , \tag{3.18}$$

based on a small angle approximate of (3.17) in the form

$$L(t) = L(0) + mg \left[\int_0^t r(\tau) \left(\sin\hat{\theta} + (\theta(\tau) - \hat{\theta}) \cos\hat{\theta} \right) \mathrm{d}\tau \right] . \tag{3.19}$$

A detailed derivation for our analytic approximations to L_{avg} is given below.

We begin the derivation by manipulating (3.19) as

$$L(t_f) = L(0) + mg \left[\left(\sin\hat{\theta} - \hat{\theta}\cos\hat{\theta} \right) I_r(t_f) + (\cos\hat{\theta}) I_{r\theta}(t_f) \right] ,$$

where $I_{r\theta}(t_f)$ can be computed by multiplying with r and then integrating as

$$I_{r\theta}(t_f) = \theta(0) I_r(t_f) + \frac{\hat{L}}{m\hat{r}^3} \left(3\hat{r} I_{tr}(t_f) - 2 I_{r\int r}(t_f) \right) \tag{3.20}$$

with

$$I_{r\int r}(t_f) = I_r^2(t_f)/2. \tag{3.21}$$

In order to evaluate average angular momentum L_{avg} in (3.18), we first need to compute

$$I_L(t_f) = t_f L(0) + mg \left[\left(\sin\hat{\theta} - \hat{\theta}\cos\hat{\theta} \right) D_r(t_f) + (\cos\hat{\theta}) D_{r\theta}(t_f) \right]$$

where $D_{r\theta}(t_f)$ can be found by direct integration of (3.20) as

$$D_{r\theta}(t_f) = \theta(0) D_r(t_f) + \frac{\hat{L}}{m\hat{r}^3} \left(3\hat{r} D_{tr}(t_f) - 2 D_{r\int r}(t_f) \right) .$$

After multiplying both sides of (3.16) with $I_r(t)/2$, we integrate the resulting expression and obtain

$$D_{r\int r}(t_f) = \frac{\gamma}{2} I_{t\int r}(t_f) - \frac{m}{2\kappa} (I_{rd\int r}(t_f) - rd(0) D_r(t_f)) - \frac{d}{2\kappa} (I_r^2(t_f)/2 - r(0) D_r(t)).$$

with $I_{rd\int r}(t_f) = r(t_f) I_r(t_f) - I_{r^2}(t_f)$. The only challenge is now to find $I_{r^2}(t_f)$. To this end, we consider conservation of energy in the radial direction for the computation of $I_{r^2}(t_f)$. Rewriting (3.11) in the unshifted coordinate system (r, rd) as

$$m\ddot{r} = -\kappa(r - r_{\text{td}}) - d\dot{r} + \kappa\bar{f} \tag{3.22}$$

with $\bar{f} := \gamma - r_{\text{td}}$, radial energy can be expressed as

$$E(t_f) = \frac{1}{2}\kappa r^2 + \frac{1}{2} mrd^2 - \kappa\gamma r + \frac{1}{2}\kappa r_{\text{td}}^2. \tag{3.23}$$

On the other hand, multiplying both sides of (3.22) with r and then integrating leads to a new form

$$I_{r^2}(t_f) = \gamma I_r(t_f) - \frac{d}{2\kappa}(r^2(t_f) - r^2(0)) - \frac{m}{\kappa} I_{rrdd}(t_f). \tag{3.24}$$

The second term $I_{rrdd}(t_f)$ on the right hand side can be computed via integration by parts as

$$I_{rrdd}(t_f) = r(t)rd(t_f) - r(0)rd(0) - I_{rd^2}(t_f). \tag{3.25}$$

Substituting (3.25 into (3.24) we get

$$I_{r^2}(t_f) - \frac{m}{\kappa} I_{rd^2}(t_f) = \gamma I_r(t_f) - \frac{d}{2\kappa}(r^2(t_f) - r^2(0)) - \frac{m}{\kappa}\left(r(t_f)rd(t_f) - r(0)rd(0)\right). \tag{3.26}$$

Consider first, lossless FSLIP with $d = 0$. Energy is conserved in this case reducing (3.23) to $E(t_f) = E(0)$. Integrating both sides of (3.23) takes the form

$$I_{r^2}(t_f) + \frac{m}{\kappa} I_{rd^2}(t_f) = (2E(0)/\kappa - r_{\text{td}}^2)t_f + 2\gamma I_r(t_f). \tag{3.27}$$

Adding (3.27 and (3.26) side by side leads to solution of $I_{r^2}(t_f)$ for $d = 0$ as

$$I_{r^2}(t_f) = \frac{3\gamma\kappa I_r(t_f) + (2E(0) - \kappa r_{\text{td}})t_f - m\left(r(t_f)rd(t_f) - r(0)rd(0)\right)}{2\kappa}.$$

For the remaining cases with $d \neq 0$, we compute $I_{r^2}(t_f)$ based on damping losses. Damping losses are defined as

$$\Delta E(t_f) := dI_{rd^2}(t_f) = E(0) - E(t_f).$$

Thus, plugging $I_{r^2}(t_f)$ into (3.26 gives the solution to $I_{r^2})t_f)$ for $d \neq 0$ as

$$I_{r^2}(t_f) = \gamma I_r(t_f) + \frac{m}{d\kappa}\Delta E(t_f) - \frac{d}{2\kappa}(r^2(t_f) - r^2(0)) - \frac{m}{\kappa}\left(r(t_f)rd(t_f) - r(0)rd(0)\right).$$

3.5.4 Estimation of Average Leg Length and Angle

An additional improvement we propose to increase the accuracy of the approximate analytical map proposed in [88] was to linearize nonlinear components in the radial and angular dynamics during stance around an average leg length and angle as defined in (3.8) and (3.9) rather than the spring rest length and vertical leg orientation. It turns out that analytic approximations for these quantities can easily be obtained by substituting (3.15) into (3.8) and integrating (3.14) to yield

$$\hat{r}^{(1)} = \frac{r_0\kappa - m\gamma - m\left(\dot{r}(t_f) - \dot{r}(0)\right) - d\left(r(t_f) - r(0)\right)}{\kappa t_f}$$

$$\hat{\theta}^{(1)} = \theta(0) + \frac{\hat{L}\left(t_f^2(3\hat{r} - 2\gamma)/2 - 2\int\limits_0^{t_f}\int\limits_0^{t} r_s(\tau)\mathrm{d}\tau\mathrm{d}t\right)}{m\hat{r}^3 t_f}$$

where we have

$$\int_0^{t_f}\int_0^{t} r_s(\tau)\mathrm{d}\tau\mathrm{d}t = -\frac{m}{\kappa}\left(r_s(t_f) - r_s(0)\right) - \frac{d}{\kappa}\int_0^{t_f} r_s(t)\mathrm{d}t + t_f\frac{m\dot{r}(0) + dr(0)}{k}\ .$$

3.5.5 Estimation of Average Gravity in the Radial Direction

In [88], angular dynamics were linearized around the vertical, approximating the effects of gravity in the radial direction with $\hat{g} = g$. However, any deviation from purely vertical motion violates this assumption and effects the accuracy of the approximations. To address this issue, we use a second order Taylor-series expansion of the average effect of gravity in the radial dynamics defined in (3.10) around $\hat{\theta}$ as

$$\hat{g}^{(1)} = \frac{g}{t_f}\int_0^{t_f}\left(1 - \frac{(\theta - \hat{\theta}(t))^2}{2}\right)\cos\hat{\theta} - (\theta - \hat{\theta})\sin\hat{\theta}\mathrm{d}t. \qquad (3.28)$$

Detailed derivations for an analytic solution to this definition are presented below.

Radially acting gravity in (3.28) can be written as

$$\hat{g}^{(1)} = \frac{g}{t_f}\left[-\frac{\cos\hat{\theta}}{2}I_{\theta^2}(t_f) + \left(\hat{\theta}\cos\hat{\theta} - \sin\hat{\theta}\right)I_\theta(t_f) + \left(\hat{\theta}\sin\hat{\theta} + (1 - \hat{\theta}^2/2)\cos\hat{\theta}\right)t_f\right].$$

where $I_{\theta^2}(t_f)$ is the only unknown quantity within this equation. Squaring both sides of (3.14) we obtain

$$\theta^2(t) = \theta^2(0) + \frac{2\hat{L}\,\theta(0)}{m\hat{r}^3}\left[3\hat{r}t - 2I_r(t)\right] + \frac{\hat{L}^2}{m^2\hat{r}^6}\left[9\hat{r}^2t^2 - 12\hat{r}tI_r(t) + 4I_r^2(t)\right].$$

Integrating both sides, $I_{\theta^2}(t_f)$ takes the form

$$I_{\theta^2}(t_f) = t_f\,\theta^2(0) + \frac{\hat{L}\,\theta(0)}{m\hat{r}^3}\left[3t_f^2 - 4D_r(t_f)\right] + \frac{\hat{L}^2}{m^2\hat{r}^6}\left[3\hat{r}^2t_f^3 - 12\hat{r}I_{t\int r}(t_f) + 4I_{(\int r)^2}(t_f)\right].$$

with $I_{(\int r)^2}(t_f) = 2D_{r\int r}(t_f)$ by (3.21)

3.5.6 Correction of Final Energy and Angular Momentum

The accuracy of the analytic approximations we described in preceding sections is lower for velocity components of the state than positional coordinates. This issue was addressed in [88] through a correction in the angular velocity based on a predicted energy level at liftoff. We extend this idea and incorporate a joint correction in both radial and angular velocities at the final point of the predicted trajectory using both the predicted energy, as well as the corrected angular momentum in(3.18). In particular, the final angular velocity is corrected as

$$\dot{\theta}(t_f) = \frac{L(t_f)}{mr^2(t_f)}$$

and the final radial velocity $\dot{r}(t_f)$ is corrected using the energy correction method described in [88].

3.5.7 A General Solution for Events During Stance

Different control strategies we consider for the FSLIP template rely on a piecewise constant parameterization of the model parameters $k(t)$, $d(t)$ and $f(t)$ during stance to support the validity of our analytic approximations. In all cases, transitions from one set of parameters to the next will be triggered by state-based "events" (e.g. the bottom instant with $\dot{r} = 0$), based on solutions to linear equations of radial states in the form

$$a_p r_s(t) + a_v \dot{r}_s(t) = a_0 \tag{3.29}$$

where a_p, a_v, a_0 denote constants specific to particular event definitions and $r_s(t)$ and $r_s(t)$ are computed using (3.13). In this section, we provide an analytic solution to compute the time of occurrence for such events.

Consider first, events with $a_0 = 0$. This simplifies the event condition to $A \cos T_f + B \sin T_f = 0$ with

$$\begin{aligned} A &:= r_s(0)a_p + \dot{r}_s(0)a_v \\ B &:= \frac{r_s(0)(a_p d - 2a_v\kappa) + \dot{r}_s(0)(2a_p m - a_v d)}{\sqrt{4\kappa m - d^2}} \end{aligned}$$

whose solutions for $n \in \mathbb{Z}$ are given by

$$t_f = \frac{2m}{\sqrt{4\kappa m - d^2}} \left(\frac{\pi}{2} + n\pi + \arctan\left(\frac{B}{A}\right)\right) \ .$$

For the remaining cases with $a_0 \neq 0$, we propose a two step solution. In the first step, a first order perturbation series is used to approximately solve for the time of the event. A more accurate solution is then computed by evaluating the exponential terms in (3.13) with the initial estimate. Substituting (3.13), (3.29) takes the form

$$A \cos T_f + B \sin T_f = y\, e^{\frac{d}{2m} t_f} \ . \tag{3.30}$$

Choosing d as the small parameter of (3.30), we model the solution as a perturbation series in the form

$$t_f = t_f^0 + d\, t_f^1 + \mathcal{O}d^2.$$

where t_f^i denotes the i[th] order perturbed solution. The resulting first-order asymptotic approximation to (3.30) leads to

$$A_0\, c_0 + B_0\, s_0 \quad = \quad y \tag{3.31}$$

$$t_f^1 \left(A_1^0\, c_0 + B_1^0\, s_0 \right) \quad = \quad A_1^1\, c_0 + B_1^1\, s_0 - t_f^0\, a_0/(2m) \tag{3.32}$$

with

$$\begin{aligned}
c_0 &:= \cos\left(t_f^0 \sqrt{2\kappa}\right) \\
s_0 &:= \sin\left(t_f^0 \sqrt{2\kappa}\right) \\
A_0 &:= r_s(0) a_p + \dot{r}_s(0) a_v \\
B_0 &:= (-r_s(0) a_v \kappa/m + \dot{r}_s(0) a_p)/\sqrt{\kappa/m} \\
A_1^0 &:= r_s(0) a_v \kappa/m - \dot{r}_s(0) a_p \\
B_1^0 &:= (r_s(0) a_p + \dot{r}_s(0) a_v)\sqrt{\kappa/m} \\
A_1^1 &:= 0 \\
B_1^1 &:= (r_s(0) a_p + \dot{r}_s(0) a_v)/(2\sqrt{\kappa m}) \ .
\end{aligned}$$

Solutions to (3.31) and (3.32) are obtained as

$$\begin{aligned}
t_f^0 &= \frac{\arccos(y/\sqrt{(A_0)^2 + (B_0)^2}) + 2n\pi + \arctan\left(B_0/A_0\right)}{\sqrt{2\kappa}} \\
t_f^1 &= \frac{A_1^1\, c_0 + B_1^1\, s_0 - t_f^0 y/(2m)}{A_1^0\, c_0 + B_1^0\, s_0}.
\end{aligned}$$

which leads to the overall perturbation solution $\hat{t}_f = t_f^0 + dt_f^1$. After the exponential term on the right hand side of (3.30) is evaluated at $\hat{t}_f$, the final solution is obtained as

$$t_f \approx \frac{2m}{\sqrt{4\kappa m - d^2}} \left[\arccos(\frac{y e^{\frac{d}{2m}\hat{t}_f}}{\sqrt{A^2+B^2}}) + 2n\pi + \arctan\left(\frac{B}{A}\right) \right].$$

3.5.8 Improvements in Predictive Performance

In order to characterize the benefits of the improvements we proposed in preceding sections, we repeated the systematic simulations described in [88], measuring the prediction performance of the analytic approximations for a single stride. In doing so, we used the same ranges for leg parameters and initial conditions but used wider range for the touchdown angle to increase coverage in the apex states, with $\theta_{\text{td}} \in \theta_{\text{td}}^n + [-0.43, 0.61]$ rad, where θ_{td}^n denotes the "neutral" touchdown angle that results in a symmetric FSLIP trajectory for the lossless model with $d = 0$ and $f = 0$. Using the the same apex position and liftoff velocity error metrics, respectively defined as

$$\begin{aligned} \text{PE}_{\text{ap}} &:= 100 \, \|[y_a, z_a] - [\hat{y}_a, \hat{z}_a]\|_2 \, / \, \|[y_a, z_a]\|_2 \\ \text{PE}_{\text{lov}} &:= 100 \left\| [\dot{r}_{\text{lo}}, \dot{\theta}_{\text{lo}}] - [\hat{\dot{r}}_{\text{lo}}, \hat{\dot{\theta}}_{\text{lo}}] \right\|_2 \Big/ \left\| [\dot{r}_{\text{lo}}, \dot{\theta}_{\text{lo}}] \right\|_2 \end{aligned}$$

Table 3.1 summarizes the performance of the approximate analytical stance solution with and without our improvements.

Table 3.1: Single stride average percentage prediction errors for the FSLIP template with and without our improvements.

	PE_{ap}		PE_{lov}	
	$\mu \pm \sigma$	max	$\mu \pm \sigma$	max
original	1.74 ± 3.12	54.90	2.01 ± 3.34	44.52
proposed	0.19 ± 0.38	4.45	0.09 ± 0.10	0.97

These results show that our proposed improvements result in a substantial increase in the predictive accuracy of the approximate analytic solutions to the FSLIP dynamics.

3.6 Gait Control of the FSLIP Template

The gait control problem for running behaviors is often formulated as the stride-to-stride regulation of apex states for planar spring-mass models. When sufficiently accurate return maps are available for a single stride, a deadbeat strategy becomes feasible, computing control inputs through direct inversion of the return map with

$$(\theta_{\mathrm{td}}[i], r_{\mathrm{td}}[i], \mathbf{p}[i]) = \mathcal{R}^{-1}(\mathbf{X}^*, \mathbf{X}[i]) \tag{3.33}$$

Such a strategy, implemented through either a numerical realization of $\mathcal{R}$ or an analytic approximation $\widehat{\mathcal{R}}$, can achieve a particular desired apex state $\mathbf{X}^*$ in a single stride.

In this chapter, our focus will be on controlling only two of the apex states, the forward velocity $\dot{y}_a$ and the body height z_a. Consequently, we choose to keep the leg length at touchdown fixed with $r_{\mathrm{td}}[i] = l_0 + u_0$ for all strides, relying only on the touchdown angle θ_{td} and radial actuation parameters $\mathbf{p}$ to achieve the desired outcome. In particular, we formulate the deadbeat controller as an optimization problem

$$(\theta_{\mathrm{td}}[i], \mathbf{p}[i]) = \underset{\theta_{\mathrm{td}},\mathbf{p}}{\operatorname{argmin}} \left\| \mathbf{X}^*_{[\dot{y},z]} - \widehat{\mathcal{R}}_{[\dot{y},z]}(\mathbf{X}[i], \theta_{\mathrm{td}}, r_{\mathrm{td}}, \mathbf{p}) \right\|^2$$

restricted to the forward velocity and body height components of the return map, using our analytic approximations to the apex return map, $\widehat{\mathcal{R}}$. In the following sections, we will use this generalized formulation for deadbeat controllers to describe a number of different strategies corresponding to specific parameterizations $\mathbf{p}$ of radial actuation for controlling system energy within the FSLIP model.

3.6.1 Traditional Technique : Variable Stiffness Controller

A commonly used mechanism for controlling energy in spring-mass models that also preserves the validity of analytic solutions to their dynamics is to force a step change in spring stiffness at maximum leg compression [92]. This approach has also been used in the control of walking and gait transitions for a bipedal SLIP model [100]. For the FSLIP model, this corresponds to keeping $d(t) = d_p$ and $f(t) = 0$ constant throughout stance, while enforcing

$$k(t) = \begin{cases} k_p & \dot{r} < 0 \text{ (compression)} \\ k_{vs} & \dot{r} \geq 0 \text{ (decompression)} \end{cases}$$

with only the decompression stiffness explicitly regulated. This corresponds to the parametrization $\mathbf{p}_{vs} := [k_{vs}]$ for a single stride. As we will show in later sections, however, this is a commonly used but unrealistic approach that requires infinite actuator power at bottom to realize the discontinuous change in leg stiffness.

3.6.2 Proposed Technique : Variable Damping Controller

3.6.2.1 Constant tunable damping

The variable stiffness strategy attempts instantaneous injection/removal of required energy difference within the stride, corresponding to a step change in the series-elastic actuator position. Physical realizations of this idea hence not only require large actuator power, but are also bound to only approximately be able to achieve the desired outcome.

A much more effective method would be to spread energy injection/removal throughout the entire stance phase, thereby decreasing instantaneous actuator power requirements. To this end, we propose to use the virtually tunable damping coefficient of the FSLIP model, realized through the embedding controllers described in Section 3.4. In particular, we keep $k(t) = k_p$ and $f(t) = 0$, while enforcing

$$d(t) = d_{cd} \ ,$$

all of which remain constant throughout the entire stance phase. This corresponds to the parametrization $\mathbf{p}_{cd} := [d_{cd}]$ for a single stride. As evident from (3.5), this is expected to yield a smooth trajectory for the series-elastic actuator, proportional to the radial leg velocity during stance. The decrease in the required actuator velocity directly translates into reduced power requirements and increased accuracy in the embedding of the template dynamics. Note that energy injection is also possible in this approach with $d_{cd} < 0$.

Even though this basic idea is promising, anchoring an FSLIP with $d_{cd} \neq d_p$ into SESLIP with (3.5) results in a discontinuity in the desired actuator position $u(t)$ at touchdown, wherein the leg spring which was previously at rest needs to immediately generate force following the transition to stance. We consider three methods to address this issue to ensure practical applicability of using tunable damping for platforms with series-elastic actuation (e.g., SEASLIP) by analyzing ideal actuator motion profiles when anchored to SESLIP.

3.6.2.2 Decompression-only tunable damping

In order to address the actuator position discontinuity mentioned above, we first observe that the controller described in Section 3.6.2.1 results in the SESLIP actuator position

$$u(t) = u_{\mathrm{td}} + \dot{r}(d_p - d_{cd})/k_p. \tag{3.34}$$

following the application of the embedding controller in Section 3.4.1. Fortunately, the stance phase within every stride experiences a "bottom" point with $\dot{r} = 0$. This suggests that the continuity of the commanded actuator position can be obtained if the regulation of the radial damping coefficient was delayed until the bottom point. In particular, regulating the damping coefficient as

$$d(t) = \begin{cases} d_p & \dot{r} < 0 \text{ (compression)} \\ d_{dd} & \dot{r} \geq 0 \text{ (decompression)} \end{cases}$$

ensures that the actuator maintains its initial position $u(t) = u_{\mathrm{td}}$ until bottom, after which it starts following (3.34) to realize the desired damping coefficient. The discrete parameterization corresponding to this strategy can be defined as $\mathbf{p}_{dd} := [d_{dd}]$. Note, also, that the approximate solutions described in Section 3.5 can be applied in two consecutive pieces to obtain an analytic apex return map for the FSLIP model with this controller.

3.6.2.3 Shifted tunable damping

Another alternative to using an explicit initialization phase as proposed in the previous section is to exploit the availability of the forcing term $f(t)$ in the FSLIP template to compensate for the discontinuous actuator position command at touchdown. In particular, if we choose a fixed damping coefficient for the entire stance phase with $d(t) = d_{sd}$, but enforce

$$f(t) = (d_{sd} - d_p)\dot{r}_{\mathrm{td}}$$

we can ensure that $u(0) = u_{\mathrm{td}}$, effectively eliminating any discontinuities in the actuator position command at touchdown. This strategy, which we call the *shifted tunable damping*, requires only a single parameter with $\mathbf{p}_{sd} = [d_{sd}]$. Moreover, since the actuator position

$$u(t) = u_{\mathrm{td}} + (d_p - d_{sd})/k_p\dot{r}(t) + (d_{sd} - d_p)/k_p\dot{r}_{\mathrm{td}}$$

resulting from this strategy is C^∞, we expect this strategy to have the best energy and power efficiency compared to other alternatives introduced above.

Figure 3.2 illustrates example single-stride simulations for the SESLIP model with all of the control strategies described above, showing resulting system trajectories and actuator positions as a function of time.

3.7 Controller Performance

In the following subsections, we present a systematic comparison of gait control methods described in Section 3.6. In particular, controllers are compared in terms of their energetic characteristics and single stride control accuracies through simulations obtained for a human-sized robotic platform with $m = 60kg$ and $l_0 = 1m$, also compatible with recent bipeds such as ATRIAS. The remaining platform parameters were chosen to span representative non-dimensional ranges with $\kappa_p := k_p r_{\mathrm{td}}/(mg) \in [8, 60]$ as the relative spring stiffness, $\xi_p := d_p/(2\sqrt{k_p m}) \in [0.02, 0.08]$ as the damping ratio and $\bar{z}_0 := z_0/r_{\mathrm{td}} \in [1.05, 1.35]$ and $\bar{\dot{y}}_0 := \dot{y}_0/\sqrt{gl_0} \in [0, 1]$ as initial apex height and velocity states, respectively.

3.7.1 Effectiveness of Energy Input

An important limitation of series-elastic actuation for compliant legged platforms comes from limits on the actuator displacement, constraining the amount of energy

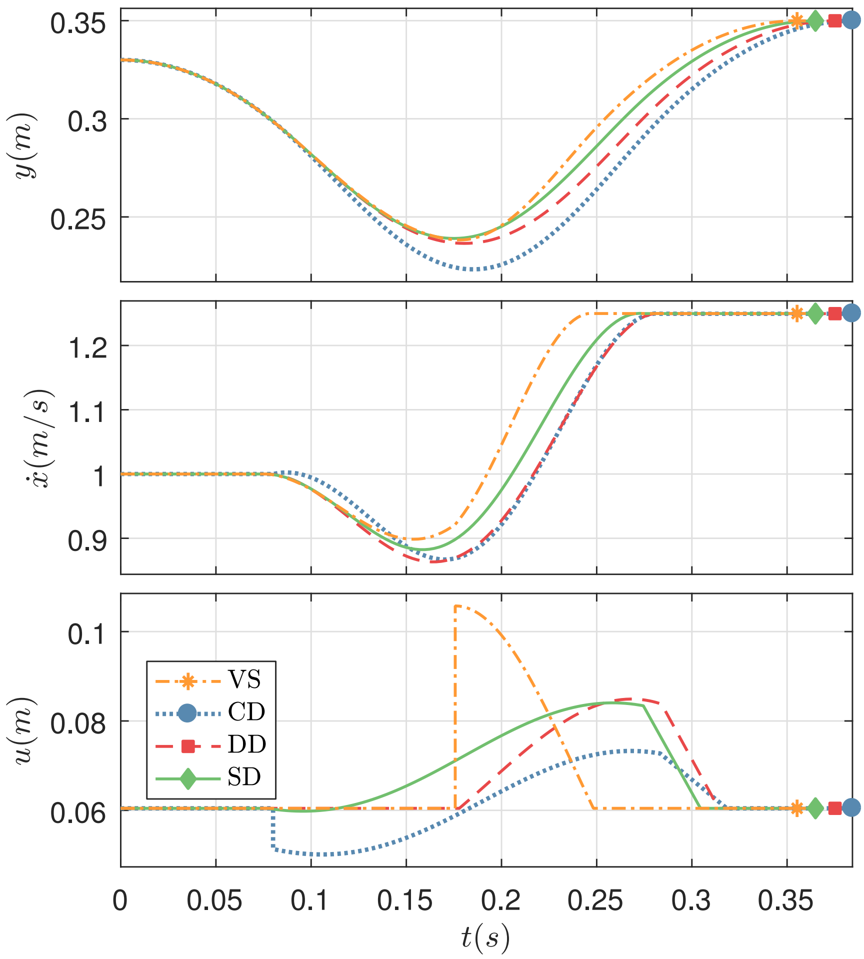

Figure 3.2: An example SESLIP simulation, using the Variable Stiffness (VS), Constant Damping (CD), Decompression-only tunable Damping (DD) and Shifted Tunable Damping (SD) methods to realize a desired apex state within a single stride starting from the same initial condition. After liftoff, the actuator is position retracted to u_0 in a fixed amount of time.

injection and removal within a single stride. In this section, we compare different control strategies regarding their effectiveness in dealing with this limitation. To this end, we consider limits on the actuator position with $|u - u_0| < 0.15 l_0$ for SESLIP, assuming that the required force and power can otherwise be supplied by the actuator. We also assume that the actuator position at touchdown, u_{td} is initialized to ensure maximal use of the actuator range for the control strategy to be used within the subsequent stride. Simulations were conducted for initial conditions, spring stiffnesses and damping ratios in the ranges described in Section 3.7 and with touchdown angles in the range $\theta_{\text{td}} \in \theta^n_{\text{td}} + [-0.25, 0.35]$. We then compute, in each case, the maximum normalized feasible energy injection with

$$\Delta\bar{E}_{max} := \max_{\mathbf{p}, u_{\text{td}}} \frac{E(\mathbf{X}_1(\mathbf{p}, u_{\text{td}}, \theta_{\text{td}})) - E(\mathbf{X}_0)}{mgl_0}$$

subject to the actuator displacement limit constraints throughout stance, where $\mathbf{X}_0$ and $\mathbf{X}_1$ denote initial and final apex states, respectively, $E(\mathbf{X}) := mgz + \frac{1}{2}m\dot{y}^2$ denotes the apex energy and $\mathbf{p}$ denotes parameters associated with a particular control strategy.

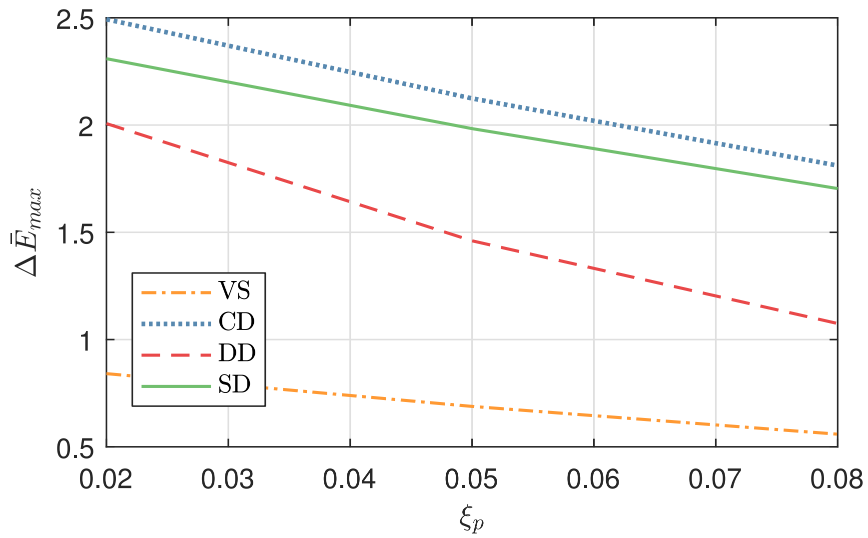

Figure 3.3: The maximum amount of normalized energy that can be injected into the system in a single stride for different control strategies as a function of the physical damping ratio ξ_p.

Figure 3.3 shows average values for this metric across different simulations with respect to different values of the physical damping ratio ξ_p. As expected, the variable stiffness (VS) controller has the lowest energy injection performance since it is limited to only the decompression phase and requires a discontinuous actuator command at bottom. The constant damping (CD) strategy seems to be the best, but still requires a discontinuous actuator command at touchdown as shown in Figure 3.2 and hence is not practical. Among practical alternatives, decompression only variable damping (DD) still only uses the decompression phase and hence is not optimal. Finally, the shifted variable damping strategy (SD) offers the best peformance while still remaining practically feasible, effectively using the entire stance phase for maximal energy injection.

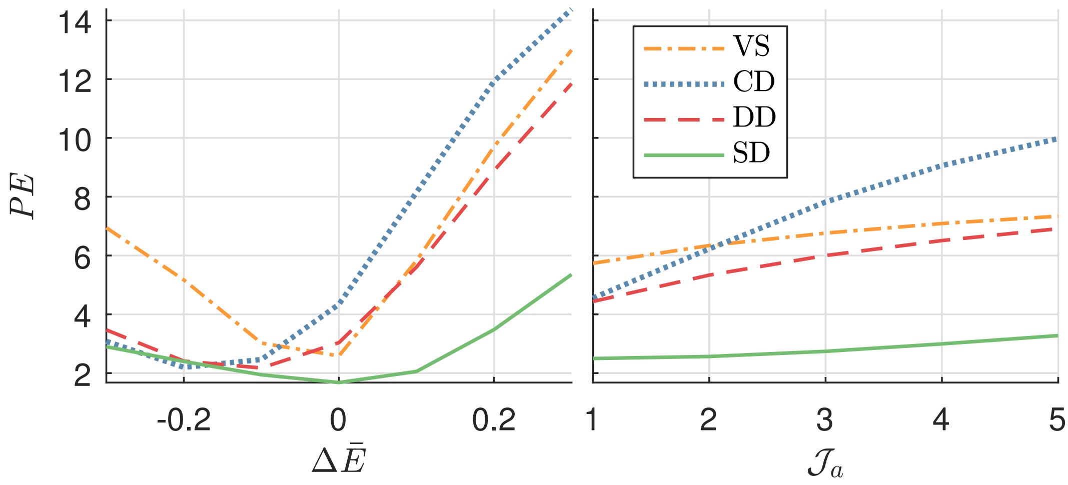

Figure 3.4: Average percentage errors in apex states for single-stride deadbeat control of the SEASLIP model for different controllers as a function of commanded change in normalized energy (left) and reflected actuator inertia (right).

3.7.2 Accuracy of Deadbeat Control for Apex States

The discontinuous actuator commands required by the variable stiffness and constant damping controllers cannot be exactly realized, and hence are expected to have considerable impact on the accuracy of the corresponding template embedding and the performance of the resulting deadbeat gait controller of (3.33). In this section, we compare the deadbeat control accuracy for all controllers described in Section 3.6 using systematic simulations with the SEASLIP model. Limits on actuator performance are imposed with stall force $f_{max}(0) = 12.5mg$ and no-load speed $\dot{u}_{max} = 0.6\sqrt{gl_0}$, mirroring constraints of various platforms with series elastic actuation [15, 35]. Simulations were conducted with the ranges of initial conditions, spring stiffnesses, and damping ratios given in Section 3.7, while considering step commands in normalized apex energy and forward velocity state components in the ranges $\Delta\bar{E} := (E(\mathbf{X}^*) - E(\mathbf{X}_0))/(mgl_0) \in [-0.3, +0.3]$ and $\Delta\bar{\dot{y}} \in [-0.25, +0.25]$, where $\mathbf{X}^*$ denotes the commanded apex state. We also consider nondimensional reflected actuator inertia taking values in the range $\mathcal{J}_a := J_a/(mg) \in [1, 5]$ in order to explore its effects on control accuracy for fixed values of actuator force and speed limits. We evaluate the accuracy of control with a percentage error metrics defined as

$$\text{PE} := 100 \left\| \mathbf{X}^*_{[\dot{y},z]} - \mathbf{X}^f_{[\dot{y},z]} \right\| / \left\| \mathbf{X}^*_{[\dot{y},z]} \right\|.$$

where $\mathbf{X}^f$ denotes the final apex state.

Figure 3.4 shows the mean percentage errors in the realization of desired apex states within a single stride with the different deadbeat control strategies described in Section 3.6 as a function of commanded change in normalized energy (left) and the actuator reflected intertia (right). The mean, standard deviation and maximum errors reported across all experiments are also shown in Table 3.2. As expected, the elimination of discontinuities in desired actuator commands by our shifted damping (SD) control strategy results in much more accurate tracking, and implements effective stabilization of the transverse variable y_1 as shown in Figure 3.5. In contrast, variable stiffness (VS) and constant damping (CD) controllers generate discontinuous actuator position commands and hence cannot accurately realize desired apex states. In other words, the VS and CD controllers fail to stabilize the zero dynamics submanifold in the presence of actuator dynamics and saturation, resulting in poor embedding of SEASLIP. Finally, the decompression-only (DD) tunable damping does not impose a discontinuous position command, but requires an abrupt change in the actuator velocity at bottom, where the large spring force limits the actuator's maximum feasible acceleration to track the actuator command. Consequently, the decompression-only strategy does well in a certain range, until its acceleration demands exceed practical actuator limits, beyond which performance degrades rapidly. In summary, since the shifted tunable damping strategy features smooth actuator motion and spreads out energy transfer throughout the entire stance phase, it has considerably higher accuracy than the alternatives, remaining relatively insensitive to reflected actuator inertia.

3.7.3 Actuator Power Requirements

Our final comparison of controller alternatives considers their power requirements. To this end, we remove actuator limitations and repeat simulations with the same ranges of initial conditions, parameters and apex step commands in Section 3.7.2. In doing so, however, we now measure peak and average power consumption for the radial leg

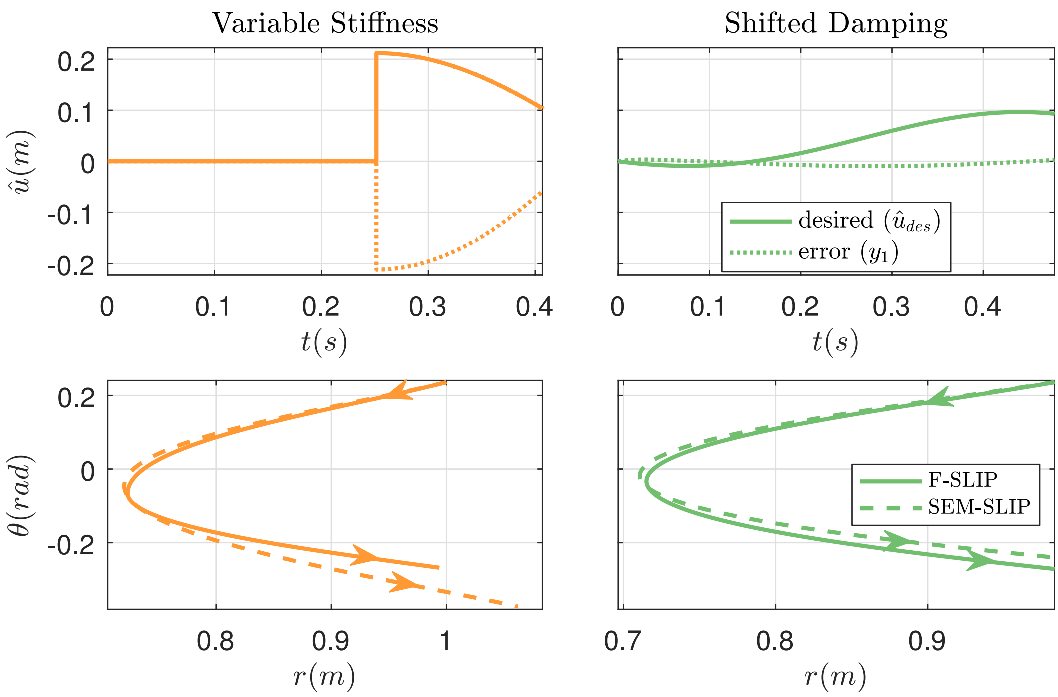

Figure 3.5: Stabilization of transverse dynamics (top) and the phase portrait for the zero dynamics (bottom) during a single stance phase with SEASLIP, embedding the template model FSLIP controlled with Variable Stiffness (left) and Shifted Damping (right) control strategies.

actuator throughout the stance phase of a single stride, which we respectively report using the normalized definitions

$$\bar{P}_{\text{peak}} := \max_{t_{\text{td}} \le t \le t_{\text{lo}}} |\nu(t)\mathcal{F}_a(t)|$$

$$\bar{P}_{\text{avg}} := \frac{1}{t_{\text{lo}} - t_{\text{td}}} \int_{t_{\text{td}}}^{t_{\text{lo}}} |\nu(t)\mathcal{F}_a(t)| \, \mathrm{d}t,$$

with $\nu(t) := \dot{u}/\sqrt{g l_0}$ and $\mathcal{F}_a := f_a/(mg)$.

As expected, our results in Figure 3.6 show that the variable stiffness control has the highest power requirements since the actuator attempts to catch up with the discontinuous actuator position command at bottom. The constant damping controller performs better but still requires significant power due to similar reasons. Decompression-only damping decreases average requirements, but still has high peak power demands due to the discontinuous velocity command for the actuator at bottom. Finally, our shifted damping control strategy has the best performance, offering a dramatic reduc-

Table 3.2: Mean (μ), standard deviation (σ) and maximum ($\max$) values for percentage control accuracy error as well as peak and average power requirements across all simulations.

		VS	CD	DD	SD
PE	μ	6.65	7.51	5.84	2.81
	σ	4.87	7.30	4.70	2.72
	max	27.16	40.34	27.09	21.27
P_{peak}	μ	17.64	7.97	2.97	0.75
	σ	9.65	4.93	3.38	0.62
	max	47.46	26.00	22.53	4.01
P_{avg}	μ	3.43	1.11	0.43	0.34
	σ	2.51	1.09	0.55	0.29
	max	13.16	12.25	4.99	1.95

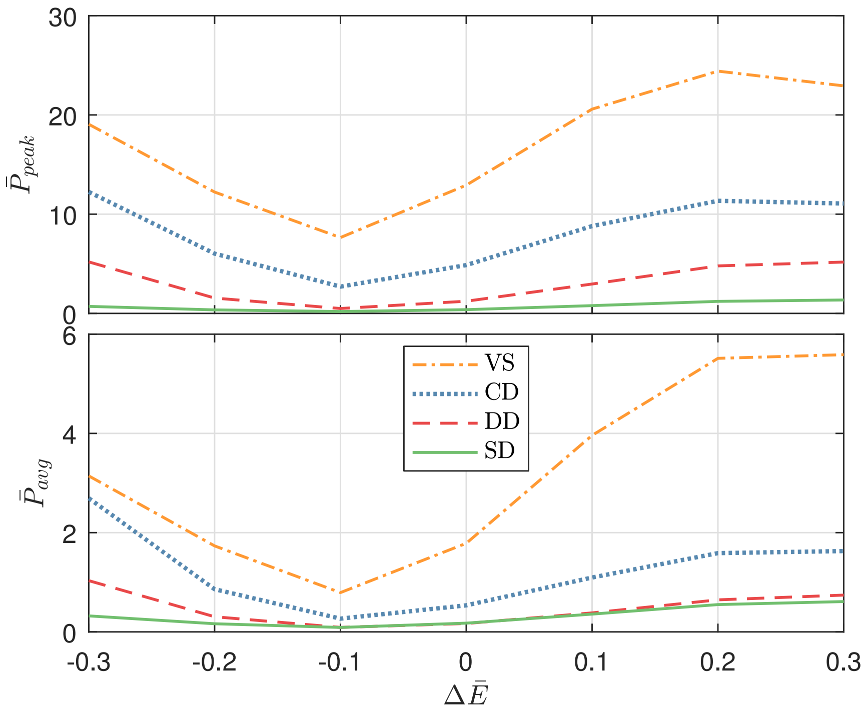

Figure 3.6: Peak (top) and average (bottom) power requirements for all deadbeat control strategies as a function of commanded change in the apex energy level, averaged over different initial conditions, model parameters and velocity commands.

tion in peak and average power requirements as also shown in Table 3.2.

3.8 Conclusion

In this chapter, we introduced a new control strategy for running robots that incorporate a linear actuator in series with the leg compliance. Our strategy is based on tuning the damping of a virtual passively compliant leg attached to a point mass, preserving the spring-mass-damper structure and corresponding approximate solutions to the dynamics during stance [88]. In order to use this strategy on serially-actuated legged platforms with non-negligible actuator dynamics, we proposed a hierarchical modeling and control framework based on the template-anchor idea [27]. In particular, we introduced the FSLIP model for planar running behaviors, incorporating tunable compliance and damping as well as a constant forcing term during stance which still admits approximate but accurate analytic solutions. We then described how single-stride deadbeat controllers can be constructed using different combinations of these tunable parameters. In order to ensure computational efficiency as well as the accuracy of control, our deadbeat controller is based on approximate analytic solutions to stance trajectories, for which we proposed a number of extensions to [88] yielding a significant increase in prediction performance.

Based on this deadbeat control framework, simulations were conducted to show that modulation of the virtual damping coefficient within the FSLIP model offers better performance and efficiency in terms of energy injection capability within a single stride, smaller power requirements on the radial leg actuator, as well as better control accuracy under realistic torque and speed limitations in comparison to an alternative control strategy that relies on modulation of leg stiffness.

CHAPTER 4

EXPERIMENTAL EVALUATION OF VERTICAL SPRING-MASS HOPPING THROUGH VIRTUAL LEG DAMPING

In this chapter, we present the first experimental implementation of the virtual damping-based control of spring-mass behavior on a vertical hopper that we built. While doing so, we present an improved variant of the shifted variable damping from Chapter 3 and a set of controllers within the embedding framework proposed in Chapter 3 in order to transfer the spring-mass behavior to the robot. The work in this chapter has also been submitted to a journal and currently under review [96].

4.1 Introduction

Simplified models of locomotion are widely used in both the design and control of legged robot platforms since they have been shown to be capable of capturing fundamental stability, robustness and controllability properties of locomotory behaviors. Furthermore, they also serve as a useful basis for the design of gait control strategies, allowing regulation of high-level locomotion behaviors abstracted away from remaining redundancies in the possibly complex morphologies of different hardware platforms [89]. In this context, the Spring-Loaded Inverted Pendulum (SLIP) model has long ben used as a powerful model for running behaviors in nature [12] for numerous legged runners with differing number of legs, morphology, and posture [27]. As an abstract representation of the fundamental dynamics of running [30], this model continues to serve as a simple yet useful target model in robotics [116, 68, 21, 22, 118].

A central challenge in the use of the SLIP model to control physical robots is the regulation of system energy, since the simplest SLIP is conservative and hence cannot change its mechanical energy. Different approaches have been proposed in the literature to address this issue, extending the basic model with additional features such as the precompression of the lef spring during flight [121], active modulation of the leg spring during stance [49, 16], or the use of additional forcing elements within the leg structure of the model [84, 81, 77].

In this context, our earlier work [94] proposed virtual tuning of leg damping in the target SLIP model as an efficient way of regulating system energy during vertical hopping, which we later extended to planar running behaviors [95]. The target model we introduced in the latter, which we called FSLIP, incorporates virtually tunable damping and a constant forcing term in addition to the pure compliance of the basic SLIP model to achieve efficient controllability. The primary contributions of the present paper are first, important extensions to both the FSLIP model itself as well as its embedding into platforms with series-elastic actuation (SEA), as well as an experimental validation of the hierarchical, template-based control strategy realized on a vertical hopping platform with SEA. Through extensive simulations and experiments, we show that both the embedding strategy, as well as the novel step-to-step energy controller we propose outperform available alternatives in terms of both accuracy and power requirements for the SEA actuator.

4.2 Target Model : FSLIP

The SLIP model is a point-mass riding on a compliant leg, as shown in Fig. 4.1 (a). Originally, the leg was modeled as a pure spring [1], which results in energetically conservative hopping. However, this is not in line with the needs and objectives of robotic running, as a robot cannot compensate its mechanical energy losses or accelerate/decelerate based on the SLIP model. In Chapter 3, we proposed an extension to the lossless SLIP model with the goal of enabling accurate and efficient control of locomotion energy. The resulting new model, called FSLIP, extends the leg structure of the SLIP model by adding a constant forcing f and a tunable damper d in parallel to the spring k as illustrated in Fig. 4.1 (b). Vertical stance dynamics of this extended

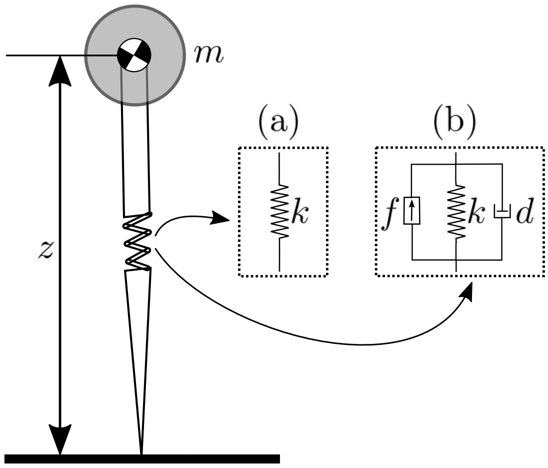

Figure 4.1: Lossless SLIP (a) and FSLIP (b) models of hopping.

FSLIP model take the form

$$\ddot{z} = -\frac{k}{m}(z - z_0) - \frac{d}{m}\dot{z} + \frac{f}{m} - g. \tag{4.1}$$

with z_0 denoting the spring rest length. On the other hand, flight dynamics are described by

$$\ddot{z} = -g. \tag{4.2}$$

As usual, transitions between these phases are marked with touchdown and liftoff events. In particular, the stance phase begins with the touchdown event as the foot comes into contact with the ground, corresponding to the condition

$$z - z_0 = 0, \tag{4.3}$$

and the flight phase begins with the liftoff event, which can be defined as the zero crossing of the ground reaction force (GRF) with

$$k(z - z_0) + d\dot{z} - f = 0. \tag{4.4}$$

Finally, the hopping height, which can be identified with the apex coordinate $h := z$ at the highest point during flight (i.e., $\dot{z} = 0$), can be controlled by changing parameters of this model once per step, as discussed in [29]. In this regard, composition of flight and stance dynamics leads to a return map from the i^{th} apex to the next with dependence on tunable model parameters $\mathbf{p}$ in the form $h_{i+1} = \mathcal{R}(h_i, \mathbf{p})$. This discrete formulation of dynamics admits once per step adjustments to $\mathbf{p}$ as control inputs for the realization of a desired apex $h^\star$ with

$$\mathcal{R}(h_i, \mathbf{p}) = \mathbf{h}^\star. \tag{4.5}$$

For instance, in Chapter 2, leg damping was used as the only control input $\mathbf{p} = [d]$, which was computed through direct inversion of the return map with $d = \mathcal{R}^{-1}(h^\star, h_i)$.

4.3 Model-Based Control of Hopping on Robots with Series Elastic Actuators

Following the concept of templates and anchors introduced by [27], we have previously developed a methodology in Chapter 3 to realize SLIP-like running behavior on legged robotic platforms, by embedding the target model into the robot through intermediate models hierarchically interconnected via control laws. This hierarchical strategy allows decomposition of the embedding problem into simpler subproblems and derivation of mathematically more tractable anchoring strategies compared to direct control of the full platform towards a behavior defined by the target model.

In subsequent subsections, we describe an improved control approach that fits into this hierarchical framework. In this context, Fig. 4.2 shows our setup where the target model (TM) is embedded into a vertically constrained robot, called robot model (RM), through an intermediate model (IM), with moderate complexity relative to RM and TM. In particular, this is achieved by means of a cascaded control system with two controllers which, first, embed the TM into IM and, then, translate the IM dynamics to the RM.

4.3.1 The Intermediate Model

As suggested by [49] and [51], a vertical hopping robot with a series elastic actuator (SEA) can be modeled as illustrated in Fig. 4.2 (a). Compared to TM dynamics, this model has an additional degree of freedom associated with the SEA coordinate δ. As a simpler alternative, an IM can be introduced by treating the SEA as an ideal displacement source perfectly realizing the position commands, hence instantaneously affecting spring deflection. The resulting model illustrated in Fig. 4.2(b) is a revised

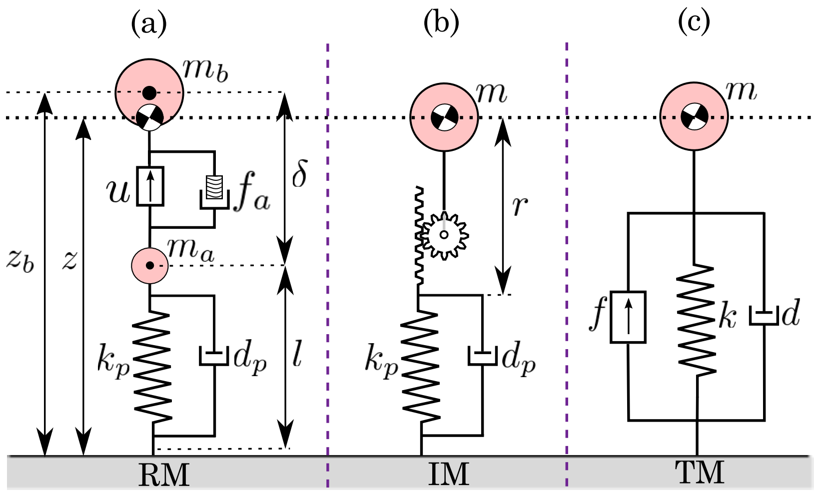

Figure 4.2: A hierarchy of models for vertical hopping starting from the RM to the TM to be realized via an IM.

version of the SE-SLIP model in Chapter 3, which was unable to accurately represent robots with SEA since the lossy element d_p was connected between the COM and the toe for simplicity. The new model in this chapter brings this to a more realistic structure.

Stance dynamics of the IM take the form

$$\ddot{z} = -\frac{k_p}{m}(z - r - l_0) - \frac{d_p}{m}(\dot{z} - \dot{r}) - g \tag{4.6}$$

where r denotes the desired actuator position, k_p spring stiffness, d_p viscous damping, and l_0 rest length of the spring. Dynamics of the flight phase are identical to those of the TM given in (4.2).

4.3.2 Embedding TM dynamics into the IM

The IM can realize the dynamics of TM by reproducing its body accelerations with the position-commanded SEA. During flight, dynamics are already identical, hence the SEA can be employed to realize a desired touchdown length z_{td} by maintaining a constant actuator position with

$$r(t) := r_{\text{td}} = z_{\text{td}} - l_0 \,, \tag{4.7}$$

allowing us to effectively control the rest length as $z_0 = z_{\text{td}}$. In contrast, during stance, TM accelerations can be realized by tracking SEA trajectories defined in the form of a linear differential equation obtained by $(\ddot{z})_{\text{IM}} = (\ddot{z})_{\text{TM}}$ (i.e., equating (4.1) to (4.6)) as

$$r + \frac{d_p}{k_p}\dot{r} = r_{\text{td}} + \frac{k_p - k}{k_p}(z - z_{\text{td}}) + \frac{d_p - d}{k_p}\dot{z} + \frac{f}{k_p} \tag{4.8}$$

The general solution to this differential equation can be formulated as

$$r(t) = r_c(t) + r_p(t) \tag{4.9}$$

where r_c and r_p respectively denote the complementary and particular solutions with the former computed as

$$r_c(t) = (r_{\text{td}} - r_p(0))\ e^{-\frac{k_p}{d_p}t}\,. \tag{4.10}$$

To solve for the latter, the method of undetermined coefficients can be employed [107]. Below, we describe a method which does not require an explicit analytical expression of $z(t)$ to facilitate this procedure. As in [64], defining the differential operator as $D := \mathrm{d}/\mathrm{d}t$, we rewrite (4.6) as

$$\left(1 + \frac{d_p}{k_p}D\right) r(t) = R + \left(\frac{k_p - k}{k_p} + \frac{d_p - d}{k_p}D\right) z(t)$$

with the remainder term $R := r_{\text{td}} + (f + (k - k_p)z_{\text{td}})/k_p$. Following the work presented by [18], we now make a guess for the particular solution based on a polynomial in the indeterminate D as

$$r_p(t) = c_0 + (c_1 + c_2 D)z(t) \tag{4.11}$$

with c_0, c_1, and c_2 denoting unknown constants. Differentiating this equation and using (4.1), we obtain

$$\dot{r}_p(t) = c_2\frac{kz_{\text{td}} + f - mg}{m} + \left[\left(c_1 - c_2\frac{d}{m}\right)D - c_2\frac{k}{m}\right]z(t).$$

Substituting r_p and $\dot{r}_p$ into (4.8) and equating coefficients of terms with the same power of D yields a linear system of equations which admits the solution in the form

$$\begin{bmatrix} c_0 & c_1 & c_2 \end{bmatrix}^T = \boldsymbol{A}^{-1}b \tag{4.12}$$

$$\text{with } \boldsymbol{A} := \begin{bmatrix} 0 & -k_p & d_p k/m \\ 0 & -d_p & d_p d/m - k_p \\ -k_p & 0 & -d_p(k z_{\text{td}} + f - mg)/m \end{bmatrix}$$

$$b := \begin{bmatrix} k_p - k \\ d_p - d \\ k z_{\text{td}} + f - k_p l_0 \end{bmatrix}.$$

With this solution, the SEA trajectory during stance can be computed according to (4.9).

4.3.3 Embedding IM dynamics into RM

Having embedded the TM dynamics into the IM, we now proceed with the realization of IM dynamics within the robot model, RM. This can be accomplished by controlling COM accelerations $\ddot{z}$ of the robot to track those of the IM. Firstly, robot dynamics can be expressed as

$$\begin{aligned} \ddot{z} &= -g - c_s F_{sea}/m \\ \ddot{\delta} &= \left(u + c_s \frac{m_b}{m} F_{sea} - f_a(\dot{\delta})\right)/J_a \end{aligned} \tag{4.13}$$

with the SEA force F_{sea} and phase selector c_s defined as

$$\begin{aligned} F_{sea} &:= k_p \left(z - \frac{m}{m_b}\delta - l_0\right) + d_p \left(\dot{z} - \frac{m}{m_b}\dot{\delta}\right) \\ c_s &:= \begin{cases} 1 & \text{stance} \\ 0 & \text{flight} \end{cases} \end{aligned}.$$

Here, J_a denotes the reflected actuator inertia, f_a the actuator friction, $m := m_b + m_a$ the total mass consisting of body mass m_b and actuator mass m_a, and k_p, d_p, and l_p defines the stiffness, damper, and rest length of the spring.

In order to embed IM into RM, we want $(\ddot{z})_{\text{RM}} = (\ddot{z})_{\text{IM}}$, which can be satisfied by indirectly controlling COM acccelerations of the robot through SEA. Observe from (4.13) that $\ddot{z}$ during stance is determined by F_{sea}, which is mediated by the SEA displacement δ. On the other hand, during flight, the COM accelerations match exactly those of the IM without the need for any control. Nevertheless, as in Section 4.3.2, the robot should prepare for the next step by adjusting its touchdown length which can again be realized by controlling δ during flight. For both stance and flight, the desired SEA position can be computed as

$$\delta_d(t) := (m/m_b)r(t), \tag{4.14}$$

which can be realized by a trajectory tracking controller. In this regard, neglecting the internal actuator friction f_a, a feedback linearization (FL) controller can be formulated as

$$u = -c_s(m_b/m)F_{sea} + u_{\text{fb}}, \tag{4.15}$$

where the former term cancels the counteracting SEA force, thus reducing the remaining actuator dynamics into the Brunovsky normal form [52] excited by the feedback part with

$$J_a\ddot{\delta} = u_{\text{fb}}, \tag{4.16}$$

This admits a feedback tracking controller in the form

$$u_{\text{fb}} = J_a\left[\ddot{\delta}_d + K_p(\delta_d - \delta) + K_d(\dot{\delta}_d - \dot{\delta})\right],$$

which stabilizes the dynamics (4.16) for any $K_p > 0$ and $K_d > 0$, hence rendering the zero dynamics set

$$\mathcal{Z} := \{(z, \delta, \dot{z}, \dot{\delta})^T : \delta = \delta_d \wedge \dot{\delta} = \dot{\delta}_d\}$$

an attracting invariant manifold with $\delta = \delta_d = (m/m_b)r$ by (4.14). Thus, $(\ddot{z})_{RM} = (\ddot{z})_{IM}$ is enforced, guaranteeing the desired embedding of IM dynamics into RM.

4.4 Controlling FSLIP with Variable Damping

4.4.1 Analysis of Feasible TM Policies

Desired SEA trajectories resulting from a specific target model should be continuously differentiable for accurate embedding, since motors cannot discontinuously change their position or velocity. In this regard, for the target model FSLIP, whose resulting SEA trajectories are given in (4.7) and (4.9), both discontinuities can be eliminated by enforcing constraints at touchdown with

$$\begin{aligned} r_c(0) &= r_{\text{td}} - r_p(0) \\ \dot{r}_c(0) &= -\dot{r}_p(0) \end{aligned}. \tag{4.17}$$

The former is a position constraint which is satisfied regardless of tunable TM parameters $\boldsymbol{p}$ in (4.5), thanks to the complementary solution $r_c(t)$ given in (4.10). However, these exponential $r_c(t)$ trajectories are too fast for SEA motors to track. Consider, for example, the ATRIAS bipedal robot whose SEA control bandwidth was reported by [68] to be 20 Hz compared to the required decay constant $k_p/d_p = 200Hz$ of $r_c(t)$, computed from parameters in [46]. In order to solve this problem while still satisfying continuity constraints, we seek to also enforce $r_c(t) = 0$ with

$$\begin{aligned} r_p(0) &= r_{\text{td}} \\ \dot{r}_p(0) &= 0, \end{aligned} \tag{4.18}$$

which can be satisfied by choosing a suitable set of model parameters $\boldsymbol{p}$ of TM and their corresponding solutions.

Another aspect to consider for the feasibility of policies is their energetic demands. For this purpose, we define the SEA output power and the net SEA work required by the energy difference between the desired and initial apex points, respectively, as

$$\begin{aligned} P_{\text{sea}}(t) &:= \dot{r}(t) F_{\text{sea}}(t) \\ (\Delta E)_{\text{sea}} &:= mgh^\star - mgh_0 + E_{\text{loss}} = \int_{t_{\text{td}}}^{t_{\text{lo}}} P_{\text{sea}}(t) dt \end{aligned} \tag{4.19}$$

where E_{loss} denotes the dissipated energy from touchdown t_{td} to liftoff t_{lo}. For maximally efficient control, we require

$$(\Delta E)_{\text{sea}} P_{\text{sea}}(t) \geq 0 : \ \forall t. \tag{4.20}$$

In subsequent sections, we will also consider this constraint for efficiency in designing policies that choose $\boldsymbol{p}$ of a TM. In particular, we present three policies in the order of ascending complexity, starting with a preliminary approach satisfying only position constraint in (4.18) to the ultimate goal of satisfying all three constraints obtained by combining (4.18) and (4.20).

4.4.2 Existing Policy : Shifted Variable Damping

Chapter 3 proposed a strategy called shifted variable damping (SVD) which tunes parameters $\boldsymbol{p} := [d, f]$ of the FSLIP once per step with fixed spring stiffness $k = k_p$ to reach a desired apex height $h^\star$, while satisfying the position constraint in (4.18).

For the revised IM in this chapter, this can be formulated by extending the problem in (4.5) to two equations as

$$\begin{bmatrix} \mathcal{R}(h_i, \boldsymbol{p}) \\ r_p(0) \end{bmatrix} = \begin{bmatrix} h^\star \\ r_{\text{td}} \end{bmatrix}, \tag{4.21}$$

which can be solved to find unknowns d and f. From the second equation, the solution to f for the revised IM can be obtained in terms of d with

$$f = \frac{(k_p \dot{z}_{\text{td}} + g d_p)(d - d_p)}{k_p}, \tag{4.22}$$

whereas d can be numerically solved from the first equation, after plugging (4.22) into the return map R. With these solutions, the SVD policy is completely specified, guaranteeing the positional continuity of resulting SEA trajectories $r^{\text{svd}}(t)$. However, as illustrated by the dotted-blue lines in Fig. 4.3, the SEA velocities $\dot{r}^{\text{svd}}(t)$ turn out to be discontinuous, violating the second constraint in (4.18). This problem occurs for all cases with the exception of $d = d_p$ corresponding to a case where IM is passively identical to TM without any need for control. This is stated more formally by the following proposition. Before presenting the Proposition and its proof, however, we find it useful to present some assumptions and remarks.

Assumption 2. *Physical leg damping d_p and virtual leg damping d satisfy the inequalities*

$$\begin{aligned} d_{p\,\text{max}} &:= 2\,\xi_{p\,\text{max}}\sqrt{k_p m} \geq d_p \geq d_{p\,\text{min}} := 0 \\ d_{\text{max}} &:= 2\,\xi_{\text{max}}\sqrt{k_p m} \geq |d| \end{aligned}$$

with maximum damping ratios $\xi_{p\,\text{max}} = \xi_{\text{max}} = 0.2$ to maintain oscillatory leg motion.

Remark 1. *Assumption 2 leads to*

$$\begin{aligned} mk_p - d_p^2 > mk_p - d_{p\,\text{max}}^2 = 0.84 mk_p > 0 \\ mk_p - d_p d > mk_p - d_{p\,\text{max}} d_{\text{max}} = 0.84 mk_p > 0 \cdot \\ mk_p - d^2 > mk_p - d_{\text{max}}^2 = 0.84 mk_p > 0 \end{aligned}$$

Remark 2. *As evidenced in Chapter 2, the change in mechanical energy ΔE of FSLIP during stance is a monotonically decreasing function of leg damping, that is*

$$\Delta E \propto -d.$$

Assumption 3. *FSLIP model parameters are constrained to satisfy* $\dddot{z}_{\mathrm{td}} > 0$ *and* $\ddot{z}_b \geq \ddot{z}_{\mathrm{td}}$ *to avoid foot rebounding.*

Remark 3. *The analytical solution to FSLIP stance dynamics (4.1) takes the form*

$$z(t)=\Delta z_{\mathrm{td}}+\left[\tilde{z}_{\mathrm{td}}\cos(t\tilde{\omega}_n)+\frac{2m\dot{z}_{\mathrm{td}}+\tilde{z}_{\mathrm{td}}d}{2m\tilde{\omega}_n}\sin(t\tilde{\omega}_n)\right]e^{\frac{-dt}{2m}} \tag{4.23}$$

with the initial offset $\Delta z_{\mathrm{td}} := z_{\mathrm{td}} - \tilde{z}_{\mathrm{td}}$, $\tilde{z}_{\mathrm{td}} := \frac{mg-f}{k}$, *and damped frequency* $\tilde{\omega}_n := \frac{\sqrt{4km-d^2}}{2m}$ *Using the identity* $A\cos x + B\sin x = R\cos(x-\phi)$ *with* $R = \sqrt{A^2+B^2}$ *and* $\phi = \mathrm{atan2}(B, A)$, *we can rewrite (4.23) as*

$$z(t) = \Delta z_{\mathrm{td}} + R_0\cos(\tilde{w}_n t - \phi_0)e^{\frac{-dt}{2m}}$$

for some R_0 *and* ϕ_0. *Derivatives of* $z(t)$ *can also be written in a similar form*

$$\frac{\mathrm{d}^i z(t)}{\mathrm{d}t^i} = R_i\cos(\tilde{w}_n t - \phi_i)e^{\frac{-dt}{2m}} \tag{4.24}$$

for some R_i *and* ϕ_i.

Remark 4. *Body acceleration of the FSLIP model satisfies* $\ddot{z}_{\mathrm{b}} > 0$, *since the bottom event identified with the subscript b connects stance compression and decompression phases where we have* $\dot{z} \leq 0$ *and* $\dot{z} > 0$, *respectively.*

Proposition 1. *The SEA trajectories for IM under the SVD policy,* $r^{\mathrm{SVD}}(t)$, *are not differentiable at touchdown unless* $d = d_p$.

Proof. *We will use the proof by contradiction to prove the proposition. In this regard, suppose that the proposition does not hold, meaning that left and right derivatives of* $r(t)$ *are equal at touchdown with* $\dot{r}(t_{\mathrm{td}}^-) = \dot{r}(t_{\mathrm{td}}^+)$. *In this regard, as the desired SEA displacement during flight is defined to be constant by (4.7), the SEA velocity just prior to touchdown is obtained as* $\dot{r}(t_{\mathrm{td}}^-) = 0$. *On the other hand, differentiating the SEA trajectory (4.9) during stance, substituting the position constraint of (4.17), which is satisfied by the SVD, and using (4.11) yields*

$$\dot{r}(t) = \dot{r}_p(t) = c_1\dot{z} + c_2\ddot{z}. \tag{4.25}$$

As dynamics of the IM are identical to those of the TM, we can substitute the stance acceleration (4.1) of FSLIP to obtain

$$\dot{r}(t)=\left[c_1 - c_2\frac{d}{m}\right]\dot{z} + c_2\left[-\frac{k}{m}(z-z_{\mathrm{td}}) + \frac{f}{m} - g\right].$$

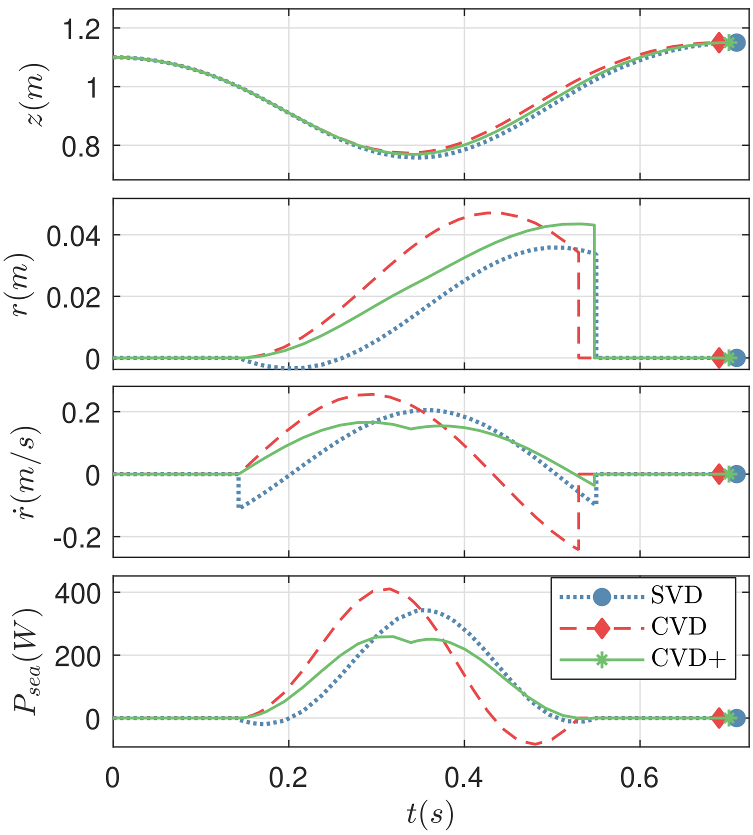

Figure 4.3: A simulation example with the IM, using SVD (dotted-blue), CVD(dashed-red), and CVD+(solid green) policies to realize the same desired apex state within a single stride starting from the same initial condition.

Substituting the leg parameters defined in Sec. 4.4.2 for the SVD policy, solutions to coefficients given by (4.12), and touchdown conditions, we obtain

$$\dot{r}(t_{\text{td}}^{+}) = -\frac{g(d_p - d)}{k_p}, \tag{4.26}$$

which automatically raises a contradiction with the initial assumption $\dot{r}(t_{\text{td}}^{-}) = \dot{r}(t_{\text{td}}^{+})$.

□

The example in Fig. 4.3 also shows that SEA trajectories under the SVD policy remove some of the useful SEA work in both compression and decompression phases, resulting in inefficient embedding since the SEA has to compensate for this wasted energy by channelling more power in the remaining periods. In the following proposition, we discover that the negative work occurs in all cases with $d \neq d_p$.

Proposition 2. *If* $d \neq d_p$*, then there exists sub-intervals* $T_c \subset [t_{\text{td}}, t_{\text{b}}]$ *and* $T_d \subset$

$[t_\mathrm{b},\, t_\mathrm{lo}]$ *in which the SEA works against the desired net energy transfer with*

$$P_{sea}^{\mathrm{svd}}(t)(\Delta E)_{\mathrm{sea}}^{\mathrm{svd}} < 0 : \forall t \in T_c \vee \forall t \in T_d \,.$$

Proof. *As explained in Sec. 4.3, the RM embeds the target model FSLIP tuned according to the SVD policy with leg damping* d *by performing the net actuator work* $(\Delta E)_\mathrm{sea}$ *on COM dynamics. On the other hand, when the SEA is turned off at a fixed position with* $\dot{r} = \ddot{r} = 0$*, the RM passively reduces to the TM with* $d = d_p$*. Therefore, it can be said that the net SEA work provides the energy difference between these two cases, which can be formulated as*

$$(\Delta E)_\mathrm{sea} = (\Delta E)_\mathrm{COM}(d) - (\Delta E)_\mathrm{COM}(d_p) \tag{4.27}$$

where $(\Delta E)_\mathrm{COM}$ *denotes the change in total mechanical energy of robot's COM during stance. By Remark 2,* $(\Delta E)_\mathrm{sea}$ *is proportional to the difference in the damping values as*

$$(\Delta E)_\mathrm{sea}(d) \propto d_p - d.$$

Therefore, the statement in the proposition can be translated to

$$P_\mathrm{sea}(t) \neq \alpha(t)(d_p - d) : \forall t \in T_c \vee \forall t \in T_d$$

for some $\alpha(t) \geq 0$*. Using (4.19) and the fact that* F_sea*, defining the ground reaction force, is positive during stance, this condition can be alternatively expressed as*

$$\dot{r}(t) \neq \alpha(t)(d_p - d) : \forall t \in T_c \vee \forall t \in T_d$$

In this regard, the SEA velocity (4.25) can be expressed in a more explicit form by substituting solutions to coefficients given by (4.12) and leg parameters defined in Sec. 4.4.2 for the SVD policy as

$$\dot{r} = \frac{(d_p - d)}{mk_p - (d - d_p)d_p} h(t) \tag{4.28}$$

with

$$h(t) := m\ddot{z} + d_p\dot{z} = F_\mathrm{sea} - mg + d_p\dot{z}. \tag{4.29}$$

Observe that the denominator satisfies

$$mk_p - (d - d_p)d_p \geq mk_p - dd_p \geq mk_p(1 - 4\xi_\mathrm{max}^2) > 0 \tag{4.30}$$

by the Assumption 2. Therefore, the proposition can be proved by showing

$$h(t) < 0 : \forall t \in T_c \vee \forall t \in T_d.$$

Consider, first, the compression phase with $t \in [t_{\mathrm{td}}, t_{\mathrm{b}}]$. *Note that* $\dot{z}(t_{\mathrm{b}}) = 0$ *and* $\ddot{z}(t_{\mathrm{b}}) > 0$, *which yields* $h(t_{\mathrm{b}}) > 0$. *On the other hand, substituting touchdown conditions into (4.29), we obtain*

$$h(t_{\mathrm{td}}) = -\frac{(mk_p - (d - d_p)d_p)g}{k_p} < 0.$$

Since $h(t)$ *is continuous, the pre-image of* $[h(t_{\mathrm{td}}), 0]$ *is compact corresponding to an interval* $[t_{\mathrm{td}}, t_x]$ *with* $h(t_x) = 0$ *and* $t_{\mathrm{td}} < t_x < t_{\mathrm{b}}$. *In this interval,* $h(t)$ *is negative, which concludes the proof for the compression part.*

Consider, now, the remaining phase, which is the decompression phase with $\dot{z} > 0$. *The decompression ends with the liftoff event, triggered by the condition* $F_{sea} = 0$ *as given in (4.4). Therefore, at liftoff, we have* $\ddot{z}(t_{\mathrm{lo}}) = -g$ *which yields*

$$h(t_{\mathrm{lo}}) = -mg + d_p \dot{z}_{\mathrm{lo}}.$$

This is negative unless liftoff velocity is impractically large. To see this, consider, for example, the ATRIAS bipedal robot with $k_p = 6500N/m$, $m = 60kg$ *and* $d_p = 35Ns/m$ *[46] leading to*

$$h(t_{\mathrm{lo}}) > 0 \iff \dot{z}(t_{\mathrm{lo}}) > 16.8\ m/s$$

which is not feasible, suggesting the contrary $h(t_{\mathrm{lo}}) < 0$ *to be true. Finally, continuity of* $h(t)$ *implies that the pre-image set* $h^{-1}([0, h(t_{\mathrm{lo}})])$ *is a non-empty and compact interval, concluding the decompression part of the proof.* □

4.4.3 A New Policy : Coupled Variable Damping

A more feasible policy can be obtained by simultaneously satisfying position and velocity constraints in (4.18). Considering the primary goal of reaching a desired apex $h^\star$, this problem can be posed as a system of equations by incorporating the velocity constraint of (4.18) into (4.21) with

$$\begin{bmatrix} \mathcal{R}(h_i, \boldsymbol{p}) \\ r_p(0) \\ \dot{r}_p(0) \end{bmatrix} = \begin{bmatrix} h^\star \\ r_{\mathrm{td}} \\ 0 \end{bmatrix}. \tag{4.31}$$

To solve these three equations, we propose to tune all leg parameters, corresponding to $\boldsymbol{p} = [d, f, k]$. In this regard, the last two equations admit analytical solutions to f and k as

$$\begin{aligned} f &= (d - d_p)\dot{z}_{\mathrm{td}} \\ k &= k_p \left(1 + \frac{(d - d_p)g}{d_p g + k_p \dot{z}_{\mathrm{td}}}\right), \end{aligned} \tag{4.32}$$

which can be substituted into the first equation to solve for d as well. With these choices of leg parameters, we obtain a more feasible instantiation of FSLIP corresponding to a new policy which we call Coupled Variable Damping (CVD). As illustrated in Fig. 4.3, this policy eliminates the negative work during the compression and SEA discontinuities at touchdown compared to SVD. However, as evidenced by the next Proposition, the negative work in the decompression still exists. Before doing so, however, we find it useful to present a Lemma and its Corollary for intermediate results to be used in the Proposition.

Lemma 2. *Body acceleration of the FSLIP model in stance compression phase satisfies* $\ddot{z}(t) > \ddot{z}_{\mathrm{td}}\ \forall\ t\ \in (t_{\mathrm{td}}, t_b]$.

Proof. *We will prove the statement separately for two cases* $\ddot{z}_{\mathrm{td}} \leq 0$ *and* $\ddot{z}_{\mathrm{td}} > 0$.

Consider, first, $\ddot{z}_{\mathrm{td}} \leq 0$. *Since* $\dddot{z}_{\mathrm{td}} > 0$ *by Assumption 3 and* $\exp(-t\,d/(2m)) > 0$ *for* $t \geq 0$, *evaluating (4.24) for* $i = 2$ *leads to*

$$\cos(-\phi_2) \leq 0 \implies -\pi < -\phi_2 \leq -\pi/2.$$

Noting that $\sin(-\phi_2) \leq 0$, *we differentiate (4.24) with* $i = 2$ *to obtain*

$$\dddot{z} = R_2 e^{\frac{-dt}{2m}} \left[-\tfrac{d}{2m}\cos(\tilde{w}_n t - \phi_2) - \tilde{w}_n \sin(\tilde{w}_n - \phi_2)\right]. \tag{4.33}$$

Suppose $-\phi_2 \leq \tilde{w}_n t - \phi_2 \leq -\pi/2$. *In this interval,* $\cos() \leq 0$ *and* $\sin() < 0$. *Therefore,* $\dddot{z}(t) \geq 0$ *for* $d \geq 0$. *On the other hand, when* $d < 0$, *we have*

$$-\tfrac{d}{2m}\cos(\tilde{w}_n t - \phi_2) \geq -\tfrac{d}{2m}\cos(-\phi_2),$$

which yields $\dddot{z}(t) \geq \dddot{z}_{\mathrm{td}} > 0$. *The positivity of jerk in both cases leads to the result*

$$\ddot{z}(t) > \ddot{z}_{\mathrm{td}}\ \ \forall t:\ -\phi_2 \leq \tilde{w}_n t - \phi_2 \leq -\pi/2.$$

Furthermore, for $-\pi/2 < \tilde{w}_n t - \phi_2 \leq +\pi/2$, *we have* $\cos(\tilde{w}_n t - \phi_2) \geq 0$, *hence its substitution into (4.24) extends the result*

$$\ddot{z}(t) \geq \ddot{z}_{\mathrm{td}}\ \ \forall t:\ -\phi_2 \leq \tilde{w}_n t - \phi_2 \leq +\pi/2. \tag{4.34}$$

On the other hand, for $\pi > \tilde{w}_n t - \phi_2 > \pi/2$, including the liftoff time, we have $\ddot{z}(t) < 0$. Putting these observations together, we conclude that the result (4.34) covers the entire compression phase since $\ddot{z}_b > 0$ at bottom by Remark 4. Therefore, proof of the statement in the Proposition is completed for $\ddot{z}_{\rm td} \leq 0$.

Consider, now, the remaining case $\ddot{z}_{\rm td} > 0$ corresponding to $-\pi/2 < -\phi_2 < 0$. Note, first, that $\cos(-\phi_2) > 0$ and $\sin(-\phi_2) < 0$ in this case. We will present the proof separately for $\mathrm{d} \leq 0$ and $\mathrm{d} > 0$. In this regard, we move on firstly with $\mathrm{d} \leq 0$. In this case, we have $e^{-\frac{dt}{2m}} > 1$ and $\cos(\tilde{w}_n t - \phi_2) > \cos(-\phi_2)\ \forall\ -\phi_2 \leq \tilde{w}_n t - \phi_2 \leq \phi_2$. To prove $\ddot{z}(t) > \ddot{z}_{\rm td}$, we, fist, define a new event identifying the second occurrence of the touchdown acceleration with $\ddot{z}(t_{\rm td2}) = \ddot{z}_{\rm td}$. Using the bounds given above for the exponential and trigonometric terms, the event equation yields $\pi/2 > \tilde{w}_n t_{\rm td2} - \phi_2 \geq \phi_2$. Since $\ddot{z}(t)$ is a continuous function and $\ddot{z}(t_{\rm td2}) = \ddot{z}_{\rm td} > 0$, the maximum point $\ddot{z}(t_{\rm max}) = \max_t \ddot{z}(t)$ is attained in the interval $t_{\rm max} \in [0, t_{\rm td2}]$. The maxima further satisfies

$$\tfrac{k}{m}\dot{z}(t_{\rm max}) - \tfrac{d}{m}\ddot{z}(t_{\rm max}) = 0 \implies \dot{z} = -\tfrac{d}{k}\ddot{z}_{\rm max}, \tag{4.35}$$

thus implying $\dot{z}(t_{\rm max}) > 0$ since $\ddot{z}(t_{\rm max}) > \ddot{z}_{\rm td} > 0$ and $d \leq 0$. This lets us infer that both $t_{\rm td2}$ and $t_{\rm max}$ occurs in the decompression phase. As a result, we conclude that $\ddot{z}(t) \geq \ddot{z}_{\rm td}\ \forall t$ in the compression phase when $d \leq 0$. Consider, now, the last case $\mathrm{d} > 0$. In this case, it can be seen from (4.35) that $t_{\rm max}$ occurs in the compression phase, which implies $t_{\rm b} > t_{\rm max}$. Since $\dddot{z}(t) \geq 0\ \forall t \in [0, t_{\rm max}]$ by continuity, we have $\ddot{z}(t) \geq \ddot{z}_{\rm td}$ before the maxima. Furthermore, the maxima occurs in $-\pi/2 < \tilde{w}_n t_{\rm max} - \phi_2 < 0$ since evaluating (4.33) at $\tilde{w}_n t - \phi_2 = 0$ yields $\dddot{z}(\phi_2/\tilde{w}_n) < 0$. Therefore, we have $\dddot{z}(t) < 0$ for

$$\tilde{w}_n t_{\rm max} - \phi_2 + \pi > \tilde{w}_n t - \phi_2 > \tilde{w}_n t_{\rm max} - \phi_2.$$

In this interval, including both $t_{\rm b}$ and $t_{\rm td2}$, the relation $\ddot{z}_b > \ddot{z}_{\rm td2}$, introduced by Assumption 3, requires $t_b < t_{\rm td2}$. As a result, we obtain

$$\ddot{z}(t) \geq \ddot{z}_{\rm td}\ \forall\ \tilde{w}_n t_{\rm max} - \phi_2 < t \leq t_b$$

corresponding to the period of time in the compression after the maxima, hence concluding the proof for the case $\mathrm{d} \leq 0$ and $\ddot{z}_{\rm td} > 0$.

Corollary 1. *Body acceleration $\ddot{z}(t)$ monotonically decreases after $t_{\rm max}$, satisfying*

$$\ddot{z}(t_1) < \ddot{z}(t_2) \leq 0\ :\ \forall\ t_{\rm lo} > t_1 > t_2 \geq t_{\rm max}.$$

The proof can be seen by following the arguments developed for the proof of Prop. 2.

Proposition 3. *When using the CVD policy, if $d \neq d_p$, then the following relations hold*

$$\begin{array}{l} \forall\, d,\ \{t_{\text{td}} \leq t \leq t_{\text{b}} : P^{\text{cvd}}_{sea}(t)(\Delta E)^{\text{cvd}}_{\text{sea}} < 0\} = \varnothing \\ \exists\, d,\ \{t_{\text{b}} \leq t \leq t_{\text{lo}} : P^{\text{cvd}}_{sea}(t)(\Delta E)^{\text{cvd}}_{\text{sea}} < 0\} \neq \varnothing \end{array}.$$

Proof. *The statement basically claims that the negative actuator power of the SVD policy is eliminated in compression but still present in the decompression. As explained in Proof of Prop.2, this claim can be proved by showing that SEA velocity satisfies*

$$\begin{array}{l} \dot{r}(t) = \alpha(t)(d_p - d) : \forall t \in [t_{\text{td}}, t_{\text{b}}] \\ \dot{r}(t) \neq \alpha(t)(d_p - d) : \exists t \in\subset [t_{\text{b}}, t_{\text{lo}}] \end{array}. \tag{4.36}$$

for some $\alpha(t) > 0$. In this regard, substituting the choices of leg parameters given in (4.32) yields

$$\begin{aligned} \dot{r}(t) =& (d_p - d)\frac{m}{(mk_p - dd_p)\dot{z}_{\text{td}} - d_p m \ddot{z}_{\text{td}}} h(t) \\ \text{with } h(t) :=& \dot{z}_{\text{td}}\ddot{z} - \ddot{z}_{\text{td}}\dot{z}. \end{aligned} \tag{4.37}$$

Before proving the claim in (4.36), we will, first, show that the denominator is negative, unless the touchdown velocity is impractically close to zero. Employing the proof by contradiction, we start by supposing that the contrary is true as $(mk_p - dd_p)\dot{z}_{\text{td}} - d_p m\ddot{z}_{\text{td}} \geq 0$. Substituting $\ddot{z}_{\text{td}} = -g - \ddot{z}_{\text{td}} d_p/m$, this argument can be alternatively expressed as

$$(mk_p - dd_p + d_p^2)\dot{z}_{\text{td}} + d_p m g \geq 0 \tag{4.38}$$

Since $mk_p - dd_p + d_p^2 > mk_p - dd_p > 0$ by Remark 1, the argument in (4.38) requires

$$\dot{z}_{\text{td}} > \mathcal{H} := -\frac{mgd_p}{mk_p - dd_p + d_p^2}.$$

Differentiating $\mathcal{H}$ to find a lower bound, we obtain

$$\begin{array}{l} \dfrac{\partial \mathcal{H}}{\partial d} = -\dfrac{mgd_p^2}{(mk_p - dd_p + d_p^2)^2} < 0 \\ \dfrac{\partial \mathcal{H}}{\partial d_p} = -\dfrac{mg(mk_p - d_p^2)}{(mk_p - dd_p + d_p^2)^2} < 0 \end{array},$$

leading to

$$(d_{\max}, d_{p\max}) = \underset{(d,dp)}{\operatorname{argmin}}\, \mathcal{H}.$$

Substituting this result with $d_{p\max}$ and $d_{\max}$ given in Assumption 2 yields

$$\dot{z}_{\mathrm{td}} > \mathcal{H} \geq -0.4mg/\sqrt{k_p m}. \tag{4.39}$$

This lower bound is actually infeasible for robotic platforms. Consider, for example, the ATRIAS bipedal robot with $k_p = 6500N/m$ and $m = 60kg$ [46] requiring $\dot{z}_{\mathrm{td}} > -0.375m/s$ corresponding to infeasible apex heights $h < z_{\mathrm{td}} + 0.007m$ due to too small foot-to-ground clearance compared to ATRIAS' leg length of $1m$. Therefore, a contradiction with the initial assumption (4.38) is obtained, hence proving the negativity of the denominator

$$(mk_p - dd_p + d_p^2)\dot{z}_{\mathrm{td}} + d_p mg < 0. \tag{4.40}$$

This translates the statement (4.36) to an alternative argument for the proof as

$$h(t) = \dot{z}_{\mathrm{td}}\ddot{z}(t) - \ddot{z}_{\mathrm{td}}\dot{z}(t) \leq 0 : \forall t \in [t_{\mathrm{td}}, t_{\mathrm{b}}] \tag{4.41}$$

$$h(t) = \dot{z}_{\mathrm{td}}\ddot{z}(t) - \ddot{z}_{\mathrm{td}}\dot{z}(t) \geq 0 : \exists t \in [t_{\mathrm{b}}, t_{\mathrm{lo}}] \tag{4.42}$$

We will, first, prove (4.41). To this end, the proof is separately given for $\ddot{z}_{\mathrm{td}} \leq 0$ and $\ddot{z}_{\mathrm{td}} > 0$. Consider, first, $\ddot{z}_{\mathrm{td}} \leq 0$. In this case, the compression phase is composed of two subintervals $[t_{\mathrm{td}}, t_b] = [t_{\mathrm{td}}, t_{z0}] \cup (t_{z0}, t_b]$ with $\ddot{z}(t_{z0}) = 0$. As detailed in Proof of Prop.2, we have $\ddot{z}(t) < \ddot{z}(t_{z0})$ for $t < t_{z0}$ and $\ddot{z}(t) > \ddot{z}(t_{z0})$ for $t > t_{z0}$ in these intervals. In the first subinterval, we have $\dot{z}(t) < \dot{z}_{\mathrm{td}}$, which lets us prove the statement (4.41) by Prop.2 as

$$\dot{z}_{\mathrm{td}}\ddot{z}(t) - \ddot{z}_{\mathrm{td}}\dot{z}(t) < \dot{z}_{\mathrm{td}}(\ddot{z}(t) - \ddot{z}_{\mathrm{td}}) \leq 0 \; \forall t \in [t_{\mathrm{td}}, t_{z0}].$$

In the second subinterval, we have $\ddot{z}(t) > 0$ by definition, thus letting us again conclude the same result as

$$\dot{z}_{\mathrm{td}}\ddot{z}(t) - \ddot{z}_{\mathrm{td}}\dot{z}(t) < 0 \; \forall t \in (t_{z0}, t_b].$$

Consider, now, the remaining case $\ddot{z}_{\mathrm{td}} > 0$. As $\ddot{z}(t) > \ddot{z}_{\mathrm{td}}$ and $\dot{z}(t) > \dot{z}_{\mathrm{td}}$ in the compression by Prop.2, we can easily prove

$$\dot{z}_{\mathrm{td}}\ddot{z}(t) - \ddot{z}_{\mathrm{td}}\dot{z}(t) < \dot{z}_{\mathrm{td}}(\ddot{z}(t) - \ddot{z}_{\mathrm{td}}) < 0.$$

With this, the proof of the statement (4.41) is concluded.

Finally, we present the proof of the statement (4.42). To this end, consider, first, $\ddot{z}_{\mathrm{td}} \leq 0$. *To show the existence of* t *satisfying (4.42), it is sufficient to consider* $\ddot{z}(t_{z0}) = 0$ *with* $t_{z0} \in (t_b, t_{\mathrm{lo}}]$. *Using the fact* $\dot{z}(t_{z0}) > 0$, *we obtain the result that we seek for the proof as*

$$h(t_{z0}) = \dot{z}_{\mathrm{td}}\ddot{z}(t_{z0}) - \ddot{z}_{\mathrm{td}}\dot{z}(t_{z0}) = -\ddot{z}_{\mathrm{td}}\dot{z}(t_{z0}) > 0.$$

Before moving to the proof for the case $\ddot{z}_{\mathrm{td}} > 0$, *we want to make two observations that will be useful in the next Section. In this regard, observe that*

$$\begin{aligned} h(t) &< h(t_{z0}) : t_b < t < t_{z0} \\ h(t_1) &> h(t_2) : t_1 > t_2 \geq t_{z0} \end{aligned} \tag{4.43}$$

since the followings are true by Corol. 1

$$\begin{aligned} \ddot{z}(t) > \ddot{z}(t_{z0}) = 0 &\implies \dot{z}(t) < \dot{z}(t_{z0}) : t_b < t < t_{z0} \\ \ddot{z}(t_1) < \ddot{z}(t_2) < 0 &\implies 0 < \dot{z}(t_1) < \dot{z}(t_2) : t_1 > t_2 \geq t_{z0}. \end{aligned}$$

Consider, now, the remaining case $\ddot{z}_{\mathrm{td}} > 0$. *As opposed to the previous case, we have*

$$h(t_{z0}) = -\ddot{z}_{\mathrm{td}}\dot{z}(t_{z0}) < 0.$$

Furthermore, the facts $\ddot{z}(t) > \ddot{z}(t_{z0}) = 0$ *and* $\dot{z}(t) > 0$ *imply* $h(t) < 0 \ : \ t_b < t < t_{z0}$ *as well. Therefore, we investigate* $t_{\mathrm{lo}} \geq t > t_{z0}$ *as the only interval worth consideration for the proof. In this regard, observe, first, that* $h(t_1) > h(t_2) : t_1 > t_2 > t_{z0}$ *due to* $0 < \dot{z}(t_1) < \dot{z}(t_2)$ *and* $\ddot{z}(t_1) < \ddot{z}(t_2) < 0$. *This yields an important intermediate result*

$$h(t_{\mathrm{lo}}) = \max_t h(t), \tag{4.44}$$

which is in line with conclusions of (4.43) that hold for $\ddot{z} \leq 0$. *In this regard, plugging explicit expressions* $\ddot{z}_{\mathrm{lo}} = -g$, *and* $\ddot{z}_{\mathrm{td}} = -g - (d_p/m)\dot{z}_{\mathrm{td}}$ *into* $h(t_{\mathrm{lo}})$ *defines the necessary condition for the proof*

$$\dot{z}_{\mathrm{lo}} > \frac{g\dot{z}_{\mathrm{td}}}{-\ddot{z}_{\mathrm{td}}} = \frac{g\dot{z}_{\mathrm{td}}}{g + (d_p/m)\dot{z}_{\mathrm{td}}}.$$

As it is sufficient to show the existence of such $\dot{z}_{\mathrm{lo}}$, *consider an example case* $\ddot{z}_{\mathrm{td}} > g$ *and* $d = 0$, *leading to* $\dot{z}_{\mathrm{lo}} = -\dot{z}_{\mathrm{td}}$, *hence satisfying the inequality. With this example case proving the statement, we conclude the proof.* □

As articulated in the proof, the CVD policy eliminates the negative power of the SVD during compression by entirely confining the SEA velocities in that phase to either

$\dot{r}(t) \geq 0$ or $\dot{r}(t) \leq 0$ through the touchdown velocity constraint $\dot{r}_p(0) = 0$. In order to eliminate the remaining negative work, we can also enforce a liftoff velocity constraint on SEA trajectories with $\dot{r}_p(t_{\text{lo}}) = 0$. However, adding a new constraint requires a new control parameter. To this end, we propose to modulate $\boldsymbol{p}$ in a piecewise constant fashion as

$$\boldsymbol{p} = \begin{cases} [d_1, k_1, f_1], & \dot{z} \leq 0 \text{ (compr.)} \\ [d_2, k_2, f_2], & \dot{z} > 0 \text{ (decompr.)} \end{cases}, \tag{4.45}$$

corresponding to six dimensional parametrization of tunable control parameters. On the other hand, we should also ensure continuity of SEA trajectories when $\dot{z} = 0$ (i.e., bottom). All of these requirements can be enforced with three additional constraints in the form

$$\begin{bmatrix} \mathcal{R}(t_{\text{b}}^{+}) \\ \dot{r}_p(t_{\text{b}}^{+}) \\ \dot{r}_p(t_{\text{lo}}) \end{bmatrix} = \begin{bmatrix} \mathcal{R}(t_{\text{b}}^{-}) \\ \dot{r}_p(t_{\text{b}}^{-}) \\ 0 \end{bmatrix} \tag{4.46}$$

where superscripts $-$ and $+$ identify pre-bottom and post-bottom quantities, respectively. By combining these constraints with those in (4.46), we obtain a total of six equations which admit a solution to the six unknowns in $\boldsymbol{p}$ when $d_p \neq 0$. Fortunately, solutions given in (4.32) are still applicable to compression parameters f_1 and k_1 with $d = d_1$. For f_2 and k_2, solving the first and second rows in (4.46) yields

$$\begin{aligned} f_2 &= f_1 - (d_1 - d_2) k_p (z_{\text{b}} - z_{\text{td}})/d_p \\ k_2 &= k_1 + k_p (d_2 - d_1)/d_p \end{aligned} . \tag{4.47}$$

Finally, substituting these expressions into the third row, the solution to d_2 can be obtained as a function of compression parameters in the form

$$d_2 = \frac{P_1 + P_2}{(d_p \dot{z}_{\text{td}}(d - d_p) - m(d_p g + k_p \dot{z}_{\text{td}}))\dot{z}(t_{\text{lo}})} \tag{4.48}$$

with

$$\begin{aligned} P_1 &:= d_p \dot{z}_{\text{td}}(d - d_p)(f_2 - mg - k_2(z(t_{\text{lo}}) - z_{\text{td}})) \\ P_2 &:= (d \dot{z}_{\text{td}}(d_p^2 - k_p m) - d_p^2(mg + d_p \dot{z}_{\text{td}}))\dot{z}(t_{\text{lo}}) \end{aligned}$$

With these solutions, we obtain a new control policy called CVD+. It yields a more efficient instantiation of FSLIP than CVD. In particular, as illustrated in Fig. 4.3, smooth SEA trajectories under CVD+ policy completely eliminate the negative work by satisfying (4.20). This is stated more formally by the following proposition.

Proposition 4. *During stance, the SEA does zero negative work with*

$$P_{sea}^{\text{cvd+}}(t)(\Delta E)_{\text{sea}}^{\text{cvd+}} \geq 0 : \forall t \in [t_{\text{td}}, t_{\text{lo}}].$$

Proof. *The proof of this proposition requires to show that the existence of* $\alpha(t) \geq 0$ *for CVD+ policy such that*

$$\dot{r}(t) = \alpha(t)(d_p - d) : \forall t \in [t_{\text{td}}, t_{\text{lo}}].$$

Consider, first, the compression phase. Leg parameters enforced by CVD+ in this phase are actually identical to those of CVD policy. Therefore, Prop. 3 becomes applicable, automatically proving $\alpha(t) \geq 0$ *for the compression.*

Consider, now, the decompression phase in which SEA velocity takes the form

$$\dot{r}(t) = (d_p - d)\underbrace{\frac{m(h(t) + \tilde{h}(t))}{m(d_p g/\dot{z}_{\text{td}}) + mk_p - d_p(d - d_p)}}_{\alpha(t)} \tag{4.49}$$

with $h(t) := \dot{z}_{\text{td}}\ddot{z}(t) - \ddot{z}_{\text{td}}\dot{z}(t)$

$\tilde{h}(t) := \dot{z}(t)(k_p\dot{z}_{\text{td}} + d_p g)(d - d_2)/(d_p(d_p - d)).$

A policy with zero negative work can be obtained by enforcing

$$\alpha(t) > 0 \; \forall \; t \in [t_{\text{td}}, t_{\text{lo}}]. \tag{4.50}$$

In this regard, observe that the denominator in (4.49) and $h(t)$ *take the same form as in the Proof of Prop. 3, thus preserving the validity of observations (4.40), (4.41), and (4.42). Using the negativity of the denominator as one of these observations, (4.50) requires*

$$h(t) + \tilde{h}(t) \leq 0 \; \forall \; t \in [t_{\text{td}}, t_{\text{lo}}].$$

This can be enforced by ensuring

$$h(t_c) + \tilde{h}(t_c) := \max_{t_b \leq t \leq t_{\text{lo}}} \left[h(t) + \tilde{h}(t)\right] = 0. \tag{4.51}$$

In Proof of Prop. 3, we observed through (4.43) and (4.44) that $\max_t h(t) = h(t_{\text{lo}})$. *Consider, now,* $\tilde{h}(t)$. *In this regard, following infeasibility of (4.39)* $\dot{z}_{\text{td}} > -0.4mg/\sqrt{k_p m}$ *proved in Proof of Prop. 3, we, first, observe* $k_p\dot{z}_{\text{td}} + d_p g < 0$. *Furthermore, assuming* $\text{sgn}(d - d_2) = -\text{sgn}(d_p - d)$, *we obtain*

$$\max_{t_b \leq t \leq t_{\text{lo}}} \tilde{h}(t) = \tilde{h}(t_{z0}),$$

which implies that the overall minima t_c defined in (4.51) satisfies

$$t_{z0} < t < t_{\mathrm{lo}}.$$

In this regard, solving for d_2 to satisfy (4.51) yields

$$d_2 = \frac{P_1 + P_2}{(d_p \dot{z}_{\mathrm{td}}(d_1 - d_p) - m(d_p g + k_p \dot{z}_{\mathrm{td}}))\dot{z}(t_c)} \tag{4.52}$$

with $P_1 := d_p \dot{z}_{\mathrm{td}}(d - d_p)(f_2 - mg - k_2(z(t_c) - z_{\mathrm{td}}))$

$P_2 := (d\dot{z}_{\mathrm{td}}(d_p^2 - k_p m) - d_p^2(mg + d_p \dot{z}_{\mathrm{td}}))\dot{z}(t_c)$

This defines the exact form of the solution to decompression damping for efficient control with zero negative work. In this context, one can check that the CVD+ policy does indeed adopt the same form. However, it approximates (4.52) by assuming $t_c \approx t_{\mathrm{lo}}$, which is done for the sake of computational efficiency, hence avoiding to solve the maximization problem (4.51). Here, we avoid more details to justify this approximation because of space limitation. However, numerical results (see Fig. 4.3 for an individual example) show that the approximation $t_c \approx t_{\mathrm{lo}}$ is sufficiently accurate. □

4.4.4 Comparison with Alternative Approaches

In this subsection, we present a comparative study of different gait control strategies with regard to their energetic performance and control accuracy through single stride simulations. In particular, we consider five policies :

1. The CVD+ : See Sec. 4.4.3.

2. The SVD : See Sec. 4.4.2.

3. The variable stiffness (VS) : This policy was first implemented on Raibert's hoppers to regulate the running energy ([73, 58]). It is based on changing the stiffness at bottom. It was later used for control of quadruped running ([26]), 3D SLIP running ([16]), and SLIP walking ([100]).

4. The velocity modulated fixed thrust (VMFT) : Introduced by [78, 79], this strategy controls the hopping energy by driving the SEA to a particular displacement at a constant velocity.

5. The active energy removal (AER) : [91] proposed a clock-based sinuosidal actuation to control the energy. As reported in [5, 72], this policy was also implemented on a monopod SLIP-like robot.

Single-stride simulations were run for the RM with non-dimensional parameters covering typical ranges of relative stiffness $\kappa := k_p z_0/(mg) \in [10, 40]$ and of damping ratio $\xi_p := d_p/(2\sqrt{k_p m}) \in [0.01, 0.07]$. On the other hand, we impose limits on the actuator performance with non-dimensionalized stall torque and no-load speed, chosen by mirroring the constraints of the experimental platform in Sec. 4.5 as

$$\begin{aligned} \tilde{u}_{\max} &:= u_{\max}/(mg) = 30 \\ \dot{\tilde{\delta}}_{\max} &:= \dot{\delta}_{\max}/\sqrt{g z_0} = 0.4 \end{aligned},$$

corresponding to a torque-speed relation $\max(-\tilde{u}_{\max}, \tilde{u}_\omega(\dot{\tilde{\delta}})) \leq \tilde{u} \leq \min(\tilde{u}_{\max}, \tilde{u}_\omega(\dot{\tilde{\delta}}))$ with $\tilde{u}_\omega := \tilde{u}_{\max}(1 - \dot{\tilde{\delta}}/\dot{\tilde{\delta}}_{\max})$. The remaining platform and simulation parameters were chosen to span representative ranges with dimensionless actuator inertia and initial apex heights, $\mathcal{J}_a := J_a/m = 10$ and $\tilde{h}_0 := h_0/z_0 \in [1.02, 1.32]$, respectively, while considering height difference commands $\Delta\tilde{h} := \tilde{h}^\star - \tilde{h}_0 \in [-0.3, 0.3]$ within a single stride to measure control accuracies and actuator power consumptions, respectively, through percentage error

$$\mathrm{PE} := 100\left|\frac{\tilde{h}^\star - \tilde{h}_0}{\tilde{h}^\star}\right| \tag{4.53}$$

and energetic metrics of root-mean-square (RMS) and peak powers, as

$$\begin{aligned} \widetilde{P}_{\mathrm{RMS}} &:= \sqrt{\frac{1}{t_{\mathrm{lo}} - t_{\mathrm{td}}} \int_{t_{\mathrm{td}}}^{t_{\mathrm{lo}}} \tilde{u}(t)\dot{\tilde{\delta}}(t)\mathrm{d}t} \\ \widetilde{P}_{\max} &:= \max_{t_{\mathrm{td}} \leq t \leq t_{\mathrm{lo}}} \tilde{u}(t)\dot{\tilde{\delta}}(t) \end{aligned}. \tag{4.54}$$

In this regard, Fig. 4.4 shows average values for percentage errors and these SEA power metrics across different simulations as a function of commanded change in apex height under different policies. The CVD+ strategy was found to have the least power consumption while yielding the best accuracy with approximately 1% error. These findings motivate the experimental implementation and verification of the CVD+, presented in the next section.

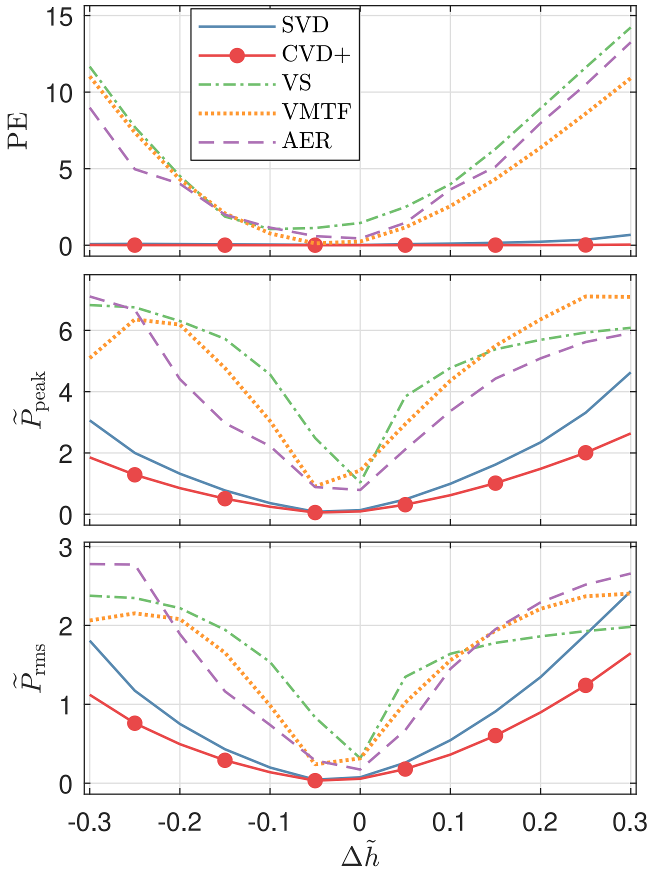

Figure 4.4: Dependence of percentage height tracking error (top) and RMS (middle) and peak (bottom) SEA power during stance on the commanded height difference for different policies.

4.5 Experimental Evaluation

In the following subsections, we present an experimental results of our approach implemented on a vertical hopping robot.

4.5.1 Hardware Platform

We built a hopping robot consisting of a vertically constrained mass, connected serially to a pair of helical linear springs through a motor and ball screw actuation unit, as depicted in Figure 4.5. Helical springs are axially constrained along the direction of the linear guide by means of a Sarrus Linkage (see [42]) in order to avoid spring buckling and to prevent the extension of springs beyond their rest lengths. Elastomers with sufficiently high damping are used on toe and link surfaces to soften contact transition impacts upon touchdown and activation of the mechanical stop at liftoff.

The actuation unit consists of a Maxon EC40 393025 170 W brushless DC motor and an NSK FA series PSS100 ball screw with 5 mm lead. The motor is controlled with a Maxon EPOS2 70/10 motor driver, capable of driving the motor with an intermittent force of 1450 N and a no-load speed of 0.8 m/s. As illustrated in Figure 4.2, we model the actuation unit as a force source u, with a counteracting friction f_a of the screw, a reflected inertia $J \approx 36kg$ of the motor and a point mass $m_a = 1kg$ of the nut in series between the body mass $m_b = 3.8kg$ and the spring with rest length $l_0 = 0.25m$, stiffness $k_p = 6000N/m$, and damping $d_p = 5Ns/m$. The robot has a point foot with mass $m_t = 0.7kg$ made from elastomer rubber filled with hot-melt adhesive. The entire system is restricted vertically by a linear guide rail with frictional interface.

The robot is equipped with two encoders to directly measure the vertical position z_b of the body and the relative SEA displacement δ. We also have a limit switch detecting the ground contact. Sensor outputs are read by a Texas Instruments ARM-based TM4C123G digital signal processor acting as a bridge and sent to the main control computer at 1 kHz via RS-485. The main controller communicates with the motor driver over a CAN bus connection at 1 kHz. The control loop is closed on the MATLAB Simulink Real-Time Operating System.

4.5.2 Model and Controller Extensions

In this subsection, we describe minor extensions to the models and the embedding controllers with the objective of further increasing the prediction accuracy.

4.5.2.1 Model Extensions

First, we extend all models to include the toe mass m_t and a viscous friction d_g as a simplified model of rail-guide friction. For the FSLIP model, this translates to new

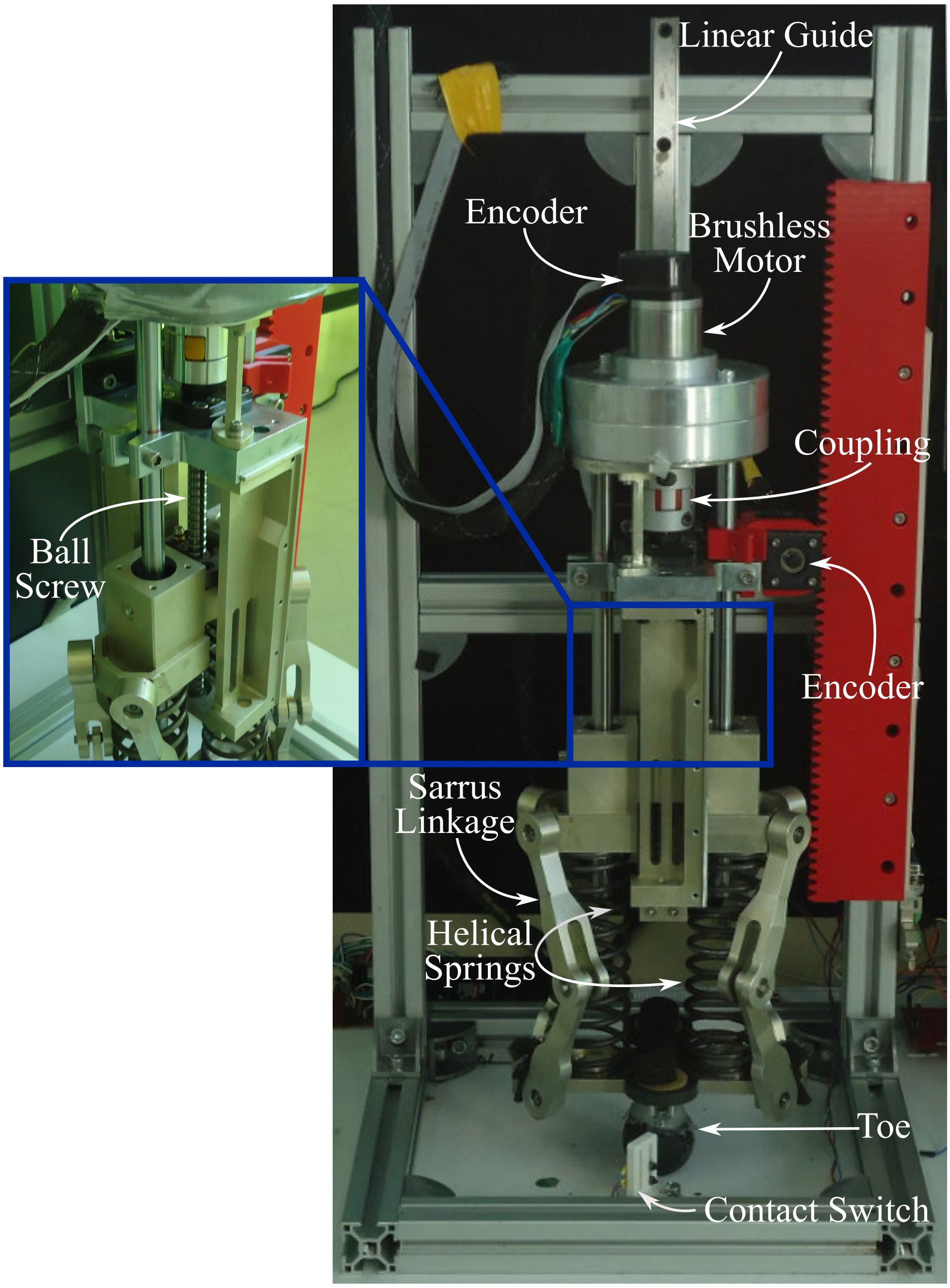

Figure 4.5: Our robot is a 5.5 kg vertical hopper with series elastic actuator consisting of a motor and ball screw.

forms for stance and flight dynamics, respectively, as

$$\ddot{z} = -\frac{k}{m}(z - z_{\mathrm{td}}) - \frac{d + d_g}{m}\dot{z} + \frac{f}{m} - g \tag{4.55}$$

$$\ddot{z} = -\frac{d_g}{m + m_t}\dot{z} - g. \tag{4.56}$$

For the IM and RM, similar extensions are also incorporated. On the other hand, liftoff events are, now, accompanied by an inelastic collision between the toe and leg structure, after which both masses end up moving with the same velocity. This can be captured by a collision map, corresponding to a discontinuity in the velocity with

$$\dot{z}_{\mathrm{lo}}^{+} = \frac{m}{m + m_t}\dot{z}_{\mathrm{lo}}^{-}. \tag{4.57}$$

These extensions alter the apex-to-apex return map of FSLIP, which we use to solve equations (4.31) and (4.46) defining the CVD+ policy. As derived below, the return map still admits an analytical solution, thus enabling real-time computation of the deadbeat controller which we implement via the MATLAB function *fzero*. Furthermore, we add the toe mass m_t and the damping d_g into the IM and RM to preserve the consistency among models.

The apex return map $\hat{h}_{i+1} = \mathcal{R}(h_i, \boldsymbol{p})$, yielding the predicted apex $\hat{h}_{i+1}$ for a given initial apex h_i and model parameters $\boldsymbol{p}$, can be computed as the composition of individual maps for flight and stance phases, which can be obtained from solutions to (4.56) and (4.55), respectively. Consequently, the apex return map can be decomposed as

$$\hat{h}_{i+1} := \left(R_a \circ R_{\mathrm{lo}} \circ R_s \circ R_d\right)(h_i)$$

combining the descent map R_d, the stance map R_s, the instantaneous liftoff map R_{lo} given in (4.57), and the ascent map R_a.

Flight dynamics (4.56), commonly defining the descent and ascent maps, admit the solution

$$z(t) = z_0 + \left(\dot{z}_0 + \frac{(m + m_t)^2 g}{d_g^2}\right)\left[1 - \exp\left(\frac{-d_g t}{m + m_t}\right)\right] - \frac{(m + m_t) g}{d_g} t$$

where z_0 and $\dot{z}_0$ denote the initial position and velocity, respectively. Evaluating this solution at the time of apex $t = t_a$ starting from initial conditions $(z_0, \dot{z}_0) = (z_{\mathrm{lo}}, \dot{z}_{\mathrm{lo}})$ taken at the liftoff $t = t_{\mathrm{lo}}$ gives the ascent map R_a. In this regard, solving $\dot{z}(t) = 0$ for t yields

$$t_a = \frac{m + m_t}{d_g} \ln\left[1 + \frac{d_g \dot{z}_{\mathrm{lo}}}{m + m_t}\right].$$

Similarly, we evaluate this solution at the time of touchdown $t = t_{\mathrm{td}}$ defined relative to the time of apex $t = 0$ with initial conditions $(z_0, \dot{z}_0) = (h_i, 0)$. However, as opposed to the apex equation $\dot{z}(t) = 0$, the touchdown equation (4.3) does not admit analytical solutions, hence we adopt the perturbation-based approach presented in Chapter 3 to approximately solve t_{td}.

Stance map R_s, on the other hand, can be obtained by evaluating (4.23), solution to dynamics (4.1), at the liftoff time $t = t_{\mathrm{lo}}$ which can be found by solving the condition (4.4) for t. Similar to the touchdown, this equation is again transcendental, thus admitting only approximate solutions, for which we again employ the perturbation-based approach.

4.5.2.2 Controller Augmentation

The feedback linearization (FL) controller embedding IM into RM is modified to take discrepancies between the RM and the actual platform into account, since PID-based controllers including FL can only perform well in the absence of disturbances and uncertainties. [114] reports experimental results aligning with this argument for an SEA including stick-slip effects in a screw-drive. In this context, disturbance observer (DOB)-based SEA controllers are recently demonstrated to provide excellent tracking and robustness by various works [61, 62, 76, 90, 75]. In order to benefit from those features, we employ a DOB in conjunction with the FL controller, defining the motor torque as

$$u = u_{\mathrm{dob}} + u_{\mathrm{ff}} + u_{\mathrm{fb}}.$$

with u_{dob} denoting the control signal generated by the DOB. This enforces the convergence of actual dynamics to the nominal model (4.13), hence helping FL achieve stability and the desired transient response. Details of the DOB-based controller design are given below.

Design of a DOB begins with the formulation of uncertainties and disturbances. In this regard, actual actuator dynamics after linearization can be modeled as a multiplicative perturbation to nominal dynamics (4.16) in the form

$$P(s) = P_n(s)(1 + \Delta(s)) \tag{4.58}$$

with transfer function of nominal dynamics $P_n(s) = 1/(J_a s^2)$, $P(s)$ actual dynamics, and $\Delta(s)$ unmodeled dynamics and lumped uncertainties. As illustrated in Fig. 4.6, the DOB feeds back the deviation between the actual control input u_{fb} and its estimate based on measured position and $P_n^{-1}(s)$ through a filter $Q(s)$. In particular, exogenous input-output relations can be defined as

$$\begin{aligned} u_{\text{dob}} &= \Upsilon(s)Q(s) - \delta(s)Q(s)/P_n(s) \\ \Upsilon &= u_{\text{fb}}(s) + u_{\text{dob}}(s) \\ \delta(s) &= (\Upsilon(s) + \zeta(s))\,/P(s) \end{aligned} \quad . \tag{4.59}$$

Solving for the actuator output yields

$$\delta(s) = G_u(s)u_{fb}(s) + G_\xi(s)\xi(s)$$

with $G_u(s) = \dfrac{P(s)P_n(s)}{P_n(s) + Q(s)(P(s) - P_n(s))}$

$G_\xi(s) = \dfrac{P(s)P_n(s)(1 - Q(s))}{P_n(s) + Q(s)(P(s) - P_n(s))}$.

For satisfactory performance, Q-filter of the DOB can be chosen as a low-pass filter since it leads to $G_u(s) \approx P_n(s)$ and $G_\xi(s) \approx 0$ at frequencies below its cut-off frequency, where $Q(s) \approx 1$. On the other hand, at frequencies above cut-off, the performance is compromised with $G_u(s) \neq P_n(s)$ and $G_\xi(s) \neq 0$ since $Q(s) \approx 0$. Even though this suggests increasing the Q filter's cut-off frequency for better performance, it is bounded above because of robustness and stability specifications as explained by [115]. This limitation can be formulated by the robust stability criterion (see [24] for details) of the inner loop formed by the DOB, i.e.,

$$\left\| \bar{S}_n(jw)\Delta(jw) \right\|_\infty \leq 1 \tag{4.60}$$

where $\bar{S}_n(jw)$ denotes the nominal complementary sensitivity function, defined as

$$\begin{aligned} \bar{S}_n(jw) &= \bar{S}(jw)\Big|_{P(jw)=P_n(jw)} \\ &= \frac{Q(jw)P(jw)}{P_n(jw) + Q(jw)(P(jw) - P_n(jw))}\Big|_{P(jw)=P_n(jw)} \\ &= Q(jw). \end{aligned}$$

In line with the literature (e.g., [54]), we choose a third-order binomial filter structure of the form

$$Q(s) = \frac{3\tau s + 1}{(\tau s + 1)^3}, \tag{4.61}$$

which has the time constant τ, to check the robust stability condition (4.60). After investigating the characteristics of lumped uncertainties based on experimental data, filter cut-off frequency was chosen as $50Hz$.

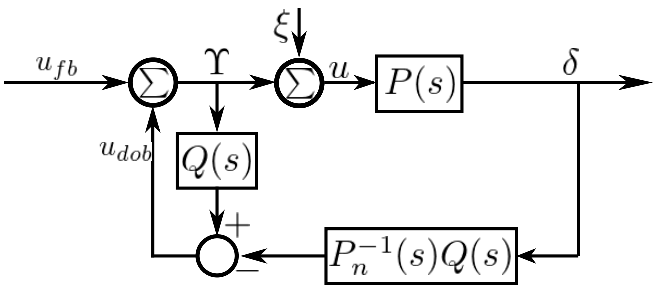

Figure 4.6: Block diagram of feedback linearized system augmented with disturbance observer.

4.5.3 Experimental Results

We performed comprehensive experiments to assess the accuracy of our extended models and performance of our embedding approach in conjunction with the target model FSLIP under CVD+ policy. In particular, our experiments were designed to cover 15 different initial conditions with $\bar{h}_0 \in [1.05, 1.35]$, each followed by 20 different apex height difference commands with $\Delta\bar{h} \in [-0.3, +0.3]$. Each experiment was repeated three times to ensure statistical reliability of the dataset. Figure 4.7 illustrates an example test run, showing trajectories of the actual robot (solid blue) and the TM (dashed maroon). In the following subsections, after showing the accuracy of our simulations based on the robot model (RM) compared to the experimental data, we present an evaluation of our control approach.

4.5.3.1 Model Accuracy

As an initial evaluation, we compare the experimental data with numerical results obtained through simulations of the robot model (RM) tailored to represent the hardware platform using parameter values identified via experiments. This evaluation is important to understand to what extent our simulation and modeling framework can accurately represent the real-world dynamics. In this regard, we conducted single-

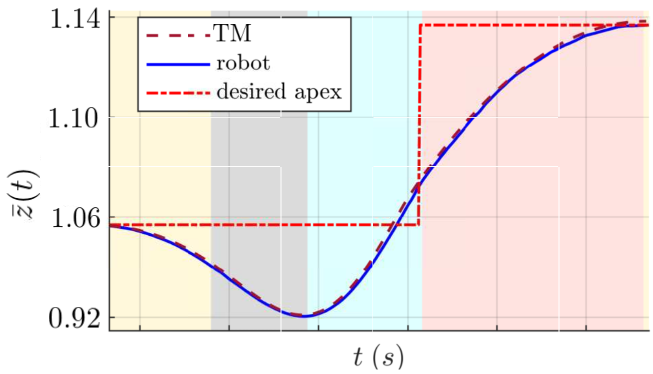

Figure 4.7: Single step trajectories of target model (TM - dashed maroon) and physical robot (RM - solid blue) for a change in desired apex height (dash-dotted red).

step simulations of the RM with same initial conditions h_0 and tunable parameters $\mathbf{p}$ used in experiments.

First, we measure the predictive performance of the simulated return map

$$\hat{h}_1 = \mathcal{R}_{\text{RM}}(h_0, \mathbf{p})$$

in terms of the error

$$E_{\text{sim}} := 100\frac{|h_1 - \hat{h}_1|}{h_1}$$

where h_1 denotes the actual apex at the end of the step, and the hat variable denotes the prediction. In this regard, we find out that the RM is an accurate predictor of physical implementation with $\%1$ and $<\%2$ mean and maximum errors, respectively, as shown by Fig. 4.8 illustrating the prediction error E_{sim} averaged across different initial conditions as a function of nondimensional commanded change in apex height $\Delta\tilde{h}$. As an additional criteria, we compare the power consumption of SEA in simulations to those in experiments. To this end, Fig. 4.9 illustrates the existence of close-correspondence in terms of nondimensional RMS and peak power ratings, $\tilde{P}_{\text{RMS}}$ and $\tilde{P}_{\text{max}}$, respectively, averaged across different initial conditions as a function of commanded height change.

Having shown that simulations based on RM are highly accurate with regard to both apex-to-apex prediction error and energetic characteristics, we can fairly expect that the comparative analysis of controllers presented in Fig. 4.4 will translate to the hardware in a similar fashion. In other words, we expect to achieve a similar control accuracy and energetic performance with the implementation of CVD+ policy on the robot, which also suggests that the relative performance of policies do not change on the hardware given the tiny discrepancy between the simulations and experiments illustrated in Fig. 4.8.

4.5.3.2 Control Performance

In order to evaluate our control approach, we measure the control accuracy with PE defined in (4.53) and energetic performance with normalized RMS and peak power ratings defined in (4.54). In this regard, Figure 4.10 shows average values of these performance metrics across three repetitions of experiments by a surface depicted as a heatmap in two dimensional space spanned by $\bar{h}_0$ and $\bar{h}^\star := \bar{h}_0 + \Delta\bar{h}$. The illustrated data show that our control approach provides highly accurate control with less than %2.5 PE in the entire workspace while demanding reasonable amount of energy input.As summarized by important statistical figures given in Table 4.1, the proposed control strategy overall provides $<$ %1 PE, 0.34 $\tilde{P}_{\mathrm{RMS}}$ and 1.2 $\tilde{P}_{\mathrm{peak}}$ on average with standard deviations well below $\%1$, 0.5, and 2, respectively, hence demonstrating consistent performance across the entire workspace. On the other hand, we observe a

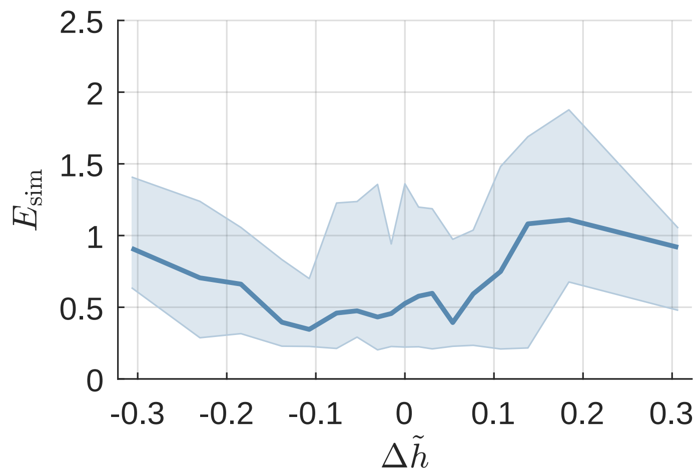

Figure 4.8: Prediction error of RM simulations compared to the physical implementation. Solid blue line corresponds to the mean error, and the shaded area is defined by the minimum and maximum error values, thus representing the entire set of experiments.

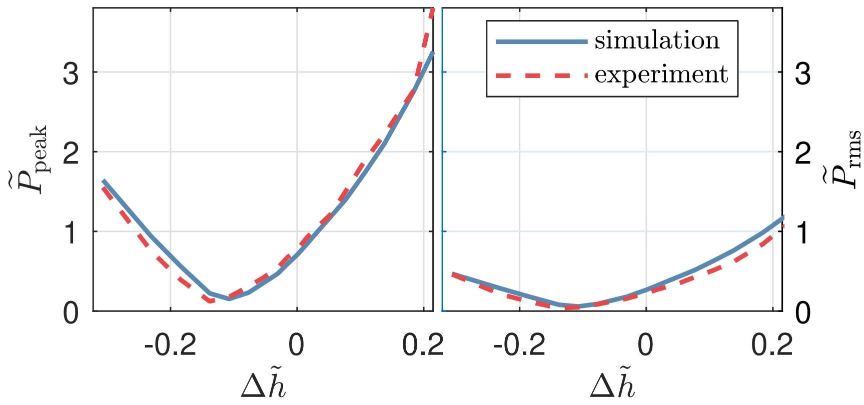

Figure 4.9: Nondimensional peak (left) and RMS (right) power consumption of RM simulations (solid blue) and experiments (dashed red) in a single step for various commanded changes in apex height.

close-correspondence between PE and power consumption from Figure 4.10 such that the PE is higher in the upper left and lower right regions where the power consumption is also increased. This can actually be explained by the fact that poor tracking of SEA trajectories in those regions lead to increase in PE. In this context, defining a nondimensional variable

$$E_\delta := \left| \frac{\int_{t_{\text{td}}}^{t_{\text{lo}}} \delta_d(t) - \delta(t)\mathrm{d}t}{(t_{\text{lo}} - t_{\text{td}}) \max\limits_{t_{\text{td}} \leq t \leq t_{\text{lo}}} \delta_d(t)} \right|$$

to quantify the overall SEA tracking error, experimental data illustrated in Fig. 4.11 provide empirical evidence for this argument by displaying the positive correlation between PE and tracking performance. This also shows the importance of planning feasible SEA trajectories for satisfactory control performance, which we do through the CVD+ policy.

Finally, we verify the main theoretical property of CVD+ policy, which is that only positive work is performed as stated in Prop. 4. To this end, as defined by [1], we consider two efficiency metrics to represent how much of the work at the output of the SEA and the motor is positive with

$$\eta_{\text{sea}} := \frac{|(\Delta E)_{\text{sea}}|}{(\Delta \mathcal{E})_{\text{sea}}}$$

$$\eta_{\text{motor}} := \frac{|(\Delta E)_{\text{sea}}|}{(\Delta \mathcal{E})_{\text{motor}}}$$

where $(\Delta E)_{\text{sea}}$ represents the net SEA work transmitted to the system as defined in (4.19), $(\Delta \mathcal{E})_{\text{sea}} := \int_{t_{\text{td}}}^{t_{\text{lo}}} |P_{\text{sea}}(t)|\mathrm{d}t$ denotes the total work generated by the SEA,

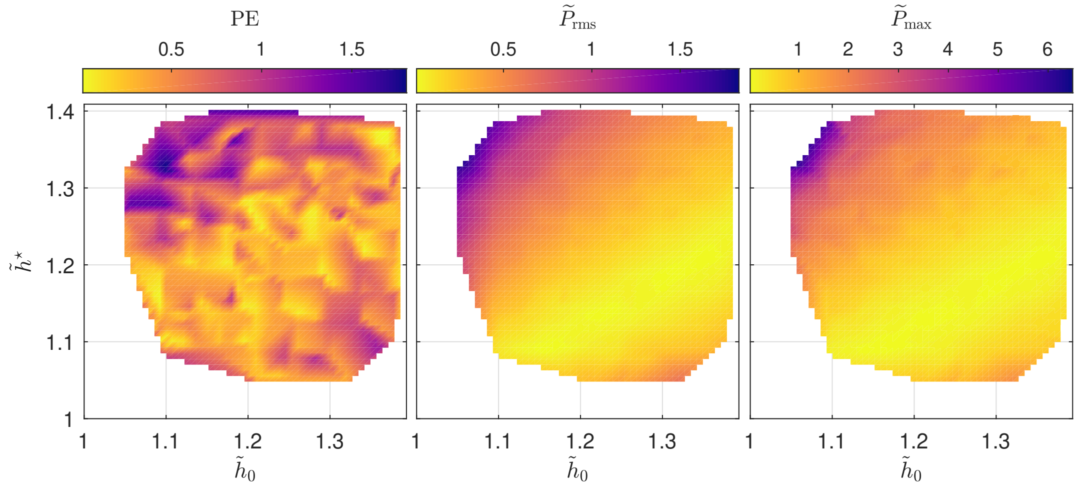

Figure 4.10: Dependence of percentage control error (left), RMS power consumption (middle), and peak power consumption (right) as a function of initial and desired apex heights.

and $(\Delta\mathcal{E})_{\text{motor}} := \int_{t_{\text{td}}}^{t_{\text{lo}}} |\dot{\delta}(t)u(t)|\mathrm{d}t$ denotes the total work delivered by the motor. In this regard, measuring the efficiency of our approach with these metrics averaged across different initial conditions as a function commanded height change, Fig. 4.12 illustrates that the SEA does only positive work with $\eta_{\text{sea}} \approx 1$ as expected, whereas the motor output is not equally efficient such that significant portion of its energy is expended to move the reflected motor inertia, which is nearly $J_a \approx 7.5(m_b + m_a)$ for our platform. Therefore, the overall efficiency is largely determined by the mechanical design of the transmission.

Table 4.1: Mean (μ), standard deviation (σ), and maximum ($\max$) values for percentage control accuracy as well as peak and RMS power requirements across all experiments.

	PE	$\tilde{P}_{\text{RMS}}$	$\tilde{P}_{\max}$
μ	0.62	0.34	1.19
σ	0.38	0.32	1.24
$\max$	1.72	1.87	6.61

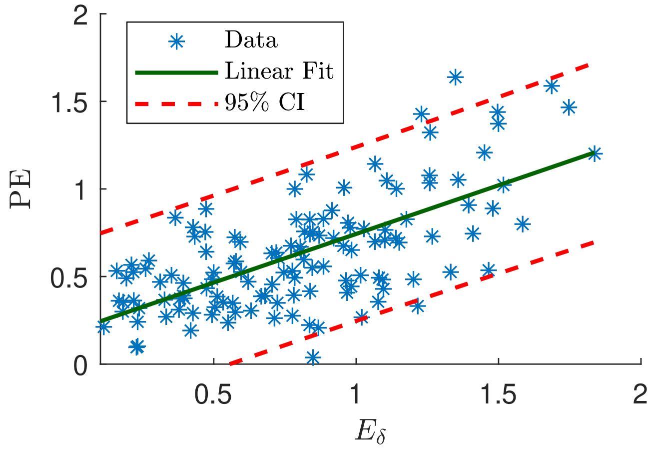

Figure 4.11: Dependence of PE on SEA tracking error where a linear model (green solid) can be fitted to the data (blue star) with 95% confidence intervals (dashed red) and $R^2 = 0.56$.

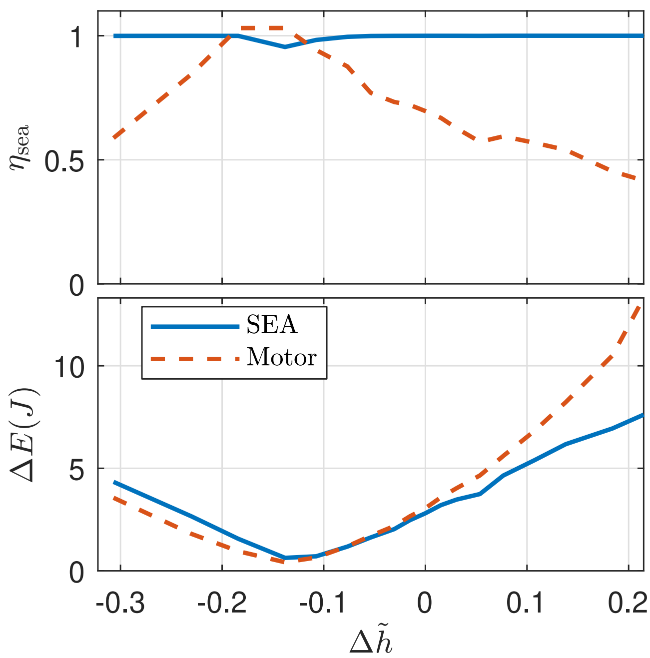

Figure 4.12: Efficiency of SEA work as a function commanded height change.

4.6 Conclusion

In this chapter, we have presented an experimental evaluation of a new damping-based gait control strategy which acts on the FSLIP model introduced in Chapter 3 by extending the well-known SLIP model. The new control strategy called CVD+ is based on tuning leg damping in conjuction with simultaneous modulation of spring stiffness and constant forcing to provide smooth actuator trajectories. After presenting a novel set of embedding controllers accurately realizing FSLIP as a target model on series-elastically actuated (SEA) platforms, we also prove that the CVD+ requires zero negative work. In order to measure the performance of this new strategy, we conduct simulations and find out that the CVD+ offers better control accuracy with smaller power requirements in comparison to many other strategies from the literature. Finally, we implement our control approach on a vertically hopping robot with SEA. The experiments provide empirical evidence in agreement with our theoretical results, thus qualifying our control approach and the CVD+ policy as an effective gait control strategy. Finally, as shown by the decoupling of locomotory degrees-of-freedom (DoFs) evidenced in [83] and [23], we hope that our results will translate to planar running which we study in the next chapter.

CHAPTER 5

EXPERIMENTAL EVALUATION OF PLANAR SPRING-MASS RUNNING THROUGH VIRTUAL LEG DAMPING

In Chapter 4, we experimentally verified the gait control policy CVD+ on a vertical hopping robot. In particular, we showed that theoretical advantages of CVD+ policy acting on the simple model FSLIP translate to more complex series-elastically actuated hardware platforms for the control of hopping energy. In this chapter, we take a step forward and implement our controllers on ATRIAS biped, which is a humanoid robot. Finally, we also report some preliminary experimental results.

5.1 Introduction

Simplified models of locomotion are widely used in robotics since they are intuitively simple and supported by biomechanical data/evidence, and being able to provide a natural stabilizing response to disturbances. In this context, the spring-loaded inverted pendulum (SLIP) model was proposed as a representative and general model of running [12] for natural runners that differ in the number of legs, leg morphology, and posture [27]. Capturing the underlying dynamics of running [30], SLIP also serves as a simple target model for robotic running and hopping [116, 21, 67, 22] since it admits extremely robust and stable running in the presence of ground height disturbances [118].

Despite these theoretical advantages of the SLIP model, it is difficult to transfer the resulting running behavior to humanoids having many additional degrees of freedom (DoFs), including a floating-base that acts like an inverted pendulum which is hard to stabilize. These additional DoFs are uncontrolled on robots with point feet, since external moments cannot be created due to the point contact and since external forces are usually reserved for tracking center of mass trajectories defined by the SLIP. This underactuation and energetic discrepancies between the model and the robot were previously associated with inaccuracy in SLIP-like running on hardware [68]. Notwithstanding the accurate realization of SLIP trajectories on the robot, uncontrolled trunk dynamics are often unstable, thus leading to a failure. On the other hand, imperfections in the mechanical system of the robot and desired changes in the running energy are not captured by the SLIP model, often requiring an additional layer of energy controller leading to deviations from the target model. In the literature, there are two approaches to solve these problems: i) Optimization-based planning of COM trajectories, which includes the desired change in locomotion energy while naturally stabilizing trunk dynamics instead of relying on simple models like SLIP [105, 14]. ii) Using more detailed simple models with trunk and non-conservative elements instead of an energetically conservative point mass body [6, 65, 11, 69]. The former provides a model-free solution using numerical optimization techniques for a set of initial conditions, thus requiring to run these computationally expensive algorithms at each step. Unfortunately, this is not easily scalable to robots with more DoFs, thus restricting the practicality of the approach to some extent. As an example, the interested reader can refer to CPU time results of a computationally improved version of a hybrid zero dynamics approach for which optimization of a single gait was reported ranging from 2 seconds to 40 seconds depending on the robot's complexity in [41]. On the other hand, the latter approach seeks more expressive simple mechanical models like the FSLIP model compared to the simplest SLIP model, hence being a model-based control approach. In this chapter, adopting this approach, we report our efforts towards transferring running behavior defined by an extension of the FSLIP model with a trunk under CVD+ policy. In particular, we extend the FSLIP model by incorporating a trunk and a hip torque reflex defined by the virtual-pivot pendulum based control [102] to stabilize the trunk.

In this context, the organization of this chapter is as follows : Section 5.2 describes both the hardware robotic bipedal platform and the conceptual FSLIP model extended with a trunk. Section 5.3 defines our multi-layered control architecture and describes details of each layer in order to transfer running gait defined by the conceptual model.

Figure 5.1: Carnegie Mellon University's copy of ATRIAS bipedal robot designed and built by Dynamic Robotics Laboratory at Oregon State University [46].

Section 5.4 presents the results of preliminary experiments conducted on a human-scale bipedal robot ATRIAS with the implementation of the described control approach. Finally, Section 5.5 concludes this chapter.

5.2 Models

5.2.1 Hardware Platform : ATRIAS Bipedal Robot

In this section, we consider dynamics of the ATRIAS (Assume The Robot Is A Sphere) bipedal robot, whose photo is given in Figure 5.1. The robot has a trunk and two legs with point feet. In particular, ATRIAS is a human-scale robot with 68 kg total mass concentrated about the trunk and two very light legs, each of which is about 2.5 kg and has a nominal length of 1 m. In our work, the robot was constrained to sagittal plane with a boom as shown by the photograph in Figure 5.2.

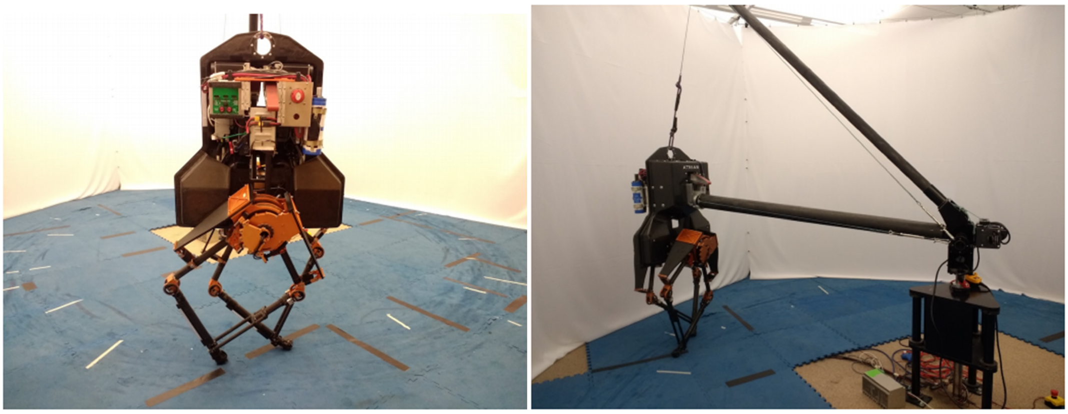

Figure 5.2: The robot is constrained to sagittal plane with a boom.

The use of boom effectively reduces the configuration space of the robot's floating base to two dimensions, admitting a planar model illustrated in Figure 5.3. The trunk has two translational degrees-of-freedom (DoF) and one rotational DoF, whereas each leg has two series-elastically actuated (SEA) joints. In this regard, we employ the floating base formulation to model the robot. The floating base formulation defines a general framework to model a system of rigid bodies that are not fixed to the world. In this framework, for the planar model of our robot whose configuration can be represented by generalized coordinates $q = \begin{bmatrix} q_b^T & q_l^T \end{bmatrix}^T \in \mathbb{R}^7$ consisting of floating-base coordinates $q_b \in \mathrm{SE}(2)$ and leg joint coordinates $q_l \in \mathbb{R}^4$, dynamics take the standard form

$$M(q)\ddot{q} + C(q, \dot{q})\dot{q} + G(q) = S^T\tau + J_f^T(q)\lambda \tag{5.1}$$

where $M(q)$ denotes the mass matrix, $C(q, \dot{q})$ the coriolis matrix, $G(q)$ the vector of gravitational forces, $S = [0_{4\times3} \quad I_{4\times4}]$ the selection matrix mapping joint torques τ produced by SEAs to generalized coordinates q, and the Jacobian J_f of contact constraints mapping constraint forces λ to joint space spanned by q.

During the stance phase of a stride, one of these limbs is in contact with the ground, while the other one is swung forward to prepare for the next stride. In the sequel, we will refer to them as the support leg and as the swing leg, respectively. Because of the contact with the ground during stance, contact forces are active (i.e., $\lambda \neq 0$) with the constraint Jacobian J_f defined as the Jacobian of the support leg's foot location $r_f(q) \in \mathbb{R}^2$ with $J_f = \partial r_f(q)/\partial q$. Furthermore, it is known that contact forces are

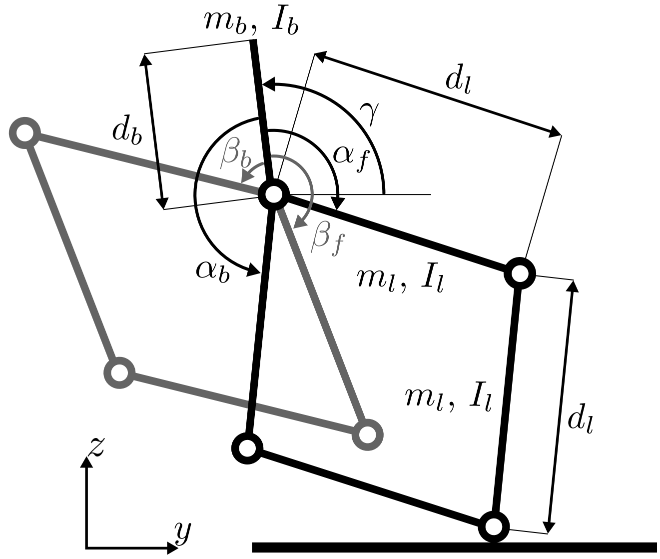

Figure 5.3: Planar model of ATRIAS robot.

completely determined by the joint torques during stance because of the constraint that the foot is stationary with

$$\begin{aligned} \dot{r}_f &= J_f(q)\dot{q} = 0 \\ \ddot{r}_f &= \dot{J}_f(q)\dot{q} + J_f(q)\ddot{q} = 0. \end{aligned} \tag{5.2}$$

To formulate the relation between contact forces λ and joint torques τ, we substitute the joint acceleration $\ddot{q}$ solved from (5.1) into (5.2) and obtain

$$\lambda = \left(J_f M^{-1} J_f\right)^{-1} \left(J_f M^{-1}(C\dot{q} + G) - J_f M^{-1} S^T \tau - \dot{J}_f \dot{q}\right). \tag{5.3}$$

On the other hand, during flight, both legs are swinging. Hence, contact forces are not active, becoming

$$\lambda = 0. \tag{5.4}$$

Under these contact forces, hybrid constrained dynamics take the common form

$$M\ddot{q} + \tilde{C}\dot{q} + \tilde{G} = \tilde{S}\tau \tag{5.5}$$

with

$$\tilde{C} := \begin{cases} \left(I - J_f^T (J_f M^{-1} J_f)^{-1} J_f M^{-1}\right) C + J_f^T (J_f M^{-1} J_f^T) \dot{J}_f & \text{during stance} \\ C & \text{during flight} \end{cases}$$

$$\tilde{G} := \begin{cases} \left(I - J_f^T (J_f M^{-1} J_f^T)^{-1} J_f M^{-1}\right) G & \text{during stance} \\ G & \text{during flight} \end{cases} \quad .$$

$$\tilde{S} := \begin{cases} \left(I - J_f^T (J_f M^{-1} J_f^T)^{-1} J_f M^{-1}\right) S^T & \text{during stance} \\ S^T & \text{during flight} \end{cases}$$

Even though Equations (5.3) and (5.4) show that contact forces are indeed specified by the mode of contact and joint torques, these forces become uncontrolled instantaneously at contact transitions. In particular, when a swing leg hits the ground, an impact happens leading to a change in states. To compute the effect of this impact on dynamics, we assume that collisions are perfectly plastic resulting in impulsive contact forces applied at the support foot y_f. In this context, following the methodology in [37], the impact map can be written as an affine function

$$\begin{bmatrix} q^+ \\ \dot{q}^+ \end{bmatrix} = \begin{bmatrix} I_{n\times n} & 0_{n\times n} \\ 0_{n\times n} & D(q^-) \end{bmatrix} \begin{bmatrix} q^- \\ \dot{q}^- \end{bmatrix} \tag{5.6}$$

where $D(q)$ is the mapping between velocities prior to and posterior to the touchdown, denoted respectively with superscripts $^+$ and $^-$. In contrast to the touchdown, as the ground contact is lost, no impact occurs at the support leg's liftoff which marks the transition from stance to flight with zero crossing of the contact force $\lambda = 0$.

5.2.2 Target Spring-Mass Models

Even though the FSLIP model proposed in Chapter 3 can be accurately embedded into COM dynamics of the full robot model for a fully controllable running gait, it does not guarantee to stabilize the trunk orientation. Unfortunately, due to the fact that robots with point feet are underactuated, trunk stabilization cannot be independently handled without compromising task of embedding FSLIP behavior into COM, as opposed to what can be done on a robot with planar feet (e.g. [116]). In this regard, we consider the virtual pivot point pendulum based control (VPPC) introduced in [69] as an extension of the FSLIP model with a trunk and a prescribed hip torque action for postural stability. In this section, we present this extended model, which we call FSLIP-VPPC after a brief recapitulation of the FSLIP with a slightly different convention for dynamical modeling.

5.2.2.1 FSLIP Model

As shown in Figure 3.1 and Figure 4.2, the FSLIP model has a compliant leg consisting of a spring with stiffness k and rest length l_0, a damper d and a constant forcing f. When the model is in contact with the ground, which is the stance phase, dynamics take the form

$$\ddot{r}_{\text{FSLIP}} = \frac{r_{\text{FSLIP}} - r_{\text{foot}}}{m\|r_{\text{FSLIP}} - r_{\text{foot}}\|}F + \begin{bmatrix} 0 \\ -g \end{bmatrix}$$

with position $r_{\text{FSLIP}} \in \mathbb{R}^2$ of the mass m, position $r_{\text{foot}} \in \mathbb{R}^2$ of the foot, 2-norm distance operator $\|.\|$, gravity g, and leg force

$$F = -k\left(\|r_{\text{FSLIP}}\| - l_0\right) - d\left(\frac{\mathrm{d}}{\mathrm{d}t}\|r_{\text{FSLIP}}\|\right) - f. \tag{5.7}$$

The stance phase starts at touchdown event marked with

$$[0 \quad 1]\, r_{\text{foot}} = 0. \tag{5.8}$$

After the springy leg is compressed in the stance, the point mass bounces back, and even takes off when

$$F = 0, \tag{5.9}$$

starting the flight phase governed by ballistic dynamics

$$\ddot{r}_{\text{FSLIP}} = \Big[0, -g\Big]^T.$$

5.2.2.2 FSLIP-VPPC Model

Originally proposed as a simple model of upright human walking [69] and later adapted for running [103, 70], the trunk FSLIP model with virtual pendulum posture control (FSLIP-VPPC) illustrated in Fig. 5.4 has a finite-inertia body instead of a point-mass and applies not only forces along the compliant leg but also hip torques to stabilize the trunk. In particular, the hypothesis of [69] based on human data suggests that hip torques and leg forces are coordinated in such a way that corresponding GRF crosses a single point fixed to the trunk throughout the stance, hence leading to pitching motion like a damped pendulum suspended from a pivot at that point. Even though this model does not entirely capture the trunk dynamics of a robot, it is a more useful template than the pure SLIP model by accounting for the trunk inertia, which is a significant contributor to the postural stability for robots with point feet.

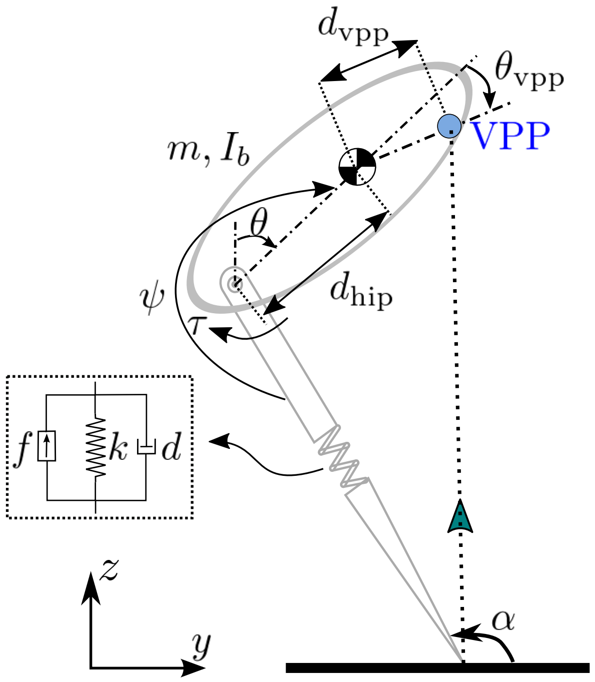

Figure 5.4: FSLIP-VPPC model redirects GRF toward the VP pivot point on the body.

With this extension, FSLIP-VPPC model can be described by three DoFs corresponding to generalized coordinate vector $q = [y, z, \theta]^T$ with COM positions (y, z) and trunk orientation θ. As shown in Fig. 5.4, compliant leg of the FSLIP-VPPC model is identical to that of the FSLIP, consisting of a spring, a damper, and a constant forcing. Thus, both models produce the same the leg force F given in (5.7) with $r_{\text{FSLIP}} = r_{\text{hip}}$ corresponding to the hip location

$$r_{\text{hip}} = r_{\text{VPPC}} - \left[d_{\text{hip}} \sin\theta, \quad d_{\text{hip}} \cos\theta\right]^T .$$

with $r_{\text{VPPC}} = [x, y]^T$.On the other hand, in order to redirect the GRF toward the virtual pendulum pivot, hip torque

$$\tau = F \, \|r_{\text{hip}}\| \, \frac{d \, sin(\psi) + d_{\text{vpp}} \, sin(\psi + \theta_{\text{vpp}})}{r - d \, cos(\psi) - d_{\text{vpp}} \, cos(\psi + \theta_{\text{vpp}})} \tag{5.10}$$

is applied between the trunk and the leg, which can be defined by the angle $\psi = \alpha + \theta + \pi/2$.

Combining leg force and hip torque, we express stance dynamics of the FSLIP-VPPC as

$$\ddot{q} = \text{diag}(1/m, 1/m, 1/I_b) \left(J_\psi \, \tau + J_r \, F - \begin{bmatrix} 0 & mg & 0 \end{bmatrix}^T \right)$$

with Jacobians $J_\psi := \partial\psi/\partial q$ and $J_r := \partial r_{\text{hip}}/\partial q$, whereas flight dynamics take the usual form $\ddot{q} = \begin{bmatrix} 0 & -g & 0 \end{bmatrix}^T$.

5.3 Control Approach

In previous chapters, we have adopted a dynamical model matching approach (aka task encoding [74]) in order to transfer the behavior to the robot by enforcing COM dynamics to take the form of a simple target model defining the behavior. For the ATRIAS, taking a different approach, we use state-space flow of the FSLIP-VPPC model as desired trajectories for the robot's COM and trunk orientation.

5.3.1 Control of the Target Behavior through Deadbeat Control of FSLIP-VPPC Model

The control of SLIP running is often formulated as a step-to-step regulation of apex states, which are defined as the system states at the vertically highest point (i.e., $\dot{z} = 0$) in flight. Since horizontal position is usually not a control objective in SLIP-like running, it is usually discarded from apex states. For example, the FSLIP model has a two-dimensional apex state vector with $\mathcal{Z} := \begin{bmatrix} z, & \dot{y} \end{bmatrix}^T$. On the other hand, for the FSLIP-VPPC model, apex state has two more dimensions compared to it as

$$\mathcal{Z} = \begin{bmatrix} z & \dot{y} & \theta & \dot{\theta} \end{bmatrix}^T . \tag{5.11}$$

In this regard, composition of flight and state dynamics defines the mapping between two consecutive apexes. This definition actually provides a useful abstraction of the

FSLIP-VPPC model by discretizing its hybrid dynamics with an apex-to-apex return map $\mathcal{Z}_{i+1} = R(\mathcal{Z}_i)$ from the i^{th} apex to the next.

In order to control this discrete system, we consider step-to-step regulation of tunable model parameters $\boldsymbol{p}$ as a control input and rewrite apex-to-apex return map as a function of these inputs with

$$Z_{i+1} = R(\mathcal{Z}_i, \boldsymbol{p}).$$

In Chapter 4, we introduced CVD+ policy, which modifies the leg damping d once-per-step to control the one dimensional apex state vector of vertical FSLIP model according to a deadbeat policy, thus corresponding to $\boldsymbol{p} = [d]$. Here, for the planar FSLIP-VPPC, we extend the CVD+ policy to a deadbeat control problem with four control inputs and four dimensional apex Z given in Equation (5.11). In particular, following [102], we employ the touchdown angle α_{td}, VP pivot angle θ_{vpp} and VP pivot distance d_{vpp} for this purpose. Therefore, a step-to-step deadbeat policy can be formulated as

$$\boldsymbol{p} := (\theta_{\mathrm{vpp}}, d_{\mathrm{vpp}}, d, \alpha_{\mathrm{td}}) = \arg\min \|Z^\star - R(\mathcal{Z}_i)\| \tag{5.12}$$

for a desired apex state $\mathcal{Z}^\star$ whose third and fourth components, are respectively chosen as $\theta^\star = \pi/2$ and $\dot{\theta}^\star = 0$ to enforce trunk stabilization. While seeking a solution to tunable parameter $\boldsymbol{p}$ with this problem, we fix remaining parameters leg spring and constant forcing according to CVD+ policy defined by Equations (4.45), (4.32), and (4.47). With this way, the FSLIP-VPPC model is completely defined, hence allowing us to compute desired COM trajectories $r_{\mathrm{VPPC}}(t)$ by forward simulation and desired foot placement targets with

$$\rho_{\mathrm{td}} = r_{\mathrm{foot}}(t_{\mathrm{td}}) - r_{\mathrm{hip}}(t_{\mathrm{td}}) = \begin{bmatrix} -l_0 \cos(\alpha_{\mathrm{td}}) & -l_0 \sin(\alpha_{\mathrm{td}}) \end{bmatrix}^T \tag{5.13}$$

for the robot.

5.3.2 Control of the Robot to Embed Target Behavior

The main objective of the robot's controller is to track the desired COM trajectories of the FSLIP-VPPC model while avoiding postural instability. To this end, During stance, this is done by indirectly controlling ground reaction forces (GRF) acting as external forces solely. In contrary to that, there are no external forces during flight, hence rendering the robot's COM and postural dynamics uncontrolled. Fortunately, robot's COM trajectory $r_{\text{COM}}(q) \in \mathbb{R}^2$ during flight match exactly to that of the FSLIP-VPPC model without any control since flight dynamics already satisfy

$$\ddot{r}_{\text{COM}} = \ddot{r}_{\text{VPPC}} = [0 \quad -g]^T \, . \tag{5.14}$$

Hence, with this approach, FSLIP-VPPC trajectories can be accurately tracked by the robot. Unfortunately, this is not sufficient for the successful transfer of the SLIP-like running to the robot, as the controller needs to 1) move the legs in a coordinated fashion during both flight and stance 2) constrain trunk orientation to an acceptable interval. In this context, we employ Khatib's task-space control framework [56], which is equivalent to input-output linearization, in order to track COM trajectories of FSLIP-VPPC model with inherent postural stability thanks to stabilizing virtual pivot point pendulum based hip action (5.10) and deadbeat controller (5.12).

Consider, a vector of tasks $w(q) \in \mathbb{R}^4$, which is a function of generalized positions. Substituting joint space dynamics into task accelerations

$$\ddot{w} = J_w(q)\ddot{q} + \dot{J}_w(q)\dot{q},$$

with Jacobian $J_w(q) = \partial w(q)/\partial q$, we obtain the task space dynamics as

$$\ddot{w} = J_w \, M^{-1} \left(\tilde{S}\tau - \tilde{C}\dot{q} - \tilde{G} \right) + \dot{J}_w \dot{q} \tag{5.15}$$

Thus, if a desired task trajectory $w_d(t) \in \mathbb{R}^4$ is given, an asymptotically stable tracking controller can be formulated as

$$\tau = \left(J_w M^{-1} S^T\right)^{-1} \left(\ddot{w}_d + K_d(\dot{w}_d - \dot{w}) + K_p(w_d - w) + J_w M^{-1}(\tilde{C}\dot{q} + \tilde{G}) - \dot{J}_w \dot{q} \right)$$

with controller gains $K_p > 0$ and $K_d > 0$. This framework is sufficiently flexible to define different tasks in flight and stance phases. Similar to [116] and [68], a state machine is employed to define and schedule these tasks depending on the mode of contact. To this end, the state machine categorizes the legs as primary and secondary. During stance, primary and secondary legs are chosen as support and swing legs, respectively. At the lift off, they are switched so that the next support leg is treated as the primary leg during flight. In this context, primary leg actuators are used to track

COM trajectories of FSLIP-VPPC during stance and to realize FSLIP-VPPC foot placement targets during flight. On the other hand, secondary leg basically mirrors the primary leg's motion in the horizontal direction while maintaining a safe ground clearance in the vertical direction as suggested by [83] to effectively prepare a swing leg to the next step without injecting much trunk disturbance. In order to realize these objectives, we explicitly define the task function as

$$w(q) = \begin{cases} [r_{\mathrm{COM}}(q);\ r_{\mathrm{F2}}(q) - r_{\mathrm{COM}}(q)] & \text{during stance} \\ \\ [r_{\mathrm{F1}}(q) - r_{\mathrm{COM}}(q);\ r_{\mathrm{F2}}(q) - r_{\mathrm{COM}}(q)] & \text{during flight} \end{cases}$$

with foot locations of the primary and secondary legs $r_{\mathrm{f1}}(q) \in \mathbb{R}^2$ and $r_{\mathrm{f2}}(q) \in \mathbb{R}^2$, respectively. Desired trajectory $w_d(t)$ corresponding to these tasks are defined as

$$w_d(t) = \begin{cases} \left[r^{\star}_{\mathrm{COM}}(t);\quad \tilde{\rho}^{\mathrm{td}}_{\mathrm{lo}}(t)\right] & \text{during stance} \\ \\ \left[\rho^{\mathrm{td}}_{\mathrm{lo}}(t);\quad \tilde{\rho}^{\mathrm{lo}}_{\mathrm{td}}(t)\right] & \text{during flight} \end{cases} \tag{5.16}$$

where $r^{\star}_{\mathrm{COM}}(t) = r_{\mathrm{VPPC}}(t)$ denotes the desired COM trajectory, chosen as the trajectory of the SLIP model, $\rho^{\mathrm{j}}_{\mathrm{i}}(t)$ is a smooth point-to-point trajectory that connects COM-to-foot position of the SLIP model at event i (i.e., ρ_i) to that at event j (i.e., ρ_j), and $\tilde{\rho}^{\mathrm{j}}_{\mathrm{i}}(t)$ is a smooth trajectory defined according to the same convention with ground clearance $\bar{z}_c \geq 0$ for leg retraction as $\tilde{\rho}^{\mathrm{lo}}_{\mathrm{td}}(t) = \rho^{\mathrm{lo}}_{\mathrm{td}}(t) + [0;\quad \bar{z}_c]$. Finally, note that, during implementation, we make a small correction to these desired trajectories at phase changes by planning a transitory trajectory from the initial conditions disturbed by contact collisions and other errors.

5.4 Preliminary Experimental Results and Discussion

Here, we present a demonstration of our preliminary experimental results with ATRIAS biped bouncing/running on level ground. In order to assess the single-step control accuracy of our approach, we commanded step changes to forward velocity as $\Delta\dot{y}^{\star} := \dot{y}^{\star}_{k+1} - \dot{y}^{\star}_{k} \in [-0.4, +0.4]$ at different baseline velocities $\dot{y}^{\star}_{k} \in [-1, +1] m/s$ while keeping the apex height constant at 1.05m, corresponding to 3.5cm ground clearance for nominal leg length at apex. As an example experiment, forward velocity trajectories of the robot is shown in Figure 5.5. In this regard, the control accuracy is measured with a percentage error defined as

$$\mathrm{PE} := 100\frac{\|\mathcal{Z}^\star - \mathcal{Z}\|}{\|\mathcal{Z}^\star\|}.$$

Preliminary experimental results quantified with this metric in Table 5.1 show that our approach provides accurate control of running with an average PE of 10% and a standard deviation of 1.85%, leading to an improvement compared to [68] reporting test results on the same platform. On the other hand, our results were in line with the previous work [68] when it comes to energy efficiency, however, opposing experimental data from the vertical hopper. Following the inquiry in [117] about the discrepancy between theory/simulations and ATRIAS hardware, we associate this contradiction between our results with several physical phenomenons of the ATRIAS platform that contribute to energetic losses greater than the gait controller :

1. ATRIAS' five bar leg configuration causes approximately a 50% loss of energy efficiency as one motor of a leg acts as a brake to the other with the majority of the power consumed for this internal cycle rather than delivered for the locomotion task. This energetic inefficiency was previously reported in [1] and referred to as antagonistic work due to legs' geometry.

2. The low compliance of legs compared to their light mass makes precise control of foot placement and contact detection challenging, hence leading to control inaccuracy and increased power consumption. In particular, incorrect timing of controller scheduling between stance and flight objectives and inaccurate realization of the desired touchdown angle α_{td} result in deviations from the theoretical performance.

Nonetheless, we need more data and experiments to draw definite conclusions about the performance of our approach.

5.5 Conclusion

In this chapter, we presented our efforts on transferring the CVD+ gait control policy to a complex humanoid robot, specifically ATRIAS bipedal robot. As the ATRIAS robot has point feet but a large trunk, the system is underactuated, hence precluding simultaneous stabilization of COM states and trunk orientation. In this context, in order to enforce postural stability while guaranteeing desired COM trajectories for running, we extend the FSLIP model by incorporating a trunk and a hip torque action providing stable trunk motion according to the virtual pivot point based pendulum control proposed in [69]. The extended model, which we call FSLIP-VPPC, is controlled according to a deadbeat CVD+ policy to achieve desired apex height, forward velocity, and angular position and velocity of the trunk. Later, COM trajectories and foot placement targets of the controlled FSLIP-VPPC model is realized on the robot with a task-space controller. Finally, we present some preliminary results of transient running experiments implemented on the robot, showing that our approach is promising and worth exploring in depth.

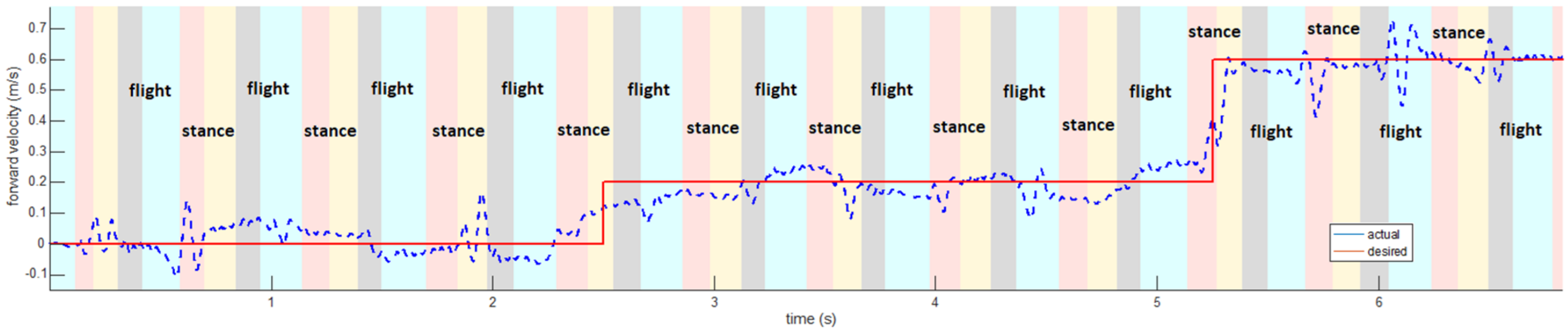

Figure 5.5: An example experiment showing commanded (solid-red) and actual (dashed-blue) forward velocities ranging from in-place hopping to 0.6 m/s.

Table 5.1: PE for different commanded changes in forward velocity across different base velocities and a constant apex height.

		velocity change (m/s)						
		-0.4	-0.2	0.0	0.2	0.4		
base velocity (m/s)	-1.0	10.6	8.6	7.9	9.4	10.2	1.05	apex height (m)
	-0.5	11.1	8.7	8.0	8.8	11.3	1.05	
	0.0	13.0	10.6	9.9	12.2	15.4	1.05	
	0.5	11.8	9.8	9.1	10.2	10.7	1.05	
	1.0	10.9	8.1	7.6	7.4	9.2	1.05	

CHAPTER 6

CONCLUSIONS

Legged robotics promise to be analogous to the automotive industry, in terms of size and how it transforms our society. In this revolution, we can see robots that help us in our homes, deliver groceries to people, or deliver manufactured goods for a factory as part of a logistics plan. In this regard, roboticists want to create machines that can go anywhere humans can go. These will not only reduce the cost of the manufacturer-to-consumer supply chain significantly but also help our aging society. Undoubtedly, these will have huge socioeconomic impacts on our world as a result. In recent decades, we have seen many robots built for these purposes as well as substantial improvements in their control. In particular, humanoids in the past were only able to balance themselves during a standing task, whereas we now see that humanoids can stably perform running motion. However, the energetic efficiency is still not a completely resolved problem. In this regard, focusing on this problem, this thesis proposes a new model-based approach for efficient and accurate control of robotic running.

In the first part of this thesis, we focused on developing a new model of running based on Spring-Loaded Inverted Pendulum (SLIP) to generate energetically controllable gaits. To this end, we proposed an FSLIP model having a tunable virtual damper for the regulation of energy. Our results showed that accurate and efficient control of running can be achieved through a once per step modulation of damping. This approach, known as deadbeat control, is formulated as a single step optimization problem. In order to facilitate the computational workload, we also proposed a procedure that yields approximate analytical solutions toFSLIP dynamics.

In the second part, our focus shifts from theoretical and simulation-based developments to experimental implementation. Towards this goal, we develop a set of feasibility conditions that should be satisfied by any control policy for accurate and energetically efficient running on physical platforms. Then, we propose a new control policy satisfying these constraints and show that it outperforms all available alternatives in the literature through numerical simulations. Finally, we implement this approach on two physical platforms : 1) A vertical hopping robot with a series elastic actuator 2) ATRIAS bipedal robot. Comprehensive experiments conducted on the former platform show experimental results aligning with simulations, hence suggesting that accuracy and efficiency translate to hardware with CVD+ policy and our controller implementation. Finally, we did some running experiments on the latter, which is a human-scale robot with compliant actuation. Even though we only managed to run a preliminary set of experiments on this platform, our collected data so far suggest that CVD+ policy provides accurate control.

Results from this thesis motivate exciting avenues for future work. First of all, our approach needs further evaluation on a sophisticated robotic platform like ATRIAS biped for reliable, statistically significant, and more scientific conclusions as our data from the ATRIAS biped is limited to a certain extent. In our application, we consider a SLIP-like template with virtual pivot point based pendulum control running with a stable posture. This model is solely based on biomechanical data, lacking insights from the hardware. Therefore, a study on running models with a stable upright trunk might explore better alternatives. In this regard, stabilization jeopardized by under-actuation due to the point feet can be compensated by developing self-stable models with a large basin of attraction, generating sufficiently smooth trajectories for robotic platforms. While exploring such models, scalability to higher dimensions (such as a model for 3D running) should also be taken into account. Otherwise, the deployment of policies based on these models will not be feasible on hardware. Another interesting avenue to explore is the use of parallel elastic actuation [119, 80] since, as shown in Chapters 4 and 5, major part of the motor work is channelled to the reflected motor inertia rather than to the robot's COM despite gait control policies specifically designed for energetic efficiency. Finally, the development of reactive footstep planning algorithms based on our model might be studied as future work to generate robust running behavior in cluttered environments.

REFERENCES

[1] A. Abate, J. W. Hurst, and R. L. Hatton. Mechanical Antagonism in Legged Robots. In *Proc. of the Robotics : Science and Systems*, 2016.

[2] G. Aguirre-Ollinger, J. Colgate, M. Peshkin, and A. Goswami. A 1-DOF Assistive Exoskeleton with Virtual Negative Damping: Effects on the Kinematic Response of the Lower Limbs. In *Proc. of the Int. Conf. on Intelligent Robots and Systems*, pages 1938–1944, 2007.

[3] M. Ahmadi and M. Buehler. Controlled Passive Dynamic Running Experiments With the ARL-Monopod II. *IEEE Transactions on Robotics*, 22(5):974–986, October 2006.

[4] R. Altendorfer, U. Saranli, H. Komsuoglu, D. E. Koditschek, J. H. B. Brown, M. Buehler, N. Moore, D. McMordie, and R. Full. Evidence for Spring Loaded Inverted Pendulum Running in a Hexapod Robot. In D. Rus and S. Singh, editors, *Experimental Robotics VII*, chapter 5, pages 291–302. Springer, December 2000.

[5] B. Andrews, B. Miller, J. Schmitt, and J. E. Clark. Running over Unknown Rough Terrain with a One-Legged Planar Robot. *Bioinspiration & Biomimetics*, 6(2), 2011.

[6] M. M. Ankarali and U. Saranli. Stride-to-Stride Energy Regulation for Robust Self-Stability of a Torque-Actuated Dissipative Spring-Mass Hopper. *Chaos: An Interdisciplinary Journal of Nonlinear Science*, 20(033121), September 2010.

[7] M. M. Ankarali and U. Saranli. Control of Underactuated Planar Pronking through an Embedded Spring-Mass Hopper Template. *Autonomous Robots*, 30(2):217–231, 2011.

[8] T. Apgar, P. Clary, K. Green, A. Fern, and J. Hurst. Fast Online Trajectory

Optimization for the Bipedal Robot Cassie. In *Proc. of Robotics : Science and Systems*, 2014.

[9] O. Arslan. Model Based Methods for the Control and Planning of Running Robots. M.Sc., Bilkent University, Ankara, Turkey, July 2009.

[10] O. Arslan and U. Saranli. Reactive Planning and Control of Planar Spring-Mass Running on Rough Terrain. *IEEE Trans. on Robotics*, 28(3):567–579, 2012.

[11] C. G. Atkeson and B. Stephens. Multiple Balance Strategies From One Optimization Criterion. In *Proc. of the IEEE/RAS Int. Conf. on Humanoid Robots*, 2007.

[12] R. Blickhan. The Spring-Mass Model for Running and Hopping. *Journal of Biomechanics*, 22(11-12):1217–1227, 1989.

[13] R. Blickhan and R. Full. Similarity in Multilegged Locomotion: Bouncing Like a Monopode. *Journal of Comparative Physiology A*, 173(5):509–517, November 1993.

[14] B. G. Buss, K. A. Hamed, B. A. Griffin, and J. W. Grizzle. Experimental Results for 3D Bipedal Robot Walking based on Systematic Pptimization of Virtual Constraints. In *Proc. of the American Control Conf.*, 2016.

[15] K. Byl, M. Byl, M. Rutschmann, B. Satzinger, L. V. Blarigan, G. Piovan, and J. Cortell. Series-Elastic Actuation Prototype for Rough Terrain Hopping. In *Proc of the Int. Conf. on Technologies for Practical Robot Applications*, pages 103–110, April 2012.

[16] S. G. Carver, N. J. Cowan, and J. M. Guckenheimer. Lateral Stability of the Spring-Mass Hopper Suggests a Two-Step Control Strategy for Running. *Chaos : An Interdisciplinary Journal of Nonlinear Science*, 19(2), June 2009.

[17] J. G. Cham, S. A. Bailey, J. E. Clark, R. J. Full, and M. R. Cutkosky. Fast and Robust: Hexapedal Robots via Shape Deposition Manufacturing. *The Int. Journal of Robotics Research*, 21(10):869–882, 2002.

[18] W. Chen. Differential Operator Method of Finding A Particular Solution to An Ordinary Nonhomogeneous Linear Differential Equation with Constant Coefficients. *arXiv preprint arXiv:1802.09343*, 2018.

[19] C. Chevallereau, J. W. Grizzle, and C.-L. Shih. Asymptotically Stable Walking of a Five-Link Underactuated 3D Bipedal Robot. *IEEE Transactions on Robotics*, 25(1):37–50, February 2009.

[20] C. Concordia and G. K. Carter. Negative Damping of Electrical Machinery. *Transactions of the American Institute of Electrical Engineers*, 60(3):116–119, 1941.

[21] B. Dadashzadeh, H. Vejdani, and J. Hurst. From Template to Anchor : A Novel Control Strategy for Spring Mass Running of Bipedal Robots. In *Proc. of the IEEE/RSJ Int. Conf. on Intelligent Robots and Systems*, pages 2566–2571, Sept 2014.

[22] A. De and D. E. Koditschek. Parallel Composition of Templates for Tail-Energized Planar Hopping. In *Proc. of the IEEE Int. Conf. on Robotics and Automation*, 2015.

[23] A. De and D. E. Koditschek. Vertical Hopper Compositions for Preflexive and Feedback-Stabilized Quadrupedal Bounding, Pacing, Pronking, nd Trotting. *The Int. Journal of Robotics Research*, 37(7):743–778, 2018.

[24] J. C. Doyle, B. A. Francis, and A. R. Tannenbaum. *Feedback Control Theory*. Dover Publications, 2009.

[25] M. Ernst, H. Geyer, and R. Blickhan. Extension and Customization of Self-Stability Control in Compliant Legged Systems. *Bioinspiration and Biomimetics*, 7(4), 2012.

[26] J. Estremera and K. J. Waldron. Thrust Control, Stabilization and Energetics of a Quadruped Running Robot. *The Int. Journal of Robotics Research*, 27(10):1135–1151, Oct. 2008.

[27] R. J. Full and D. E. Koditschek. Templates and Anchors: Neuromechanical Hypotheses of Legged Locomotion. *Journal of Experimental Biology*, 202:3325–3332, 1999.

[28] M. Garcia, A. Chatterjee, A. Ruina, and M. Coleman. The Simplest Walking Model: Stability, Complexity, and Scaling. *Journal of Biomechanical Engineering*, 120(2):281–288, 1998.

[29] H. Geyer and U. Saranli. *Gait Based on the Spring-Loaded Inverted Pendulum*, pages 923–947. Springer Netherlands, Dordrecht, 2019.

[30] H. Geyer, A. Seyfarth, and R. Blickhan. Compliant Leg Behaviour Explains Basic Dynamics of Walking and Running. *Proc. of the Royal Society B*, 273(1603):2861–2867, 2006.

[31] R. M. Ghigliazza, R. Altendorfer, P. Holmes, and D. Koditschek. A Simply Stabilized Running Model. *SIAM Journal of Applied Dynamical Systems*, 2(2):187–218, 2003.

[32] Y. Gong, R. Hartley, X. Da, A. Hereid, O. Harib, J. Huang, and J. Grizzle. Feedback Control of a Cassie Bipedal Robot: Walking, Standing, and Riding a Segway. In *Proc. of American Control Conf.*, 2019.

[33] P. Gregorio, M. Ahmadi, and M. Buehler. Design, Control, and Energetics of an Electrically Actuated Legged Robot. *IEEE Transactions on Systems, Man, and Cybernetics–Part B: Cybernetics*, 27(4):626–634, August 1997.

[34] P. Gregorio, M. Ahmadi, and M. Buehler. Design, Control, and Energetics of an Electrically Actuated Legged Robot. *IEEE Trans. on Systems, Man, and Cybernetics - Part B : Cybernetics*, 27(4):626–634, 1997.

[35] J. Grimes. ATRIAS 1.0 & 2.1 : Enabling Agile Biped Locomotion with a Template Driven Approach to Robot Design. Master's thesis, Oregon State University, 2013.

[36] J. A. Grimes and J. W. Hurst. The Design of ATRIAS 1.0 a Unique Monopod, Hopping Robot. In *Proc. of the Int. Conf. on Climbing and Walking Robots*, 2012.

[37] J. W. Grizzle, G. Abba, and F. Plestan. Asymptotically Stable Walking for Biped Robots : Analysis via Systems with Impulse Effects. *IEEE Transactions on Automatic Control*, 46(1):51–64, 2001.

[38] J. W. Grizzle, J. W. Hurst, B. Morris, H. Park, and K. Sreenath. MABEL, A New Robotic Bipedal Walker and Runner. In *Proc. of the American Control Conference*, pages 2030–2036, 2009.

[39] O. Gur and U. Saranli. Model Based Proprioceptive State Estimation for Spring-Mass Running. In *Robotics: Science and Systems VII*. The MIT Press, 2012.

[40] H. Hamzacebi and O. Morgul. On The Periodic Gait Stability of a Multi-Actuated Spring-Mass Hopper Model via Partial Feedback Linearization. *Nonlinear Dynamics*, 88(2):1237–1256, April 2017.

[41] A. Hereid, C. M. Hubicki, E. A. Cousineau, and A. D. Ames. Dynamic Humanoid Locomotion: A Scalable Formulation for HZD Gait Optimization. *IEEE Transactions on Robotics*, 34(2):370–387, 2018.

[42] K. L. Hoffman and R. J. Wood. Myriapod-Like Ambulation of a Segmented Microrobot. *Autonomous Robots*, 31:103–114, 2011.

[43] P. Holmes. Poincaré, Celestial Mechanics, Dynamical-Systems Theory and "Chaos". *Physics Reports*, 193(3):137–163, 1990.

[44] P. Holmes, R. Full, D. Koditschek, and J. Guckenheimer. The Dynamics of Legged Locomotion: Models, Analyses, and Challenges. *SIAM Review*, 48(2):207–304, 2006.

[45] C. Hubicki, A. Abate, P. Clary, S. Rezazadeh, M. Jones, A. Peekema, J. V. Why, R. Domres, A. Wu, W. Martin, H. Geyer, and J. Hurst. Walking and Running with Passive Compliance: Lessons from Engineering: A Live Demonstration of the ATRIAS Biped. *IEEE Robotics and Automation Magazine*, 25(3):23–39, 2018.

[46] C. Hubicki, J. Grimes, M. Jones, D. Renjewski, A. Sprowitz, A. Abate, and J. Hurst. ATRIAS : Design and Validation of a Tether-Free 3D-Capable Spring-Mass Bipedal Robot. *The Int. Journal of Robotics Research*, 35(12):1497–1521, 2016.

[47] C. M. Hubicki and J. W. Hurst. Running on Soft Ground: Simple, Energy-Optimal Disturbance Rejection. In *Proc. of the Int. Conf. on Climbing and Walking Robots*, page 548. World Scientific, 2012.

[48] J. W. Hurst. The Electric Cable Differential Leg: A Novel Design Approach for Walking and Running. *Int. Journal of Humanoid Robotics*, 08(02):301–321, 2011.

[49] J. W. Hurst, J. E. Chestnutt, and A. A. Rizzi. An Actuator with Physically Variable Stiffness for Highly Dynamic Legged Locomotion. In *Proc. of IEEE Int. Conf. on Robotics and Automation*, 2004.

[50] J. W. Hurst, J. E. Chestnutt, and A. A. Rizzi. Design and Philosophy of the BIMASC, a Highly Dynamic Biped. In *Proc. of the Int. Conf. on Robotics and Automation*, pages 1863–1868, April 2007.

[51] J. W. Hurst and A. A. Rizzi. Series Compliance for an Efficient Running Gait. *IEEE Robotics and Automation Magazine*, 15(3):42–51, 2008.

[52] A. Isidori. *Nonlinear Control Systems*. Springer-Verlag, 1995.

[53] D. Karnopp. Active Damping in Road Vehicle Suspension Systems. *Vehicle System Dynamics*, 12(6):291–311, 1983.

[54] C. J. Kempf and S. Kobayashi. Disturbance Observer and Feedforward Design for a High-Speed Direct-Drive Positioning Table. *IEEE Transactions on Control Systems Technology*, 7(5):513–526, 1999.

[55] G. Kenneally, A. De, and D. E. Koditschek. Design Principles for a Family of Direct-Drive Legged Robots. *IEEE Robotics and Automation Letters*, 1(2):900–907, 2016.

[56] O. Khatib. A Unified Approach for Motion and Force Control of Robot Manipulators : Operational Space Formulation. *IEEE Journal on Robotics and Automation*, 3(1):43–53, Feb. 1987.

[57] N. Kodera, H. Yamashita, and T. Ando. Active Damping of the Scanner for High-Speed Atomic Force Microscopy. *Review of Scientific Instruments*, 76(5):053708–053708–5, 2005.

[58] D. E. Koditschek and M. Buehler. Analysis of a Simplified Hopping Robot. *The Int. Journal of Robotics Research*, 10(6):587–605, 1991.

[59] D. Koepl and J. Hurst. Force Control for Planar Spring-Mass Running. In *Proc. of the Int. Conf. on Intelligent Robots and Systems*, pages 3758–3763, 2011.

[60] D. Koepl and J. Hurst. Impulse Control for Planar Spring-Mass Running. *Journal of Intelligent & Robotic Systems*, 74(3-4):589–603, 2014.

[61] K. Kong, J. Bae, and M. Tomizuka. Control of Rotary Series Elastic Actuator for Ideal Force-Mode Actuation in Human Robot Interaction Applications. *IEEE/ASME Transactions on Mechatronics*, 14(1):105–118, 2009.

[62] K. Kong, J. Bae, and M. Tomizuka. A Compact Rotary Series Elastic Actuator for Human Assistive Systems. *IEEE/ASME Transactions on Mechatronics*, 17(2):288–297, 2012.

[63] S. Kuinsderma, R. Deits, M. Fallon, A. Valenzuela, H. Dai, F. Permenter, T. Koolen, P. Marion, and R. Tedrake. Optimization-Based Locomotion Planning, Estimation, and Control Design for the ATLAS Humanoid Robot. *Autonomous Robots*, 40(3):429–455, 2016.

[64] J. Lee. *Introduction to Smooth Manifolds*. Springer, 2013.

[65] S. H. Lee and A. Goswami. Reaction Mass Pendulum (RMP): An Explicit Model for Centroidal Angular Momentum of Humanoid Robots. In *Proc. of the Int. Conf. on Robotics and Automation*, 2007.

[66] T. Libby, A. M. Johnson, E. Chang-Siu, R. J. Full, and D. E. Koditschek. Comparative Design, Scaling, and Control of Appendages for Inertial Reorientation. *IEEE Transactions on Robotics*, 32(6):1380–1398, Dec. 2016.

[67] W. C. Martin, A. Wu, and H. Geyer. Robust Spring Mass Model Running for a Physical Bipedal Robot. In *Proc. of the IEEE Int. Conf. on Robotics and Automation*, pages 6307–6312, May 2015.

[68] W. C. Martin, A. Wu, and H. Geyer. Experimental Evaluation of Deadbeat

Running on the ATRIAS Biped. *IEEE Robotics and Automation Letters*, 2(2):1085–1092, 2017.

[69] H. M. Maus, S. W. Lipfert, M. Gross, J. Rummel, and A. Seyfarth. Upright Human Gait Did Not Provide a Major Mechanical Challenge for Our Ancestors. *Nature Communications*, 1(70), 2010.

[70] M. Maus, J. Rummel, and A. Seyfarth. Stable Upright Walking and Running Using a Simple Pendulum Based Control Scheme. In *Proc. of the Int. Conf. of Climbing and Walking Robots*, 2008.

[71] B. Miller, J. Colgate, and R. Freeman. Guaranteed Stability of Haptic Systems with Nonlinear Virtual Environments. *IEEE Transactions on Robotics and Automation*, 16(6):712–719, 2000.

[72] B. Miller, J. Schmitt, and J. E. Clark. Quantifying Disturbance Rejection of SLIP-like Running Systems. *The Int. Journal of Robotics Research*, 31(5), 2011.

[73] K. N. Murphy and M. H. Raibert. *Theory and Practice of Robots and Manipulators*, chapter Trotting and Bounding in a Planar Two-Legged Model, pages 411–420. Springer, Boston, MA, 1985.

[74] J. Nakanishi, T. Fukuda, and D. E. Koditschek. A Brachiating Robot Controller. *IEEE Trans. on Robotics*, 16(2):109–123, 2000.

[75] S. Oh and K. Kong. High Precision Robust Force Control of a Series Elastic Actuator. *IEEE/ASME Transactions on Robotics*, 22(1):71–80, 2017.

[76] N. Paine, S. Oh, and L. Sentis. Design and Control Considerations for High Performance Series Elastic Actuators. *IEEE/ASME Transactions on Mechatronics*, 19(3):1080–1091, 2014.

[77] G. Piovan and K. Byl. Enforced symmetry of the stance phase for the Spring-Loaded Inverted Pendulum. In *Proc. of the Int. Conf. on Robotics and Automation*, pages 1908–1914, 2012.

[78] G. Piovan and K. Byl. Reachability-Based Control for the Active SLIP. *The Int. Journal of Robotics Research*, 34(3):270–287, 2015.

[79] G. Piovan and K. Byl. Approximation and Control of the SLIP Model Dynamics via Partial Feedback Linearization and Two-Element Leg Actuation Strategy. *IEEE Transactions on Robotics*, 32(2):399–412, 2016.

[80] M. Plooij, M. Wisse, and H. Vallery. Reducing the Energy Consumption of Robots Using the Bidirectional Clutched Parallel Elastic Actuator. *IEEE Trans. on Robotics*, 32(6):1512–1523, 2016.

[81] I. Poulakakis and J. W. Grizzle. The Spring Loaded Inverted Pendulum as the Hybrid Zero Dynamics of an Asymmetric Hopper. *IEEE Transactions on Automatic Control*, 54(8):1779–1793, Aug. 2009.

[82] N. A. Radford, P. Strawser, K. Hambuchen, J. S. Mehling, W. K. Verdeyen, A. S. Donnan, J. Holley, J. Sanchez, V. Nguyen, L. Bridgwater, R. Berka, R. Ambrose, M. Myles Markee, N. J. Fraser-Chanpong, C. McQuin, J. D. Yamokoski, S. Hart, R. Guo, A. Parsons, B. Wightman, P. Dinh, B. Ames, C. Blakely, C. Edmondson, B. Sommers, R. Rea, C. Tobler, H. Bibby, B. Howard, L. Niu, A. Lee, M. Conover, L. Truong, R. Reed, D. Chesney, R. Platt Jr, G. Johnson, C.-L. Fok, N. Paine, L. Sentis, E. Cousineau, R. Sinnet, J. Lack, M. Powell, B. Morris, A. Ames, and J. Akinyode. Valkyrie: NASA's First Bipedal Humanoid Robot. *Journal of Field Robotics*, 32(3):397–419, 2015.

[83] M. H. Raibert. *Legged Robots That Balance*. MIT Press, Cambridge, MA, USA, 1986.

[84] M. H. Raibert and H. B. Brown. Experiments in Balance with a 2D One-Legged Hopping Machine. *Journal of Dynamic Systems, Measurement, and Control*, 106(1):75–81, 1984.

[85] A. Ramezani, J. W. Hurst, K. Akbari Hamed, and J. W. Grizzle. Performance Analysis and Feedback Control of ATRIAS, A Three-Dimensional Bipedal Robot. *Journal of Dynamic Systems, Measurement, and Control*, 136(2):021012–021012, Dec. 2013.

[86] M. Rutschmann. Control of a Planar, One-Legged Hopping Robot Model on Rough Terrain. M.Sc., ETH Zurich, 2012.

[87] M. Rutschmann, B. Satzinger, M. Byl, and K. Byl. Nonlinear Model Predictive Control for Rough-Rerrain Robot Hopping. In *Proc. of the Int. Conf. on Intelligent Robots and Systems*, pages 1859–1864, 2012.

[88] U. Saranli, O. Arslan, M. M. Ankarali, and O. Morgul. Approximate Analytic Solutions to Non-Symmetric Stance Trajectories of the Passive Spring-Loaded Inverted Pendulum with Damping. *Nonlinear Dynamics*, 62(4):729–742, 2010.

[89] U. Saranli and D. E. Koditschek. Template based control of hexapedal running. In *Proc. of the Int. Conf. on Robotics and Automation*, 2003.

[90] E. Sariyildiz and K. Ohnishi. On The Explicit Robust Force Control via Disturbance Observer. *IEEE Transactions on Industrial Electronics*, 62(3):1581–1589, 2015.

[91] J. Schmitt and J. Clark. Modeling Posture-Dependent Leg Actuation in Leg Plane Locomotion. *Bioinspiration & Biomimetics*, 4(4), 2009.

[92] W. J. Schwind. *Spring Loaded Inverted Pendulum Running: A Plant Model*. Phd, University of Michigan, 1998.

[93] W. J. Schwind and D. E. Koditschek. Approximating the Stance Map of a 2-DOf Monoped Runner. *Journal of Nonlinear Science*, 10:533–568, 2000.

[94] G. Secer and U. Saranli. Control of Hopping Through Active Virtual Tuning of Leg Damping for Serially Actuated Robots. In *Proc. of the IEEE Int. Conf. on Robotics and Automation*, 2014.

[95] G. Secer and U. Saranli. Control of Planar Spring-Mass Running Through Virtual Tuning of Radial Leg Damping. *IEEE Transactions on Robotics*, 34(5):1370–1383, 2018.

[96] G. Secer and U. Saranli. Experimental Evaluation of Spring-Mass Hopping through Virtual Leg Damping. *IEEE Trans. on Robotics*, Currently Under Review.

[97] J. Seipel and P. Holmes. A Simple Model for Clock-Actuated Legged Locomotion. *Regular and Chaotic Dynamics*, 12(5):502–520, 2007.

[98] J. E. Seipel and P. Holmes. Running in Three Dimensions : Analysis of a Point-Mass Sprung-Leg Model. *Int. Journal of Robotics Research*, 24(8):657–674, 2005.

[99] A. Seyfarth, H. Geyer, M. Gunther, and R. Blickhan. A Movement Criterion for Running. *Journal of Biomechanics*, 35(5):649–655, 2002.

[100] M. Shahbazi, R. Babuska, and G. A. D. Lopes. Unified Modeling and Control of Walking and Running on the Spring-Loaded Inverted Pendulum. *IEEE Transactions on Robotics*, 32(5):1178–1195, Oct. 2016.

[101] M. Shahbazi, U. Saranli, R. Babuska, and G. A. D. Lopes. Approximate Analytical Solutions to The Double Stance Dynamics of The Lossy Spring-Loaded Inverted Pendulum. *Bioinspiration & Biomimetics*, 12(1), 2016.

[102] M. A. Sharafi, C. Maufroy, H. M. Maus, A. Seyfarth, M. N. Ahmadabadi, and M. J. Yazdanpanah. Controllers for Robust Hopping with Upright Trunk Based on the Virtual Pendulum Concept. In *IEEE/RSJ Int. Conf. on Intelligent Robots and Systems*, 2012.

[103] M. A. Sharbafi, C. Maufroy, M. N. Ahmadabadi, M. J. Yazdanpanah, and A. Seyfarth. Robust Hopping Based on Virtual Pendulum Posture Control. *Bioinspiration & Biomimetics*, 8(3), 2013.

[104] K. Sreenath, H.-W. Park, I. Poulakakis, and J. W. Grizzle. A Compliant Hybrid Zero Dynamics Controller for Stable, Efficient and Fast Bipedal Walking on MABEL. *Int. Journal of Robotics Research*, 30:1170–1193, 9 2011.

[105] K. Sreenath, H. W. Park, I. Poulakakis, and J. W. Grizzle. Embedding Active Force Control within the Compliant Hybrid Zero Dynamics to Achieve Stable, Fast Running on MABEL. *Int. Journal of Robotics Research*, 32(3):324–345, 2013.

[106] J. Tan, T. Zhang, E. Coumans, A. Iscen, Y. Bai, D. Hafner, S. Bohez, and V. Vanhoucke. Sim-to-Real: Learning Agile Locomotion For Quadruped Robots. In *Proc. of Robotics: Science and Systems*, 2018.

[107] M. Tenenbaum and H. Pollard. *Ordinary Differential Equations*. Dover Publications, 1985.

[108] P. Terry and K. Byl. CoM Control for Underactuated 2D Hopping Robots with Series-elastic Actuation via Higher Order Partial Feedback Linearization. In *Proc. of the IEEE 54th Annual Conference on Decision and Control*, 2015.

[109] P. Terry, G. Piovan, and K. Byl. Towards Precise Control of Hoppers : Using High Order Partial Feedback Linearization to Control the Hopping Robot FRANK. In *Proc. of the IEEE Conference on Decision and Control*, 2016.

[110] P. W. Terry. *Accurate Step Length Control Strategies for Underactuated and Realistic Series Elastic Actuated Hoppers via High Order PFL*. PhD thesis, University of California, Santa Barbara, 2016.

[111] O. Unver and M. Sitti. Flat Dry Elastomer Adhesives as Attachment Materials for Climbing Robots. *IEEE Transactions on Robotics*, 26(1):131–141, 2010.

[112] I. Uyanik, O. Morgul, and U. Saranli. Experimental Validation of a Feed-Forward Predictor for the Spring-Loaded Inverted Pendulum Template. *IEEE Transactions on Robotics*, 2014. Under review.

[113] I. Uyanik, U. Saranli, and O. Morgul. Adaptive Control of a Spring-Mass Hopper. In *Proc. of the Int. Conf. on Robotics and Automation*, pages 2138–2143, May 2011.

[114] H. Vallery, R. Ekkelenkamp, H. V. D. Kooiij, and M. Buss. Passive and Accurate Torque Control of Series Elastic Actuators. In *Proc. of the Int. Conf. on Intelligent Robots and Systems*, 2007.

[115] C. C. Wang and M. Tomizuka. Design of Robustly Stable Disturbance Observers Based on Closed Loop Consideration Using H_∞ Optimization and Its Applications to Motion Control Systems. In *Proc. of the American Control Conference*, 2004.

[116] P. M. Wensing and D. E. Orin. High-Speed Humanoid Running Through Control with a 3D-SLIP Model. In *Proc. of the IEEE/RSJ Int. Conf. on Intelligent Robots and Systems*, 2013.

[117] A. Wu. *The Theory, Implementation, and Evaluation of Spring-Mass Running on ATRIAS, a Bipedal Robot*. PhD thesis, Carnegie Mellon University, 2017.

[118] A. Wu and H. Geyer. The 3-D Spring-Mass Model Reveals a Time-Based Deadbeat Control for Highly Robust Running and Steering in Uncertain Environments. *IEEE Transactions on Robotics*, 29(5), 2013.

[119] Y. Yesilevskiy, W. Xi, and C. D. Remy. A Comparison of Series and Parallel Elasticity in a Monoped Hopper. In *Proc. of the IEEE Int. Conf. on Robotics and Automation*, 2015.

[120] H. Yu, M. Li, and H. Cai. Approximating the Stance Map of the SLIP Runner Based on Perturbation Approach. In *Proc. of the Int. Conf. on Robotics and Automation*, pages 4197–4203, 2012.

[121] G. Zeglin. *The Bow Leg Hopping Robot*. Ph.d., Carnegie Mellon University, October 1999.

CURRICULUM VITAE

PERSONAL INFORMATION

Surname, Name: Seçer, Görkem
Nationality: Turkish (TC)
Date and Place of Birth: 23 October 1987, Ordu
Marital Status: Married
Phone: +90 536 699 68 92
email: gsecer@gmail.com

EDUCATION

Degree	Institution	Year of Graduation
MS	Bilkent University Electrical and Electronics Engineering	2012
BS	ITU Control Engineering	2009
High School	Turgut Halil Kale Science High School	2004

WORK EXPERIENCE

Year	Place	Enrollment
2009-2020	ROKETSAN Missiles Industries	Engineer

FOREIGN LANGUAGES

Advanced English

PUBLICATIONS

1. Seçer G. and Saranlı U. "Control of Planar Spring Mass Running Through Virtual Tuning of Radial Leg Damping", IEEE Transactions on Robotics, 5(34), 1370-1383 (2018)